

**Computational investigation of weak-bonding interactions
in substituted borane-ketone complexes**

Philippe Archambault

A Thesis

in
The Department
of
Chemistry and Biochemistry

Presented in Partial Fulfillment of the Requirements for the Degree of Master of Science at
Concordia University
Montréal, Québec, Canada

August 2015

© Philippe Archambault, 2015

CONCORDIA UNIVERSITY
School of Graduate Studies

This is to certify that the thesis prepared

By: **Philippe Archambault**

Entitled: **Computational investigation of weak-binding interactions in substituted borane-ketone complexes**

and submitted in partial fulfillment of the requirements for the degree of

Master of Science (Chemistry)

complies with the regulations of this University and meets the accepted standards with respect to originality and quality.

Signed by the final examining committee:

_____ Chair
Dr. Louis Cuccia

_____ Examiner
Dr. Pat Forgione

_____ Examiner
Dr. Gilles H. Peslherbe

_____ Supervisor
Dr. Heidi M. Muchall

Approved by: _____
Chair of Department or Graduate Program Director

August 13, 2015

Dean of Faculty

Abstract

One of the largely unexplored areas of computational organic chemistry is the source of facial selectivity from prochiral ketones. Most of the available literature provides reaction pathways highlighting the lowest activation barrier, but this approach leaves the origin of the enantioselectivity unaddressed at the molecular level. Instead, the interactions that enable energetic differentiation in the transition states must be investigated for any useful information to be acquired for predictive purposes. The focus of this work is on the enantioselective CBS (Corey-Bakshi-Shibata) reduction as it has been extensively studied experimentally.

This work aims, first, to evaluate the complexation of substituted boranes with a prochiral ketone, acetophenone, for better understanding the modes of complexation during a reduction reaction, and second, to assess the source of facial selectivity of the enantioselective reduction of a different ketone, *t*-butyl methyl ketone, with borane using an oxazaborolidine catalyst. A systematic investigation of weak-bonding interactions in the complexes and their transition states is carried out computationally using electronic structure theory. A quantitative relationship between the electron demand on boron and the complexation energy is established from electron density analyses providing a binding cut-off of $0.19 \text{ e}\cdot\text{\AA}^{-3}$. In the CBS reduction of *t*-butyl methyl ketone, the calculated enantiomeric excess is 99 % or greater in favour of the *R*-configured product by transition state theory. The source of facial selectivity is uncovered through changes in features of the geometries and the electron densities as the responsible complexes as well as their transition states for hydride transfer are compared.

Acknowledgements

First and foremost, I would like to thank my supervisor Dr. Heidi M. Muchall for her assistance, patience, and support during my research. I am incredibly grateful that she allowed me to discover the joy of research at such an early stage in my academic career. She introduced me to the field of computational chemistry and I haven't looked back since. Without her help the completion of this thesis would have been painful. When I was doing something right she let me know the good work I was doing, but when I did something work she wasn't shy about it and I truly believe that it has helped me to push further in my research.

I would like to thank Dr. Pat Forgione and Dr. Peslherbe for their guidance, their suggestions and their comments as my committee members as I progressed in my research. They provided me with valuable insight and asked all the right questions to keep me on my toes. A special thanks to Dr. Denise Koch for her help and maintenance of the CERMM servers.

Finally, I would like to thank past group member Stephen Boateng and everyone in CERMM for their support; Colin Gavrilenko for his stimulating conversations about QTAIM and his help with advance topics in mathematics; and my family and close friends for putting up with me over the course of my degree.

In dedication to
my family and friends for their support.

Table of contents

<i>Abstract</i>	<i>iii</i>
<i>Acknowledgements</i>	<i>iv</i>
<i>List of Figures</i>	<i>ix</i>
<i>List of Schemes</i>	<i>xvi</i>
<i>List of Tables</i>	<i>xvii</i>
<i>List of Abbreviations and Symbols</i>	<i>xix</i>
Chapter 1. Introduction	1
1.1. Stereochemistry.....	1
1.1.1. Stereoisomers.....	1
1.1.2. Stereoselective synthesis.....	3
1.2. Reduction reactions.....	5
1.2.1. Brown's reaction.....	5
1.2.2. Carbonyl reduction.....	6
1.3. Organocatalysis.....	7
1.4. Boron.....	8
1.4.1. Borane and diborane	8
1.4.2. Boron-containing compounds.....	9
1.5. Non-covalent interactions	9

Chapter 2. Objectives and organization of the remainder of the thesis	11
2.1. Computational investigation of weak-bonding interactions in substituted borane-acetophenone complexes	14
2.2. Origin of the enantioselectivity in the <i>t</i> -butyl methyl ketone reduction with a chiral oxazaborolidine catalyst.....	15
Chapter 3. Computational investigation of weak-bonding interactions in substituted borane-acetophenone complexes.	16
3.1. Introduction.....	16
3.2. Computational Details	19
3.3. Results and Discussion	21
3.3.1. Boranes	21
3.3.2. Acetophenone-borane complexes	34
3.4. Conclusions.....	47
Chapter 4. Origin of the enantioselectivity in the <i>t</i>-butyl methyl ketone reduction with a chiral oxazaborolidine catalyst	49
4.1. Introduction.....	49
4.2. Computational Details	53
4.3. Results and Discussion	55
4.3.1. CBS Catalyst.....	55
4.3.2. Catalyst-borane adducts	57
4.3.3. Pre-reaction complexes.....	63

4.3.3.1. B···O complexation	63
4.3.3.2. C-H···O complexation	72
4.3.4. Reaction pathways (Transition States).....	78
4.3.4.1. Uncatalyzed reaction.....	78
4.3.4.2. Catalyzed reaction.....	80
4.3.4.2.1. Pathway 1. B···O complexation – <i>Si</i> -face attack.....	84
4.3.4.2.2. Pathway 2. B···O complexation – <i>Re</i> -face attack.....	86
4.3.4.2.3. Pathway 3. C-H···O complexation	89
4.4. Conclusions.....	90
Chapter 5. Conclusions and future work.....	92
References	96
Appendix A	105
Appendix B	111

List of Figures

Figure 1.1: Stereoisomers of 2,3,4-trihydroxybutanal.....	2
Figure 1.2: Asymmetric carbon atom (C*) in a tetrahedral geometry where $a \neq b \neq c \neq d$	3
Figure 1.3: Combined reaction profiles for the reduction of a generic prochiral ketone with hydride. <i>Re</i> -face attack producing <i>S</i> -alcohol (left), <i>Si</i> -face attack producing <i>R</i> -alcohol (right).....	5
Figure 3.1: Fixation of the aldehyde in pre-reaction complexes of enantioselective reactions through B···O (bolded) and C-H···O interactions. (Modified from ref. 39).....	17
Figure 3.2: Suggested ketone and ester coordination to trifluoroborane, stabilized by C α -H···F interactions ⁶⁰	18
Figure 3.3: Range of electron donating and electron withdrawing groups using the Hammett σ (m or p) constant as a reference point. Substituents chosen for this study are highlighted in the spread in pink.....	22
Figure 3.4: Molecular graphs of mono-, di-, and tri-substituted boranes from PBE0/6-311++G(2d,p). Atoms are represented by large spheres: carbon (grey), hydrogen (white), oxygen (red), nitrogen (blue), boron (pink), fluorine (cyan), chlorine (lime green) and bromine (maroon). Bond critical points are indicated by small red spheres, ring critical points by small yellow spheres.....	24
Figure 3.5: a) Borane with its empty 2p _z orbital. b) Adjacent nitrogen lone pair filling the 2p _z orbital on boron in the boranamine.....	25
Figure 3.6: NRT structures for mono-substituted boranes with π -electron donating groups. For simplicity, the lone pairs have been omitted. (From PBE0/6-311++G(2d,p).).....	28
Figure 3.7: NRT structures for mono-substituted boranes with non-electron donating groups. For simplicity, the lone pairs have been omitted. (From PBE0/6-311++G(2d,p).).....	29

Figure 3.8: a) Partial molecular graph of acetophenone with $\nabla^2\rho$ contour plot ($\nabla^2\rho > 0$ dashed lines, $\nabla^2\rho < 0$ solid lines; the arrow indicates a VSCC maximum). b) Molecular graph of borane with $\nabla^2\rho = 0$ surface (blue). Atoms are represented by large spheres: carbon (grey), oxygen (red), hydrogen (white) and boron (pink). Bond critical points are indicated by small red spheres. 31

Figure 3.9: Choosing a $\nabla^2\rho$ isosurface value to map ρ . a) Molecular graph of borane. b) Molecular graph of borane with (3,-1) Laplacian critical points. The black arrow points to one of the highlighted critical points that are displaced about boron. c) Blue $\nabla^2\rho$ isosurface with white arrow pointing to the same critical point. d) ρ mapped on $\nabla^2\rho$ isosurface. The ρ colour gradient allows a graphical determination of the density value. Atoms are represented by large spheres: hydrogen (white) and boron (pink). Bond critical points are indicated by small red spheres and Laplacian critical points by even smaller pink spheres. 31

Figure 3.10: Molecular graphs of substituted borane-acetophenone complexes 1k-17k, from PBE0/6-311++G(2d,p). Atoms are represented by large spheres: carbon (grey), hydrogen (white), oxygen (red), nitrogen (blue), boron (pink), fluorine (cyan), chlorine (lime green) and bromine (maroon). Bond critical points are indicated by small red spheres, ring critical points by small yellow spheres and cage critical points by small green spheres. 36

Figure 3.11: Molecular graphs of substituted borane-acetophenone complexes 18k-20k, from PBE0/6-311++G(2d,p). Atoms are represented by large spheres: carbon (grey), hydrogen (white), oxygen (red), nitrogen (blue), boron (pink), fluorine (cyan), chlorine (lime green) and bromine (maroon). Bond critical points are indicated by small red spheres, ring critical points by small yellow spheres and cage critical points by small green spheres. 37

Figure 3.12: Relative energies for relaxed scans of dihedral torsions in a conformational search for the fluoroborane-acetophenone complex 2k. Torsion (in 10° increments) of the (top) B-O-

$C_{C=O}-C_{Ph}$ dihedral and (bottom) $F-B-O-C_{C=O}$ dihedral. Structures shown represent minima. Dashed line added using Gaussview software⁹³. Atoms are represented by large spheres: carbon (grey), hydrogen (white), oxygen (red), fluorine (cyan) and boron (pink). From PBE0/6-311++G(2d,p). 37

Figure 3.13: Molecular graphs of acetophenone-borane complexes 11k and 13k, highlighting the weak interactions (arrows indicate $C\alpha-H\cdots O$). Atoms are represented by large spheres: carbon (grey), hydrogen (white), oxygen (red) and boron (pink). Bond critical points are indicated by small red spheres, ring critical points by small yellow spheres and a cage critical point by a small green sphere. From PBE0/6-311++G(2d,p). 39

Figure 3.14: Structural and electronic relationships in borane-acetophenone complexes: a) expected exponential relation between ρ_{BCP} and distance^{29,43}; b) scatter plot between ρ_{BCP} and the change in charge upon complexation, Δq_B (borane minus borane-complex). 42

Figure 3.15: Relationship between counterpoise-corrected binding energy in a set of borane-acetophenone complexes and B $2p_z$ occupancy for the corresponding set of boranes. Symbols are BH₃ (●), mono-substituted (○), di-substituted (×) and tri-substituted (Δ) boranes. The y-error incorporated by dashed lines represents $+1 \sigma_y$ of the fitted curve. 43

Figure 3.16: Relationship between binding (free) energies in borane-acetophenone complexes and ρ -on- $\nabla^2\rho$ values on boron in the corresponding set of boranes. Symbols are BH₃ (●), mono-substituted (○), di-substituted (×) and tri-substituted (Δ) boranes. The position of the “corrected” nitroborane density value from its restrained geometry is given by (●) (see text for details). x-error bars represent the largest error ($0.015 e\cdot\text{\AA}^{-3}$, from 17) identified in the determination of ρ -on- $\nabla^2\rho$ values. y-error incorporated by dashed lines represented $+1 \sigma_y$ of the fitted curve. 44

Figure 3.17: Molecular graphs of the a) nitroborane (17) optimized geometry, b) nitroborane constrained geometry, and c) optimized nitroborane-acetophenone complex (17k), from PBE0/6-311++G(2d,p). Atoms are represented by large spheres: carbon (grey), hydrogen (white), oxygen (red), nitrogen (blue) and boron (pink). Bond critical points are indicated by small red spheres, ring critical points by small yellow spheres..... 45

Figure 3.18: Relationship between counterpoise-corrected binding energy in methyl-substituted borane-acetophenone complexes 6k-8k and ρ -on- $\nabla^2\rho$ values on boron in the corresponding set of boranes. Symbols used are borane (\bullet), methylborane (\circ), dimethylborane (\times) and trimethylborane (Δ)..... 45

Figure 3.19: Molecular graphs of methylborane-acetophenone complexes 6k-8k highlighting the weak interactions (arrows indicate H \cdots H contacts). Atoms are represented by large spheres: carbon (grey), hydrogen (white), oxygen (red) and boron (pink). Bond critical points are indicated by small red spheres, ring critical points by small yellow spheres. From PBE0/6-311++G(2d,p). 46

Figure 4.1: The unsubstituted CBS catalyst with ring atoms numbered. 56

Figure 4.2: Molecular graphs of catalyst-borane adducts, showing non-diborane-like character (CBS-BH₃) and diborane-like character (CBS-dBH₃), from B3LYP/6-31+G(2d,2p). Atoms are represented by large spheres: carbon (grey), hydrogen (white), oxygen (red), nitrogen (blue) and boron (pink). Bond critical points are indicated by small red spheres, ring critical points by small yellow spheres..... 58

Figure 4.3: Energy profiles (relaxed scans, in kcal·mol⁻¹) for the B-N-B angle change in the catalyst-borane adducts. B3LYP/6-31+G(2d,2p) (solid line), MP2/6-311++G(2d,p) (dashed line), ω B97X-D/6-31+G(2d,2p) (dotted line) and PBE0/6-31+G(2d,2p) (dash-dotted line). The three \times

points represent the optimized CBS-BH₃ minima calculated with the respective model chemistries. The energies of the CBS-dBH₃ complexes from each functional are set to relative zero; the B-N-B bond angle was increased by one-degree increments. 60

Figure 4.4: Alignment of the substituted CBS-BH₃ geometry observed in the crystal^{145,146} (green) with that of the optimized unsubstituted CBS-BH₃ from B3LYP/6-31+G(2d,2p) (coloured by element). 61

Figure 4.5: NRT structures of CBS (left), CBS-BH₃ (middle) and CBS-dBH₃ (right) with their associated resonance weights in percent. For simplicity, only the lone pairs are represented and the formal charges have been omitted. (From B3LYP/6-31+G(2d,2p).)..... 62

Figure 4.6: Representations of B···O CBK complexes 1-6, from B3LYP/6-31+G(2d,2p). The dashed lines (added using Gaussview software⁹³) indicate the carbonyl oxygen interaction with the catalyst framework. 64

Figure 4.7: Alignment of the catalytic framework of B···O CBK complexes 1-6, from B3LYP/6-31+G(2d,2p), illustrating the B···O complexation landscape. 66

Figure 4.8: Relative energies (kcal·mol⁻¹) for various “conformations” of the CBS-BH₃ adduct, with that of the optimized B3LYP/6-31+G(2d,2p) geometry set to relative zero. A higher-energy conformation, identified with a prime on the number of the original complex, is isolated from its respective CBK complex 1-6, and its energy evaluated with the same model chemistry. 66

Figure 4.9: Complexation profiles for CBS-(d)BH₃ and subsequent CBK formation, with the reactants (ketone, CBS, BH₃) at relative zero, from B3LYP/6-31+G(2d,2p). Relative a) free energy and b) electronic energy (kcal·mol⁻¹). 69

Figure 4.10: Molecular graphs of pre-reaction complexes 1-6 from B3LYP/6-31+G(2d,2p). Atoms are represented by large spheres: carbon (grey), hydrogen (white), oxygen (red), nitrogen

(blue) and boron (pink). Bond critical points are indicated by small red spheres, ring critical points by small yellow spheres, cage critical points (indicating cage features) by small green spheres..... 70

Figure 4.11: Representations of C-H···O CBK complexes 7-15, from B3LYP/6-31+G(2d,2p). Bonds to the bridged hydrogen atom in 11 and 12 were not given in the Gaussview software and were not added manually. The dashed lines (added using Gaussview software⁹³) indicate the carbonyl oxygen interaction with the catalyst framework..... 73

Figure 4.12: Alignment of the catalytic framework of C-H···O CBK complexes 7-15, from B3LYP/6-31+G(2d,2p), illustrating part of the C-H···O complexation landscape..... 74

Figure 4.13: Molecular graphs of pre-reaction complexes 7-15 from B3LYP/6-31+G(2d,2p). Atoms are represented by large spheres: carbon (grey), hydrogen (white), oxygen (red), nitrogen (blue) and boron (pink). Bond critical points are indicated by small red spheres, ring critical points by small yellow spheres, cage critical points (indicating cage features) by small green spheres..... 77

Figure 4.14: Intrinsic reaction coordinate for the uncatalyzed reduction of *t*-butyl methyl ketone by BH₃, B3LYP/6-31+G(2d,2p). The points of inflection discussed (see text) are indicated with arrows..... 79

Figure 4.15: *t*-Butyl methyl ketone reduction reaction profile from reactants (ketone, CBS, BH₃) at relative zero to the rate limiting step: the hydride transfer transition state. Relative free energies (kcal·mol⁻¹) with the three reactants at relative zero, from B3LYP/6-31+G(2d,2p). 82

Figure 4.16: Molecular graphs for Pathway 1, leading to the experimentally observed enantiomer: pre-reaction complexes 1 and 2 and transition state TS1, from B3LYP/6-31+G(2d,2p). See text for the two conformations of the pre-reaction complex. 85

Figure 4.17: Molecular graphs for Pathway 2, leading to the experimentally unobserved enantiomer: pre-reaction complexes 4, 5 and 6 and their respective transition states TS2-TS4, from B3LYP/6-31+G(2d,2p). Cage critical points, indicating structural cage features, are shown by small green spheres. 88

Figure 4.18: Molecular graphs for Pathway 3: pre-reaction complex 11 (12) and corresponding TS5 (TS6) (leading to the experimentally (un)observed enantiomer), from B3LYP/6-31+G(2d,2p). 89

List of Schemes

Scheme 1.1: Hydroboration-oxidation reaction scheme.	6
Scheme 1.2: Asymmetric reduction of carbonyl compounds using the Noyori reaction.....	7
Scheme 2.1: CBS reduction reaction mechanism proposed by Corey. (Redrawn from ref. 40)..	11
Scheme 2.2: Thought development of reducing the complexity of the CBS reduction. CH ₃ removal: B-CH ₃ change to B-H does not affect the enantioselectivity ⁴⁰ ; di-phenyl removal: for computational economy, and preliminary computational work on the unsubstituted CBS is available; ketone substitution: lack of phenyl on CBS warrants the use of an aliphatic ketone...	13
Scheme 3.1: Reaction scheme of a <i>t</i> -butyl methyl ketone reduction catalyzed by an unsubstituted oxazaborolidine catalyst using borane.	47
Scheme 4.1: CBS reduction of acetophenone using a chiral oxazaborolidine catalyst with borane in THF. (Redrawn from ref. 40).....	51

List of Tables

Table 1.1: Non-covalent interactions comparison summary ³⁰	9
Table 3.1: Substituents R ¹ , R ² and R ³ in substituted boranes BR ¹ R ² R ³ 1-20. ^a	23
Table 3.2: Charge on boron, qB (au) and occupancy (number of electrons), from NBO natural population analyses following optimization at PBE0/6-311++G(2d,p). ^a	26
Table 3.3: Selected QTAIM results for mapping the electron density, $\rho(r)$, onto an isosurface of its Laplacian, $\nabla^2\rho(r)$: $\nabla^2\rho$ isosurface ($e\cdot\text{\AA}^{-5}$) and electron density ($e\cdot\text{\AA}^{-3}$) for boranes 1-20. The charge on boron, qB (au), is presented as well. ^{a,b}	33
Table 3.4: Selected geometric properties (distances in pm, dihedral angles and bond angles in °) in complexes 1k-20k, from PBE0/6-311++G(2d,p). ^a	35
Table 3.5: Uncorrected and corrected binding energies ($\text{kcal}\cdot\text{mol}^{-1}$) and selected electronic properties (electron density in $e\cdot\text{\AA}^{-3}$, Laplacian in $e\cdot\text{\AA}^{-5}$) at the bond critical point of the B \cdots O interaction in complexes 1k-20k, from PBE0/6-311++G(2d,p). ^{a,b}	41
Table 4.1: Selected geometric parameters (distances in pm, angles in °) of catalyst-borane adducts ^a from various model chemistries.	57
Table 4.2: Relative ^a electronic and Gibbs free energies ($\text{kcal}\cdot\text{mol}^{-1}$) of catalyst-borane adducts. ^b	58
Table 4.3: Value of the electron density ($e\cdot\text{\AA}^{-3}$) at the bond critical point of N3-B2 and B2-O1 interactions of the catalyst and catalyst-borane adducts. ^a Values in parentheses give the densities at the N3-B _{BH3} bond critical point.	62
Table 4.4: Selected geometric parameters (distances in pm, angles in °) of B \cdots O CBK complexes 1-6, from B3LYP/6-31+G(2d,2p).	64

Table 4.5: Relative ^a electronic and Gibbs free energies (kcal·mol ⁻¹) of pre-reaction complexes 1-6 with B···O interactions.....	67
Table 4.6: Value of the electron density (e·Å ⁻³) at the bond critical point of selected interactions of B···O CBK complexes 1-6, from B3LYP/6-31+G(2d,2p).....	71
Table 4.7: Selected geometric parameters (distances in pm, angles in °) of C-H···O CBK complexes 7-12, from B3LYP/6-31+G(2d,2p).....	74
Table 4.8: Relative ^a electronic and Gibbs free energies (kcal·mol ⁻¹) of pre-reaction complexes 7-15 with C-H···O interactions.....	75
Table 4.9: Value (e·Å ⁻³) of the electron density at the bond critical point of selected interactions of C-H···O CBK complexes 7-12, from B3LYP/6-31+G(2d,2p).	76
Table 4.10: Relative ^a electronic and Gibbs free energies (kcal·mol ⁻¹) of transition states TS1-TS7.....	81
Table 4.11: Calculated rate constants k (s ⁻¹) and relative rates k/k _{p1} for the hydride transfer reaction, using the 6-31+G(2d,2p) basis set.	83
Table 4.12: QTAIM oxygen charge (au) and electron density (e·Å ⁻³) at the bond critical point of selected interactions of transition states TS1-TS6, from B3LYP/6-31+G(2d,2p).....	84

List of Abbreviations and Symbols

Å	Angstrom
Δ	Difference
°	Degree
σ	Hammett substituent constants
ρ(r)	Electron density
∇ρ(r)	Gradient of the electron density
∇ ² ρ(r)	Laplacian of the electron density
ωB97X-D	Head-Gordon and co-worker's long-range corrected hybrid functional with dispersion correction
AB	Acetophenone-borane
AIM	Atoms in Molecules
B3LYP	Becke's three-parameter hybrid exchange/Lee-Yang-Parr-correlation functional
BCP	Bond critical point
BE	Binding energy
BSSE	Basis set superposition error
CBK	Catalyst-borane-ketone
CBS	Corey-Bakshi-Shibata
CCP	Cage critical point
cp	Counter-poise
CP	Critical point
DFT	Density-functional theory
e	Electron
E	Energy
E _{rel}	Relative energy
EDG	Electron donating group
EWG	Electron withdrawing group
G	Gibbs free energy

G _{rel}	Relative Gibbs free energy
HF	Hartree-Fock
IRC	Intrinsic reaction coordinate
kcal	Kilocalorie
LP CP	Laplacian critical point
L(r)	Negative of the Laplacian of the electron density
Me	Methyl
mol	Mole
MP2	Second order Møller-Plesset perturbation theory
NBO	Natural bond orbital
NRT	Natural resonance theory
PBE	Pedrew, Burke, Ernzerhof
PES	Potential energy surface
Ph	Phenyl
pm	Picometer
q	Atomic charge
QTAIM	Quantum theory of Atoms in Molecules
RCP	Ring critical point
<i>t</i> -Bu	<i>Tert</i> -butyl
THF	Tetrahydrofuran
TS	Transition state
ZPVE	Zero-point vibrational energy

Chapter 1.

Introduction

1.1. Stereochemistry

We interact with the world in three dimensions, and yet we are still developing an understanding of chemical concepts and structures in three dimensions. Stereochemistry, which refers to chemistry in three dimensions, was a concept that was only lately embraced; in the 19th century it was still unexplored. In the last 25 years, stereochemistry has become an important part of understanding problems in all fields of chemistry and as such no chemist should be without proper knowledge on the subject. Stereochemistry has often been divided into two major categories: static and dynamic. Static stereochemistry, or stereochemistry of molecules, consists mainly of stereoisomers, their energies and their physical properties. In contrast, dynamic stereochemistry, or stereochemistry of reactions, on the other hand consists mainly of stereochemical requirements and stereochemical outcomes of chemical reactions. Stereochemistry cannot be ignored as it is heavily required for the complete understanding of reaction mechanisms¹.

1.1.1. Stereoisomers

Isomers, compounds that share the same chemical formula but with different structures, can be placed into various categories based on their constitution, their configuration and their conformation. Isomers that only vary in configuration and/or conformation are recognized as stereoisomers. Stereoisomers can be further subdivided into enantiomers and diastereomers. The

terms enantiomer and diastereomer refer to molecules as a whole and therefore two enantiomeric/diastereomeric molecules must have the same connectivity, but differ in their spacial arrangement. While both subdivisions of stereoisomers may differ in configuration or only in conformation, the distinction lies in their geometrical relations (Fig. 1.1).

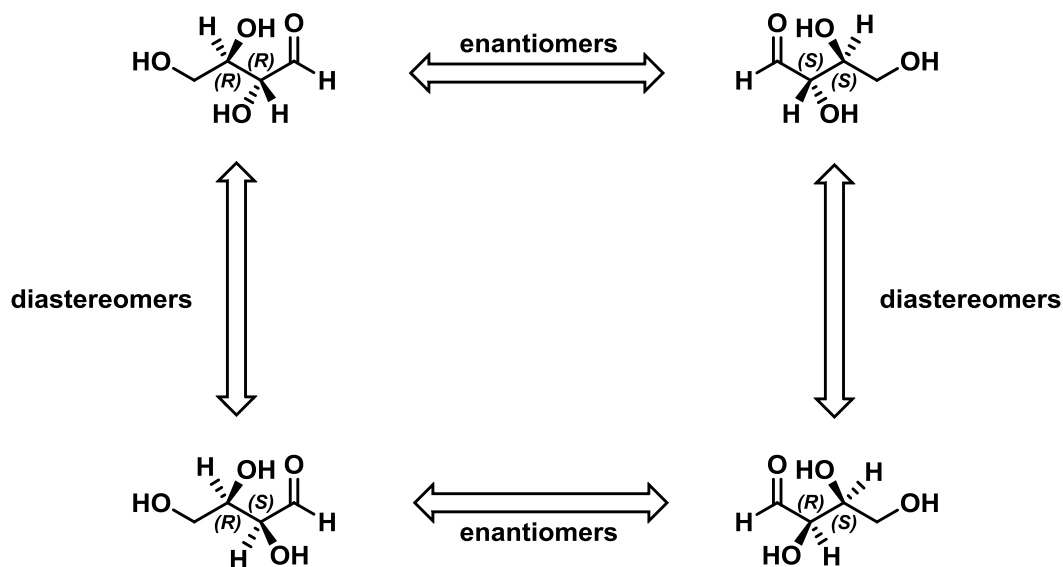


Figure 1.1: Stereoisomers of 2,3,4-trihydroxybutanal.

Enantiomers are pairs of isomers that are non-superimposable mirror images of one another, and their relation mainly comes from a configurational perspective. In contrast, diastereomers as in Fig. 1.1 do not have mirror-image relations to one another and stem from configurational (or conformational) differences at several locations in a molecule known as chiral centers. While enantiomers, in terms of chiral centers, are associated with one or more, diastereomers contain at least two. A chiral center, or center of chirality or asymmetric carbon atom (Fig. 1.2), leads to observable chirality. In 1874, van't Hoff demonstrated that a molecule with an asymmetric tetrahedral carbon atom is in fact chiral. This work followed the development of the Le Bel-van't

Hoff rule that states the number of stereoisomers an organic compound with no internal planes of symmetry can adopt is 2^n where n is equal to the number of asymmetric carbon atoms.

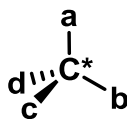


Figure 1.2: Asymmetric carbon atom (C^*) in a tetrahedral geometry where $a \neq b \neq c \neq d$.

To identify the stereochemical environment of each asymmetric carbon atom, the descriptors R and S are assigned. R , meaning *rectus*, and S , meaning *sinister*, identify the absolute configuration of a chiral center². Selecting the appropriate descriptor follows a simple set of rules³: (1) Each substituent is assigned a priority based on atomic number (higher atomic number means higher priority) and for two directly attached and identical atoms, the immediately connected adjacent atoms are taken into consideration (principle of outward exploration); (2) the substituent of lowest priority should be at the back (“d” in Fig. 1.2); and (3) descending in assigned priority of the remaining three substituents, a clockwise rotation means an R configuration, a counter clockwise rotation an S configuration. Since 1951, absolute configurations for chiral molecules possessing a heavy atom can be obtained by X-ray crystallography⁴.

1.1.2. Stereoselective synthesis

One of the fundamental aspects of organic synthesis is carrying out a reaction under stereochemical control, and such reactions can be placed into three general categories: (1) those that lead to the selective formation of enantiomers – enantioselective synthesis; (2) those that lead to the selective formation of diastereomers – diastereoselective synthesis; and (3) double

stereodifferentiating reactions, in which at least two reactants are chiral¹. Both diastereoselective synthesis and double stereodifferentiating reactions can be further subdivided, but this will not be discussed.

The term “enantiospecific” is used for syntheses employing one enantiomer of a chiral substrate and continue by diastereoselective reactions while maintaining the original enantiopurity. The more widely used term “enantioselective”, on the other hand, is used to describe syntheses that involve an enantioselective step, or a sequence of steps that produces a given enantiomer by temporarily incorporating a chiral auxiliary. These terms were developed to replace the cumbersome “enantiomerically pure compound synthesis⁵”, all the while avoiding scenarios in which a substrate or product is not technically “enantiomerically pure”. The traditionally identified “asymmetric synthesis” that leads to enantiomers has been redefined as enantioselective synthesis^{6,7}.

For example, the typical reduction of a generic prochiral ketone (i.e., a ketone in which addition to the carbonyl carbon atom leads to a chiral center) has two outcomes (Fig. 1.3). Either the reducing moiety, in this case a hydride, will attack the carbonyl *Re*-face producing the *S*-alcohol or it will attack the *Si*-face producing the *R*-alcohol. (The *Re*-/*Si*-nomenclature for facial attack is based on the same principle as that for the absolute configuration.) When no chiral information is present, there is no facial preference for the hydride attack. Consequently, the activation barriers for both attacks will be identical and a racemate (a 1:1 mixture of enantiomers) will be produced. However, the introduction of chiral information by any means (such as a solvent or a catalyst), will result in a differentiation of the activation barriers and producing potentially high enantiomeric excess. However, simply determining the transition state of lower energy is insufficient to determine the source of the facial preference. Facial selectivity

is a topic that has not been thoroughly investigated in computational organic chemistry and needs to be studied further. These ideas will be further explored in Chapter 4.

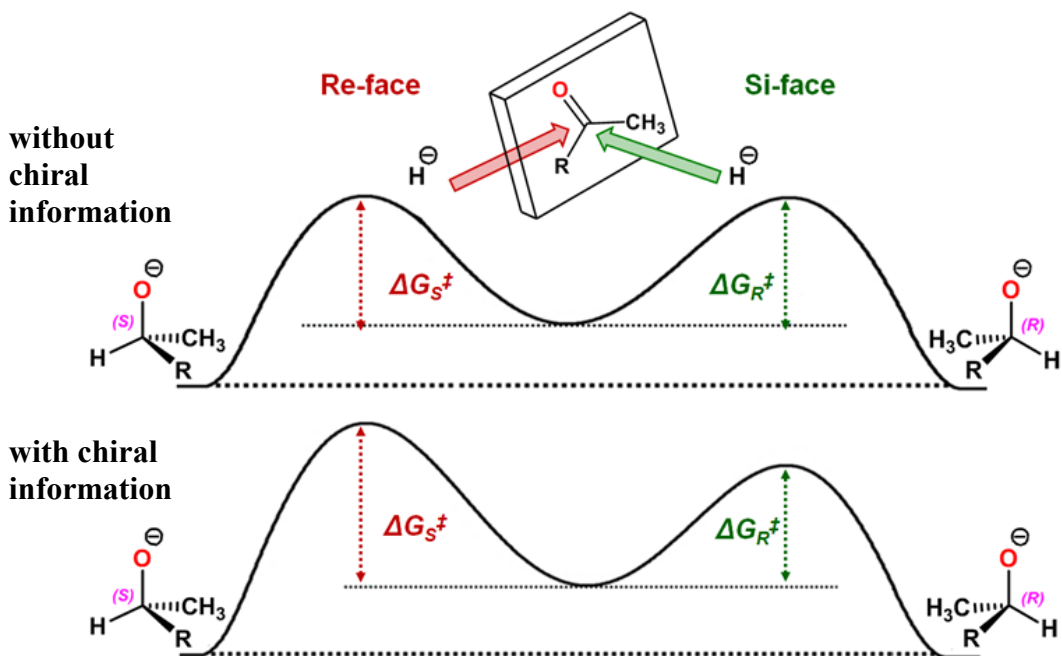
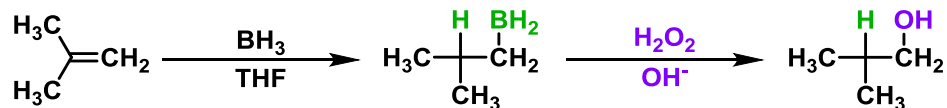


Figure 1.3: Combined reaction profiles for the reduction of a generic prochiral ketone with hydride. *Re*-face attack producing *S*-alcohol (left), *Si*-face attack producing *R*-alcohol (right).

1.2. Reduction reactions

1.2.1. Brown's reaction

There are many different reduction reactions that have been developed over the years. Arguably one of the most well-known is Brown's reaction, or hydroboration-oxidation reaction (Scheme 1.1). It is a two-step organic reaction that converts alkenes into alcohols. The reaction was first reported by H.C. Brown in 1959⁸ and helped pave the way for his, shared with Georg Wittig, 1979 Nobel Prize in chemistry.



Scheme 1.1: Hydroboration-oxidation reaction scheme.

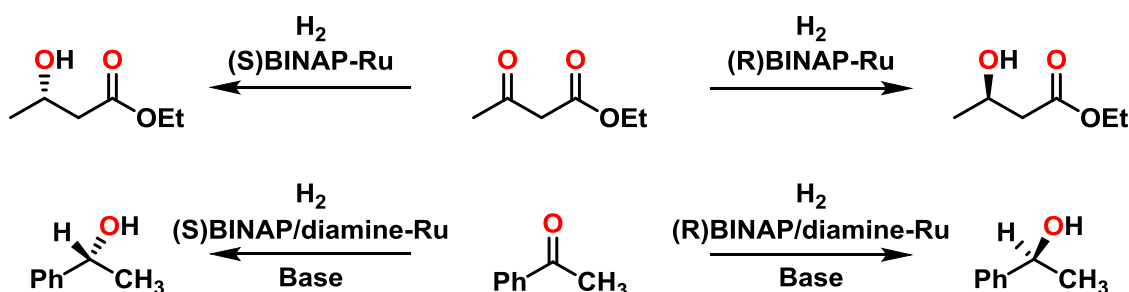
Prior to Brown's work on the hydroboration reaction, organic chemists did not have a viable method to generate alcohols under mild conditions. Diborane was a rare substance, produced by only a few laboratories, and organic chemists did not use it. While working with Schlesinger, a cheaper synthetic route was discovered by adding methyl borate to sodium hydride at high temperatures, producing NaBH_4 and NaOCH_3 . The addition of acetone to the mixture led to the discovery that NaBH_4 reduced the acetone. The discovery of NaBH_4 ⁹ in 1942 began innovative changes in procedures for the reduction of organic molecules. NaBH_4 is a mild reducing agent that works well on a variety of carbonyl compounds and is still used today¹⁰. This work led the way for the development of countless other carbonyl reduction reactions.

1.2.2. Carbonyl reduction

Carbonyls, such as aldehydes and ketones, can be reduced in different ways using a vast array of reducing agents. The two main types of carbonyl reduction are deoxygenation and hydrogenation. Deoxygenation, in the context of a carbonyl reduction, involves the removal of oxygen atoms from a molecule. In contrast, hydrogenation involves the addition of H_2 , generally in the presence of a catalyst such as nickel, platinum or palladium.

These types of reactions can be symmetric (non-stereoselective) or asymmetric (stereoselective). Some notable carbonyl reductions in asymmetric synthesis include the CBS reduction (using BH_3 and a chiral oxazaborolidine catalyst, see Chapter 4) and the Noyori asymmetric hydrogenation (Scheme 1.2).

In 2001, R. Noyori shared the Nobel Prize in chemistry with W.S. Knowles for their work on the asymmetric reduction of ketones. The reduction reaction is enantioselective and exploits the use of a chiral ruthenium catalyst¹¹. While the asymmetric reduction of ketones was not new¹², a practical catalytic reaction had not yet been available until it was introduced in 1994¹³. Noyori demonstrated that diastereoselectivity and enantioselectivity could be obtained simultaneously when using a chiral BINAP (2,2'-bis(diphenylphosphino)-1,1'-binaphthyl) ligand^{13,14}. The Noyori reaction is now used in the development of several antibacterial and antibiotic pharmaceuticals¹⁵.



Scheme 1.2: Asymmetric reduction of carbonyl compounds using the Noyori reaction.

1.3. Organocatalysis

Organocatalysis, originating from the terms “organic” and “catalyst”, is a form of catalysis and refers to the acceleration of a chemical reaction with non-stoichiometric amounts of an organic catalyst. An organic catalyst, or organocatalyst, often consists of carbon, hydrogen, oxygen and other non-metal elements, and as such organocatalysts have grown in popularity^{16,17}. Organocatalyzed reactions now cover a large range of reactions. Coupling reactions such as Suzuki¹⁸⁻²⁰ and Heck-type coupling²¹, that were once only transition-metal-mediated reactions, can now be performed in a green way without their respective inorganic metal components.

The majority of organocatalysts used are bifunctional and often with a Brønsted acid and a Lewis base center²². Lewis (hydrogen bonding) and Brønsted (proton-transfer) acid

organocatalysts involve (thio)ureas, diols, phosphoric acids, oxazaborolidines, guanidinium/amidinium ions, and bispidine²³. Organocatalyzed reaction with oxazaborolidines use boron as their reactive center (see Chapter 4).

1.4. Boron

Boron is the only non-metal element in Group 13 of the periodic table and as such shares similarities to its neighbouring elements, carbon and silicon, to a greater extent than with the other members of Group 13 (Al, Ga, In and Tl). It has the tendency to form covalent bonds, but due to having one less valence electron than C or Si, it is referred to as electron deficient and can differ severely in properties, both electronic and physical²⁴.

1.4.1. Boranes and diboranes

Less than 100 years ago, one of the simplest molecules of boron and hydrogen, diborane (B_2H_6), was thought to be a serious problem for the Lewis theory of bonding¹⁰, and this was true for all electron deficient boranes. Nowadays it is known that B_2H_6 possesses four terminal two-electron B-H bonds and four internal B-H-B bridges in which four electrons are responsible for four three-center-two-electron bonds. From an experimental point of view, diborane is of particular importance as all other boranes can be made from it. B_2H_6 is a gas that can be readily made, in small quantities, by reacting I_2 with $NaBH_4$ in diglyme ($(CH_3OCH_2CH_2)_2O$). Interestingly, diborane, can be used as a reactive intermediate, without requiring isolation or purification, when Et_2OBF_3 is added to $NaBH_4$, making it convenient to use in reactions²⁴.

1.4.2. Boron-containing compounds

Compounds containing boron play an important role in many disciplines of science^{25,26}. For example, carboranes are clusters of boron, carbon and hydrogen and have been studied as a boron source in boron neutron capture therapy (BNCT). For the past 50 years, boron is used as a delivery agent for cancer treatment in BNCT²⁷. Interactions between boron in boranes and oxygen in carbonyl compounds have also been investigated. Borane reagents form complexes with the carbonyl compounds, stabilizing the borane and activating the carbonyl for further synthesis²⁸. Such complexes are formed through weak coordinating interactions.

1.5. Non-covalent interactions

Non-covalent, or weak, interactions are part of the glue that holds the building blocks of chemistry and nature together. Interactions like ion-ion, ion-dipole, dipole-dipole, induced dipole-induced dipole, hydrogen bonding, van der Waals, and more, all fall under the umbrella of weak interactions. While the basic principles that govern each weak interaction are fundamentally the same, they differ in their magnitude, operative range and mode of operation²⁹ (Table 1.1).

Table 1.1: Non-covalent interactions comparison summary³⁰.

Interaction type	Operative range	Mode of operation	Typical magnitude
Ion-ion	Long	Non-directional	250 kJ·mol ⁻¹
Hydrogen bonding	Long	Directional	20 kJ·mol ⁻¹
Ion-dipole	Long	Non-directional	15 kJ·mol ⁻¹
Ion-induced dipole	Moderate	Non-directional	12 kJ·mol ⁻¹
Dipole-dipole	Short-Moderate	Directional	1-12 kJ·mol ⁻¹
Dispersion	Short	Non-directional	< 1 kJ·mol ⁻¹

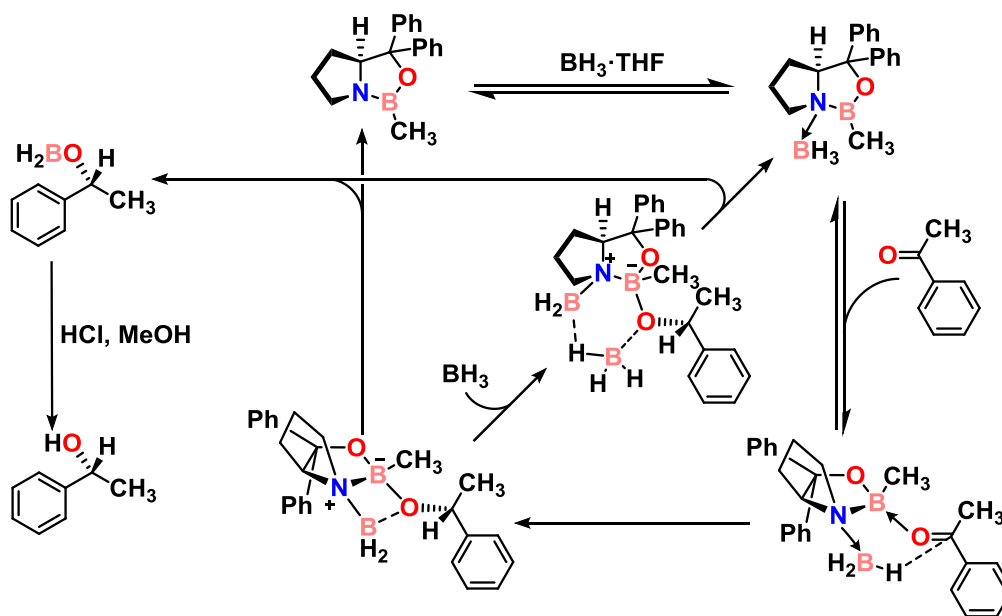
Typically, a hydrogen bond as given in Table 1.1 is the result of an interaction between the hydrogen atom of a group X-H and an electronegative atom. The X-H pair is referred to as the donor, Y is the acceptor. By convention, both X and Y atoms are electronegative and are often F, O or N. Due to the polarized nature of the covalent bond X-H, a highly electropositive hydrogen results that is attracted to the electron rich acceptor, Y.

Hydrogen bonding in which X is not a strongly electronegative atom, such as C, is often referred to as improper, or atypical, hydrogen bonding. The C-H \cdots O interaction was first predicted in crystal structures³¹ in 1963 and was the subject of much controversy. It is nowadays well established and is a prominent focus in weak interaction research³²⁻³⁶. C-H \cdots O interactions have numerous roles in the stability of reaction complexes³⁷⁻³⁹ as they help in providing anchoring points upon complexation (see Chapters 3 and 4).

Chapter 2.

Objectives and organization of the remainder of the thesis

From the interesting observation that the enantioselectivity in the CBS (Corey-Bakshi-Shibata) reduction reaction can depend strongly on the aromatic substituent on the CBS framework (97 % with diphenyl, 28 % with di(*ortho*-anisyl) for acetophenone), the overall goal of this work is to reveal the source of facial selectivity at the molecular level (Scheme 2.1). The CBS reduction is selected as it has been extensively studied experimentally and therefore provides a wealth of data for a computational study.



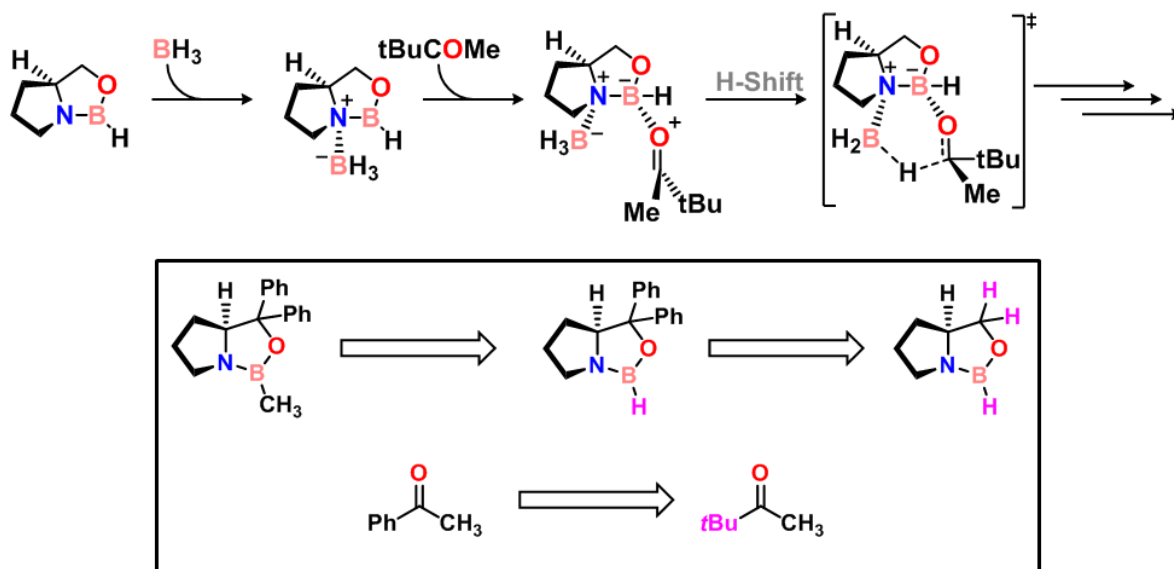
Scheme 2.1: CBS reduction reaction mechanism proposed by Corey. (Redrawn from ref. 40)

The first objective is to evaluate the complexation of substituted boranes with a prochiral ketone, acetophenone, in order to better understand the modes of complexation during the

reduction reaction studied later (Scheme 2.1). As suitable choice of boron substituents is to be made, and mono-, di- and tri-substitution are to be evaluated. In a first step, the geometries of the boranes are to be optimized. For this, the “parameter-free” hybrid DFT method by Pedrew, Burke and Ernzerhof (PBE0) functional is to be used and evaluated against the second order Møller-Plesset (MP2) method for accuracy. As the complexes used are mostly small, a triple zeta basis set is to be used. Changes in electronic structure of the boranes, with special attention to the electron demand on boron, are to be evaluated using Natural Bond Orbitals (NBO), Natural Resonance Theory (NRT) and the Quantum Theory of Atoms in Molecules (QTAIM) methodologies. In a second step, the borane-ketone complexes are to be treated similarly. In particular, though, and using the electron density (QTAIM analyses), attempts will be made at establishing a quantitative relationship between the electron demand on boron and the complexation energy.

The second objective is to investigate the CBS reduction of ketones with special attention to the weak interactions that lead to the facial selectivity. However, the first step in this work is to define which system to work on. Scheme 2.2 depicts the thought process in reducing the size (in terms of electron count, seeing that electronic structure theory methods will be used) of the catalytic system. Here, an unsubstituted CBS catalyst with *t*-butyl methyl ketone and BH_3 is to be investigated. The popular Becke’s 3-parameter exchange functional and the Lee-Yang-Parr correlation function (B3LYP), along with PBE0 and Head-Gordon’s long-range hybrid functional with dispersion correction (ω B97X-D) are to be employed and evaluated, if necessary, against MP2. Geometry optimizations will be carried out in a bottom-up approach for increasing complexity: first the CBS catalyst by itself, second plus the borane, lastly plus the ketone (Scheme 2.2). From the final complexes, the transition states for hydride transfer will be

optimized, and computed enantiomeric excess will be determined from the free energy-based rate constants (according to Transition State Theory). The geometries and electronic structures (using NBO, NRT and QTAIM) of all species are to be assessed (and evaluated against crystal structures if available), with particular emphasis on the weak bonding interactions in the catalyst-ketone complexes and their transition states. Finally, it will be attempted to determine the source of the facial preference, and therefore the enantioselectivity, through changes in features of either the geometries or the electron densities.



Scheme 2.2: Thought development of reducing the complexity of the CBS reduction. CH₃ removal: B-CH₃ change to B-H does not affect the enantioselectivity⁴⁰; di-phenyl removal: for computational economy, and preliminary computational work on the unsubstituted CBS is available; ketone substitution: lack of phenyl on CBS warrants the use of an aliphatic ketone.

Work on the first objective is presented in Chapter 3, that on the second objective in Chapter 4. Both chapters are presented in manuscript format aimed at publication. The two abstracts follow here. Chapter 5 presents the overall conclusions and a brief outlook on future work. Appendices A and B contain the supplemental material for Chapters 3 and 4, respectively.

2.1. Computational investigation of weak-bonding interactions in substituted borane-acetophenone complexes

To be submitted: Journal of Physical Chemistry A

Authors: Philippe Archambault and Heidi Muchall

Contributions by P.A.: Carried out all calculations and analyses of the computational results.

Abstract

We are interested in further investigating the binding interactions between borane derivatives and ketones. As such, in this work, electronic structure theory methods are used to evaluate the stability and bonding interactions in acetophenone ($C_6H_5COCH_3$) complexes with a series of substituted borane. While acetophenone, as a ketone, does not possess a C_α -H atom on an sp^2 -hybridized carbon, a feature that allows aldehydes to undergo interactions with certain substituents on boron, it does feature similar C_β -H on the phenyl ring. By probing the effect of the Lewis acid on the stability of the complexes and their bonding interactions, we hope to shed light on binding interactions that govern reactant-catalyst complexes in enantioselective reactions that involve borane-carbonyl complexes.

2.2. Origin of the enantioselectivity in the *t*-butyl methyl ketone reduction with a chiral oxazaborolidine catalyst

To be submitted: Journal of Organic Chemistry or Journal of Physical Chemistry A

Authors: Philippe Archambault and Heidi Muchall

Contributions by P.A.: Carried out all calculations and analyses of the computational results.

Abstract

The origin of enantioselectivity from prochiral compounds is one of the largely unexplored fields in computational organic chemistry. Extensive experimental work on the CBS reduction of prochiral ketones, which employs a chiral oxazaborolidine, allows for an interesting opportunity to try recovering the sources of facial selectivity. The reduction relies on the chiral catalyst-borane adducts approaching the ketones on their preferred face, and with the hydride transfer as the rate-limiting step. It therefore becomes critical to establish all reasonable ketone orientations within the complex. The often-assumed $B \cdots O=C$ complexation, in fact, is disfavoured due to the reduced electron demand of the catalytic framework's boron atom and leads to only one particular set of reasonable ketone orientations.

In this work, electronic structure theory methods are used to investigate the complexes of the Lewis acid catalyst with *t*-butyl methyl ketone, their corresponding transition states for hydride transfer, and bonding interactions in the complexes and transition states.

Chapter 3.

Computational investigation of weak-bonding interactions in substituted borane-acetophenone complexes

3.1. Introduction

Weak interactions are generally referred to as non-bonding interactions. Typical weak interactions include dipole-dipole interactions, hydrogen bonding and van der Waals forces. Their investigation in chemical and biological systems has become an important part of understanding how molecules interact with each other⁴¹⁻⁴³. Weak interactions are responsible for three-dimensional structures, such as proteins and nucleic acids, and life could not exist without them. Many different reactions depend on them to coordinate reactants and substrates, driving the reaction forward.

Uncommon hydrogen bonding, such as C-H \cdots O interactions, is believed to play a large part in the enantioselectivity of Diels-Alder reactions involving unsaturated aldehydes and often using chiral boron compounds as catalysts⁴⁴⁻⁴⁸. Corey and co-workers have proposed that the nature of the high enantioselectivity from chiral Lewis acid catalysts arises from the presence of a formyl hydrogen on the reactant interacting with fluorine or oxygen on the catalyst^{37,39,49,50}. Weak interactions within the reactant-catalyst complex would restrict the motion of the aldehyde and ensure the formation of one enantiomer in excess. X-ray crystal structures of complexes from 2,3-methylenedioxybenzaldehyde, as well as dimethylformamide, and boron-containing Lewis acids, indicate the potential presence of a hydrogen bond between the formyl hydrogen of the aldehyde reactant and the fluorine or oxygen atom of the Lewis acid⁵¹. The aldehydic C-H

and the B-X (X = F,O) bonds have a propensity to adopt a coplanar arrangement, with H \cdots X distances suitably close for a possible interaction. The electron deficient boron works as an electron acceptor to the oxygen lone pairs. The coordination of an aldehyde with a Lewis acid increases the positive charge at the formyl hydrogen, allowing for a “pre-orientation” of the aldehyde through weak interactions (Fig. 3.1).

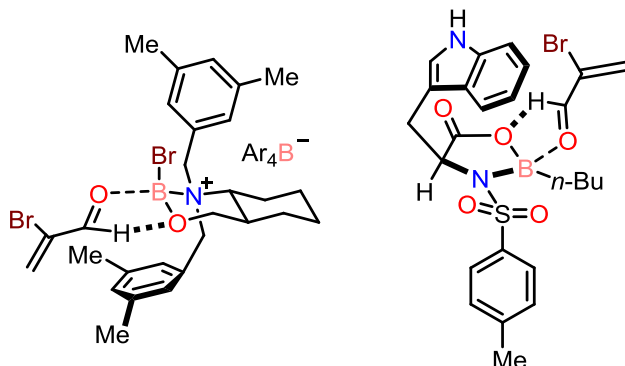


Figure 3.1: Fixation of the aldehyde in pre-reaction complexes of enantioselective reactions through B \cdots O (bolded) and C-H \cdots O interactions. (Modified from ref. 39)

The formation of an H_{aldehydic} \cdots X bond within Lewis acid-aldehyde complexes was consistent with earlier experimental and theoretical work on monofluoroborane (BH₂F) and trifluoroborane (BF₃) complexing with formaldehyde, acetaldehyde, or benzaldehyde. The complexes exhibited a preference for the Lewis acid to orient *anti* to the alkyl groups allowing the B-F bond to adopt a coplanar arrangement with the C=O group⁵²⁻⁵⁶. It was believed that the conformational preference of aldehyde-Lewis acid complexes was determined by a complex interplay of hyperconjugation interactions and steric effects from the groups attached to boron⁵⁷.

Despite experimental and theoretical evidence of H_{aldehydic} \cdots F interactions in aldehyde complexes with BF₃ and BH₂F, it remains unclear whether such interactions occur in the actual aldehyde-catalyst complexes. The chemical groups present on the catalyst moiety are expected to

exert large electronic effects on the boron atom, which could affect the structure and stability of the reactant-catalyst complexes.

In contrast to aldehydes, ketones lack a formyl hydrogen to form an $H_{\text{aldehydic}} \cdots X$ ($X = F, O$) bond, although Lewis acid-ketone complexes still occur. It has been proposed that α, β -unsaturated carbonyls, having $C_{\alpha}\text{-H}$ (Fig. 3.2) and potentially $C_{\beta}\text{-H}$ substitution, could form an $H \cdots X$ bond to stabilize the complexes⁵⁸. Corey notes that the reported distances are much shorter than the sum of the van der Waals radii, implying the probability of the interaction being present. However, no computational or otherwise follow-up study was conducted to substantiate the claim. Typical X-ray crystal structures of various ketone-borane derivatives display a lack of evidence to support this premise⁵⁹⁻⁶². These complexes show an increase in structural flexibility while demonstrating substantial changes in bonding interactions, in spite of only small changes (e.g. in substitution) on the borane or on the ketone.

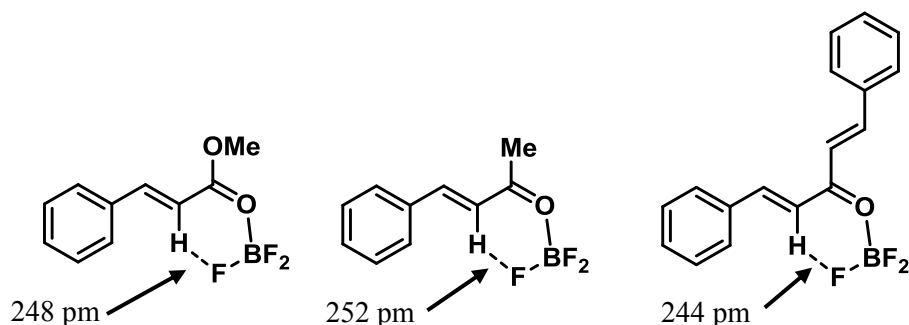


Figure 3.2: Suggested ketone and ester coordination to trifluoroborane, stabilized by $C_{\alpha}\text{-H} \cdots F$ interactions⁶⁰.

Previous work on borane and ketones has focused almost entirely on borane's use in chemical reactions, like in the reduction of carbonyl compounds^{40,63,64}, but not much has been done in investigating the binding interactions between borane derivatives and ketones. Morita and co-workers published two papers that focus, in part, on the effects of an observed increase in the ketone's carbonyl bond length after coordination of BF_3 to the ketone. Morita describes that

the increased bond length improves the interaction between the Pd d_{xy} orbital and the carbonyl carbon. Consequently, a shortening of the Pd \cdots C distance, due to the delocalization of Pd electrons to the carbonyl, increases the oxidation state of Pd⁵⁹. A similar observation was made with Pt⁶¹. While only a couple of Lewis acids were investigated (BF₃ and B(C₆F₅)₃), Morita states that, in principle, these observations could be witnessed for a variety of ketones/aldehydes, low-valent transition-metals, and Lewis acids combinations and used for the development of palladium-catalyzed catalytic conjugate addition of the alkyl-metals⁵⁹.

We are interested in further investigating the binding interactions between borane derivatives and ketones. As such, in this work, computational methods are used to evaluate the stability and bonding interactions in acetophenone (C₆H₅COCH₃) complexes with borane and borane derivatives. While acetophenone does not have C_α-H substitution on an sp²-hybridized carbon, it does have C_β-H substitution and is widely used by Corey and co-workers in highly enantioselective reduction reactions using chiral boron compounds as catalysts⁴⁰. By probing the effect of the Lewis acid on the stability and bonding interactions of the complexes, we hope to shed light on binding interactions that govern reactant-catalyst complexes in enantioselective reactions that involve borane-carbonyl complexes.

3.2. Computational Details

All calculations were performed using the Gaussian09 program⁶⁵. The geometries were optimized using the “parameter-free” hybrid DFT method by Pedrew, Burke and Ernzerhof (PBE0)^{66–69} with the 6-311++G(2d,p) basis set. Second order Møller-Plesset (MP2) perturbation theory^{70–74} with the same basis set was used in order to assess the reliability of PBE0. Frequency analyses with the same model chemistries were carried out to establish the nature of the stationary points. Electronic and free energies are given in S1 and S2 of Appendix A. Relaxed

scans (energy profiles) were obtained for the B-O-C_{C=O}-C_{Ph} and F-B-O-C_{C=O} dihedral angle change in the fluoroborane-acetophenone complex in ten-degree increments: only one dihedral angle was fixed at a time, the remaining geometry was allowed to fully optimize. The computed binding energies were corrected for basis set superposition error using the Counterpoise approach⁷⁵. Additionally, zero-point vibrational energy (ZPVE) corrections were included (Table 3.5), but are not discussed as they do not change the binding order of the borane-acetophenone complexes.

Bonding interactions for each ketone complex were determined from computed electron densities, $\rho(r)$ using the program AIMAll⁷⁶ within the Quantum Theory of Atoms in Molecules (QTAIM)^{77,78}. Due to negligible differences between the computed $\rho(r)$ obtained using the different functionals in this study, only the results from PBE0/6-311++G(2d,p) are presented in detail and discussed. Critical points in the topology of the electron density map onto established chemical entities: e.g., the position of a nucleus is represented, as expected, by an electron density maximum. In a molecule at minimum energy geometry, a line of maximum electron density (a so-called bond path) between two nuclei represents a bonding interaction. It is thus possible to determine which atoms are bonded, within and between molecules. Properties at the lowest-density point, the so-called bond critical point (BCP), along the bond path allow a characterization of the nature of the bonding interaction. A large value of the electron density (ρ_{BCP}) and a negative value of its Laplacian (the second derivative of the electron density, $\nabla^2\rho_{\text{BCP}}$) indicate a shared interaction (or covalent bond), whereas a small value in ρ_{BCP} and a positive $\nabla^2\rho_{\text{BCP}}$ are representative of a closed-shell interaction (such as in dative and hydrogen bonds, van der Waals complexes). The network of all bond paths for a chemical system is termed the molecular graph. In the molecular graphs, bond critical points are shown by small red

spheres; ring critical points, indicating structural ring features, by small yellow spheres; and cage critical points, indicating structural cage features, by small green spheres.

Atomic charges were determined using AIMAll and the natural bond orbital (NBO)^{79,80} approach as implemented in Gaussian09. The NBO calculations were also used to validate the presence of π -bonding within the catalyst framework. The NBO approach provided the occupancy of the p_z orbital on boron, which is empty in the unsubstituted borane. Upon substitution, the orbital occupancy provides insight into the appearance of π -bonding. Additional natural resonance theory (NRT)⁸¹⁻⁸⁴ evaluations were carried out using NBO5.G^{80,85}. Only the first one or two major resonance contributors are given; resonance structures with smaller contributions exhibit breakage of single bonds and were not considered further.

The novel ρ -on- $\nabla^2\rho$ approach was developed due to a lack of ways to directly measure the charge depletion, or hole in the VSCC (Valence Shell Charge Concentration). The density values obtained are an estimate of the electron density within the B $2p_z$ orbital and provide a complimentary analysis to the occupancy obtained using the NBO analysis.

3.3. Results and Discussion

3.3.1. Boranes

In order to understand the electronic effects on boron, a systematic approach was taken that depended on selecting substituents of both electron donating and electron withdrawing character; for a lack of more suitable options, substituents were selected based on their Hammett constants⁸⁶. While Hammett constants are defined for the benzenoid system, it seemed that boranes with their formally unoccupied $2p_z$ orbital on boron should respond compatibly to attached π -systems; the Hammett constants themselves were not used in this study but merely

guided the selection of the substituents. In all 12 substituents, plus an additional “cage”-substituent from a literature crystal structure⁶², were chosen, covering a wide range of potential electronic effects (Fig. 3.3). The boranes used in this study as well as the numbering scheme used are given in Table 3.1.

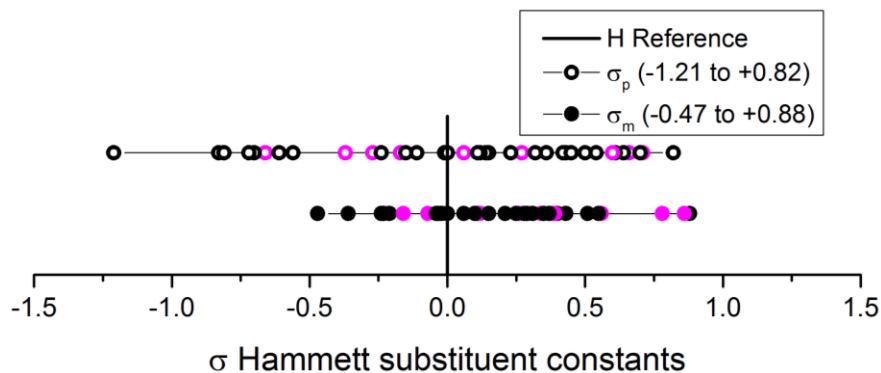


Figure 3.3: Range of electron donating and electron withdrawing groups using the Hammett σ (m or p) constant as a reference point. Substituents chosen for this study are highlighted in the spread in pink.

The optimized geometries of boranes **1-20** are shown in Fig. 3.4. Selected electronic properties from NBO and QTAIM analyses of these structures are summarized in Tables 3.2 and 3.3, respectively. The PBE0 functional was found in agreement with MP2 in finding minima and so the results are presented primarily using PBE0/6-311++G(2d,p).

Boranes with larger substituents (e.g., methoxyl substitution in **9**, **10** and **11**) can adopt different conformations (in the plane defined by the sp^2 -hybridized boron atom or out-of-plane), and their global minima are used in this study. The nitro-substituted **17** presents a strange case (Fig. 3.4). The O-N-O angle of its nitro group is immensely distorted from the norm, seemingly in an attempt of an oxygen atom to interact with the boron to satisfy the electron demand of the latter. An additional geometry was optimized by fixing the O-N-O angle (to a regular 115.6° , the

value in complex **17k**, see Section 3.3.2) for comparisons in the analyses of the electronic properties; this structure carries the planar BH₂ and NO₂ moieties at 90° to each other.

Table 3.1: Substituents R¹, R² and R³ in substituted boranes BR¹R²R³ **1-20**.^a

	R¹	R²	R³
1	H	H	H
2	F	H	H
3	Cl	H	H
4	Br	H	H
5	F	F	F
6	CH ₃	H	H
7	CH ₃	CH ₃	H
8	CH ₃	CH ₃	CH ₃
9	OCH ₃	H	H
10	OCH ₃	OCH ₃	H
11	OCH ₃	OCH ₃	OCH ₃
12	OH	H	H
13	OH	OH	H
14	NH ₂	H	H
15	NH ₃ ⁺	H	H
16	CN	H	H
17	NO ₂	H	H
18	NO ₂	OCH ₃	N(CH ₃) ₂
19	C ₆ F ₅	C ₆ F ₅	C ₆ F ₅
20			

^a See Fig. 3.4 for structures.

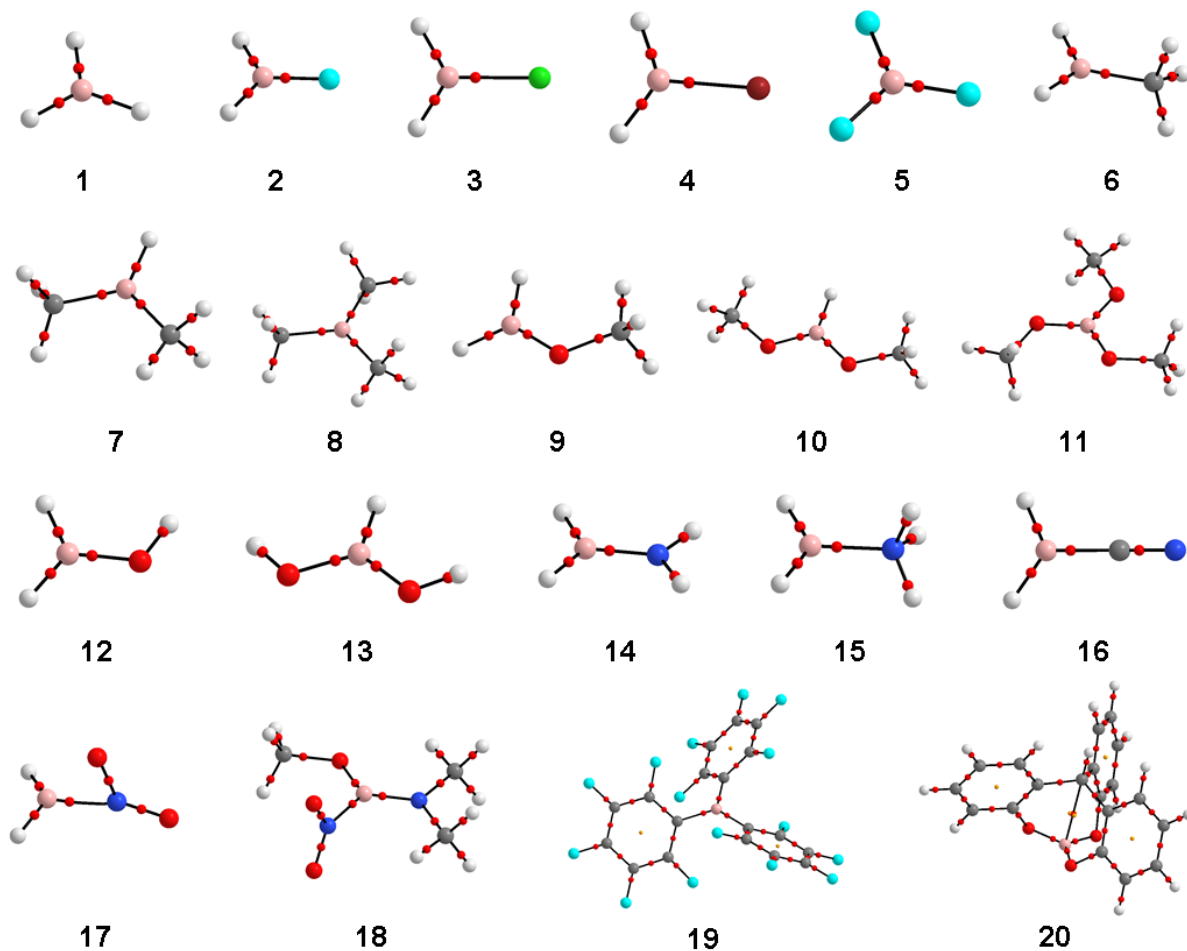


Figure 3.4: Molecular graphs of mono-, di-, and tri-substituted boranes from PBE0/6-311++G(2d,p). Atoms are represented by large spheres: carbon (grey), hydrogen (white), oxygen (red), nitrogen (blue), boron (pink), fluorine (cyan), chlorine (lime green) and bromine (maroon). Bond critical points are indicated by small red spheres, ring critical points by small yellow spheres.

NBO:

Natural population analysis from the NBO method was used to measure the electron occupancy of the boron $2p_z$ orbital. As shown in Fig. 3.5, boron, with its electron sextet, in BH_3 is hypovalent and vastly electron deficient. A neighbouring amino group, with its π -electron donating character, can fill the vacant p-orbital to satisfy the electron demand on boron. NBO calculates the bonding orbital with maximum electron occupancy, and as such, informs on which

substituents contribute to the $2p_z$ orbital and by how much. The NBO results from PBE0/6-311++G(2d,p) are summarized in Table 3.2.

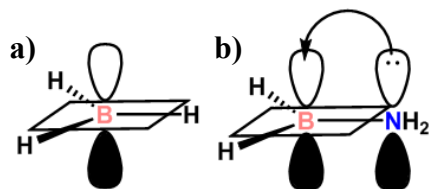


Figure 3.5: a) Borane with its empty $2p_z$ orbital. b) Adjacent nitrogen lone pair filling the $2p_z$ orbital on boron in the boranamine.

The B-H bonds in borane (**1**), as expected, do not possess any π -character and the $2p_z$ orbital is entirely unoccupied. Due to their high electronegativity, halogens are typically referred to as electron withdrawing groups, but their π -electron donating character is demonstrated through their ability to donate their electron lone pairs to fill the B $2p_z$ orbital. For the mono-substituted **2-4**, the charge on boron in **2** is more largely positive (0.749) compared to that in **3** and **4** (0.312 and 0.239, respectively), and the B $2p_z$ orbital shows less occupancy. Fluorine of course, as the most electronegative element, is less willing to donate its electrons to boron than Cl or Br. PBE0/6-311++G(2d,p) reports **5** as possessing a π -bond, which is in disagreement with the original work of Weinhold and co-workers^{81,82,87}, in which a hypovalent trifluoroborane structure with hardly any partial double bond character (bond order of 1.050) was reported.

Boranes **6-8** with their methyl substitution do not possess π -electron donating groups and as expected do not show any double bond character. The linear increase in B $2p_z$ occupancy along the series is observed due to increasing amounts in hyperconjugation (B $2p_z/\sigma_{C-H}$ interaction).

Table 3.2: Charge on boron, qB (au) and occupancy (number of electrons), from NBO natural population analyses following optimization at PBE0/6-311++G(2d,p).^a

	qB	B 2p _z occupancy	π bond
1	0.317	0.00	No
2	0.749	0.14	Yes
3	0.312	0.19	Yes
4	0.239	0.20	Yes
5	1.405	0.33	Yes
6	0.486	0.07	No
7	0.681	0.12	No
8	0.916	0.17	No
9	0.584	0.23	Yes
10	0.911	0.36	Yes
11	1.245	0.42	Yes
12	0.593	0.14	Yes
13	0.903	0.33	Yes
14	0.405	0.29	Yes
15	0.662	0.03	No
16	0.378	0.07	No
17	0.324 (0.533) ^b	0.28 (0.11) ^b	No
18	1.075	0.46	Yes
19	0.849	0.24	No
20	1.347	0.34	No

^a See Fig. 3.4 for structures. ^b Value from the constrained geometry, see text.

Methoxyl (**9-11**) and hydroxyl (**12** and **13**) substituted boranes exhibit B=O bond character and, in general, higher B 2p_z occupancy (again with a linear increase along a series) as the O lone pairs can donate into the empty 2p_z-orbital to form a π-bond. The ability to donate to the B 2p_z orbital can be dramatically demonstrated through **14**, with its amino substituent, and the related ammonium-substituted **15**. The removal of the nitrogen lone pair drops the rather large B 2p_z occupancy in **14** to about zero in **15** (again there is a small hyperconjugative interaction from

$\sigma_{\text{N-H}}$), and the π -character to the B-N bond in **14** is not present in **15**. For the aminoborane (**14**), the B $2p_z$ occupancy is comparable to that in borazine (0.35 electrons).

The cyano group in **16** is clearly a π -substituent, but its π -electrons are not available to donation and the B $2p_z$ orbital is left largely unoccupied. Similarly, the nitro group in **17** has π -character, but in its “proper” (i.e., constrained) geometry it does not donate its π -electrons to boron, because the NO_2 π -system and the vacant B $2p_z$ orbital are orthogonal. The occupancy instead arises from oxygen lone pairs through B $2p_z/n_{\text{O}}$ interactions. In the optimized structure, the electron demand on boron is sufficiently great for an oxygen to lean over. The geometry distortion is huge, but the required energy is more than compensated (optimized **17** is more stable than restrained **17** by $4.8 \text{ kcal}\cdot\text{mol}^{-1}$) through the now present B \cdots O interaction that fills the B $2p_z$ orbital to the same degree as the amino nitrogen in **14**.

The trisubstituted **18** exhibits the largest B $2p_z$ occupancy observed here, with a value similar to that in trimethoxyborane (**11**). **19** and **20** do not show the formation of a π -bond despite having higher B $2p_z$ occupancy.

NRT:

In accord with the NBO analysis, π -electron donating groups satisfy the electron demand on boron through resonance, which can be captured through NRT analysis (Fig 3.6). All 10 boranes with one or more electron donating groups possess a π -bond. There is, of course, no resonance in **1**.

For halogen mono-substituted boranes **2-4**, the leading resonance structure, with greater than 97 % weight, shows the presence of a π -bond. Like **2**, the trifluoro-substituted **5** prefers to have one fluorine lone pair fill the empty $2p_z$ orbital on boron, which, as mentioned above, contradicts

the findings of Weinhold and co-workers^{81,82,87}. From HF/6-31G*, the trifluoroborane octet-violating form was reported as the leading resonance structure, weighted at 76.1 %, and the octet-obeying structures weighted at only 5.2 %, which explains the reported small double bond character. In this work, from PBE0 and MP2 with a much larger basis set, the octet-violating structure is only weighted at 4.7 % (4.2 % for MP2), and the octet-obeying structures total 90.2 % (91.9 % for MP2), a result that seems more reasonable.

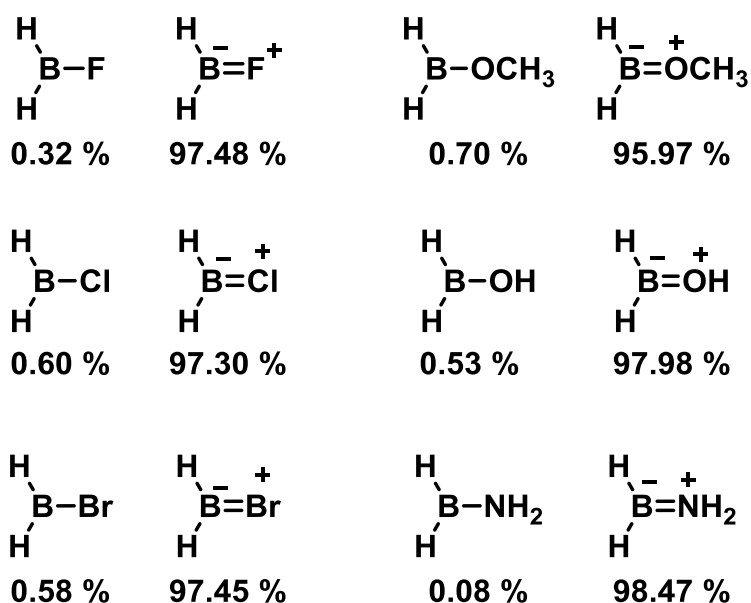


Figure 3.6: NRT structures for mono-substituted boranes with π -electron donating groups. For simplicity, the lone pairs have been omitted. (From PBE0/6-311++G(2d,p).)

For mono-substitution in **9** (OCH₃), **12** (OH) and **14** (NH₂), there is a preference for N to donate its electrons than for O. This is to be expected with N being closer in size to B and therefore experiencing a better orbital overlap, a fact that was made use of in the development of stable carbenes⁸⁸. The idea of N/O competition in their interaction with B is further addressed in Chapter 4, where the electronic structure of an oxazaborolidine (O-B-N functionality) catalyst is explored.

Again in accord with the NBO analysis, those substituents not π -electron donating prefer an octet-violating Lewis structure (Fig. 3.7). The hyperconjugation from $\sigma_{\text{C-H}}$ in **6** (CH_3 substitution) and $\sigma_{\text{N-H}}$ in **15** (NH_3^+ substitution) suggested from the B $2p_z$ occupancy is also reflected in the resonance description (Fig. 3.7). Not surprisingly, the resonance weight of the π -description for the already charged **15** is smaller than that for the neutral **6**.

Nitroborane (**17**) was not evaluated with respect to its resonance contributors, as its optimized geometry does not allow for “normal” resonance contributors. In the trisubstituted **18**, two distinct resonance contributors emerge from the analysis: 71.03% B=N (from NMe_2) and 8.05% B=O, as would be expected from the N/O competition discussed above. **19** and **20** were not investigated.

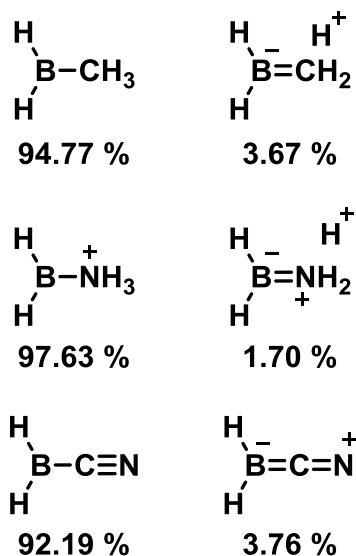


Figure 3.7: NRT structures for mono-substituted boranes with non-electron donating groups. For simplicity, the lone pairs have been omitted. (From PBE0/6-311++G(2d,p).)

QTAIM:

Although direct indication of electron lone pairs is not presented in the electron density, $\rho(\mathbf{r})$, itself, it can be found in the Laplacian of the electron density, $\nabla^2\rho(\mathbf{r})$, as a maximum in the valence shell charge concentration (VSCC)⁸⁹. Figure 3.8a shows such a maximum in $\nabla^2\rho$ of acetophenone. In analogy, regions of charge depletion can be recovered through $\nabla^2\rho(\mathbf{r})$ ⁸⁹, which is illustrated through borane in Fig. 3.8b, where an area of charge depletion, displaced from the plane of the nuclei, is visible above boron. With borane and acetophenone properly oriented, the source of complexation thus is captured through the Laplacian of the electron density. It was therefore desirable to determine the electron density in the general area of charge depletion on boron, i.e., at the location of the B $2p_z$ orbital in the molecular orbital picture. This “mapping of the electron density onto the Laplacian” (or ρ -on- $\nabla^2\rho$) approach is described in Appendix A. A proof of principle evaluating the ρ -on- $\nabla^2\rho$ approach against a previous and related study of the effect of the π -electron density at the positively charged carbon of a series of substituted carbocations on the ^{13}C chemical shift^{90,91} can be found in Appendix A.

The novel ρ -on- $\nabla^2\rho$ approach avoids simply using a ρ -value at an arbitrary distance from the B nucleus. Instead, we aimed to let QTAIM, which analyses the electron density obtained from the quantum chemical wavefunction, define a suitable point above B that would naturally be adjusted through any change in substitution.

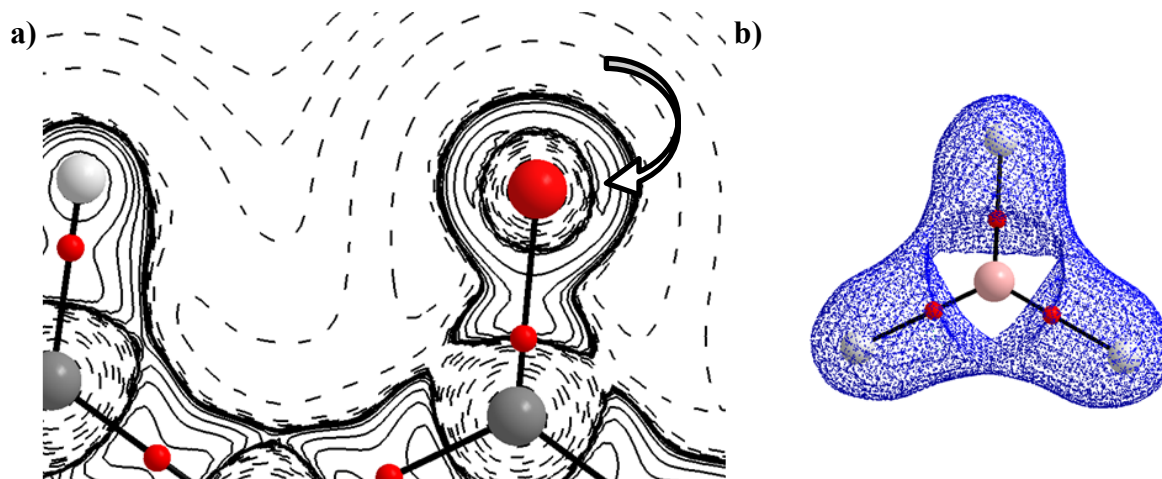


Figure 3.8: a) Partial molecular graph of acetophenone with $\nabla^2\rho$ contour plot ($\nabla^2\rho > 0$ dashed lines, $\nabla^2\rho < 0$ solid lines; the arrow indicates a VSCC maximum). b) Molecular graph of borane with $\nabla^2\rho = 0$ surface (blue). Atoms are represented by large spheres: carbon (grey), oxygen (red), hydrogen (white) and boron (pink). Bond critical points are indicated by small red spheres.

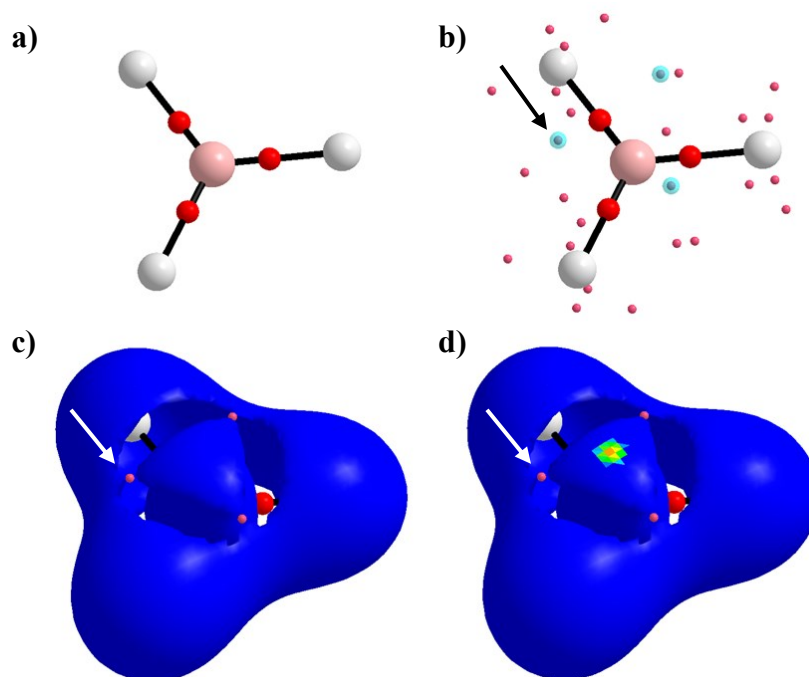


Figure 3.9: Choosing a $\nabla^2\rho$ isosurface value to map ρ . a) Molecular graph of borane. b) Molecular graph of borane with (3,-1) Laplacian critical points. The black arrow points to one of the highlighted critical points that are displaced about boron. c) Blue $\nabla^2\rho$ isosurface with white arrow pointing to the same critical point. d) ρ mapped on $\nabla^2\rho$ isosurface. The ρ colour gradient allows a graphical determination of the density value. Atoms are represented by large spheres: hydrogen (white) and boron (pink). Bond critical points are indicated by small red spheres and Laplacian critical points by even smaller pink spheres.

Figure 3.9 illustrates the ρ -on- $\nabla^2\rho$ approach. A $\nabla^2\rho$ isosurface is chosen according to the value at a (3,-1) Laplacian critical point (LP CP). Whereas the value of such a (3,-1) Laplacian critical point around boron varies somewhat with substitution, its (3,-1) nature is the same regardless of substitution. The associated surface is plotted and the value of ρ determined (the colour gradient in Fig. 3.9d illustrates the location of the specific point). For the mono-substituted boranes, the (3,-1) LP CP chosen is located opposite to the substituent. For boranes with increased substitution lacking these critical points, the corresponding value from borane was used. This was deemed satisfactory as for the mono-substituted boranes only small variations of the $\nabla^2\rho$ isosurface values are observed and negligible differences in ρ values resulted from their use compared to the use of the BH_3 $\nabla^2\rho$ isosurface value (for example, $0.118 \text{ e}\cdot\text{\AA}^{-3}$ instead of $0.120 \text{ e}\cdot\text{\AA}^{-3}$ for **6** and $0.106 \text{ e}\cdot\text{\AA}^{-3}$ instead of $0.102 \text{ e}\cdot\text{\AA}^{-3}$ for **15**).

Table 3.3 gives the electron density values obtained from the ρ -on- $\nabla^2\rho$ approach and the underlying Laplacian isosurface values. Whereas the value of the (3,-1) LP CP (which defines the isosurface) exhibits only slight variations, the resulting values of the electron density above boron varies rather widely.

For halogen mono-substituted boranes **2-4**, the ρ value increases moving down the family, in analogy to the B $2p_z$ occupancy from Table 3.2. It is unclear why **2** and **5** possess similar density values, especially considering the difference in the qB charge values. This issue between mono- and trisubstitution does not occur for the methyl substituent (**6-8**), but recurs somewhat for methoxyl substitution (**9-11**). The overall picture that emerges again follows that from Table 3.2. Boranes with π -electron donating groups (**2-5**, **9-14**, and **19** and **20**) exhibit larger ρ values above boron than those without (**6-8** and **15-17**). The trisubstituted **18**, possessing both donating and

withdrawing groups, exhibits by far the highest ρ value (reflective of its high B $2p_z$ occupancy) and will be further discussed in Sections 3.3.2 and 3.3.3.

Table 3.3: Selected QTAIM results for mapping the electron density, $\rho(\mathbf{r})$, onto an isosurface of its Laplacian, $\nabla^2\rho(\mathbf{r})$: $\nabla^2\rho$ isosurface ($\text{e}\cdot\text{\AA}^{-5}$) and electron density ($\text{e}\cdot\text{\AA}^{-3}$) for boranes **1-20**. The charge on boron, $q\text{B}$ (au), is presented as well.^{a,b}

	qB	$\nabla^2\rho$ isosurface^c	$\rho(\mathbf{r})$^d
1	1.869	1.42	0.100
2	2.063	1.44	0.146
3	1.906	1.44	0.158
4	1.785	1.42	0.162
5	2.438	1.42 ^e	0.145 ^f
6	1.903	1.46	0.120
7	1.934	1.42 ^e	0.129 ^f
8	1.960	1.42 ^e	0.133 ^f
9	2.017	0.143	0.188
10	2.176	1.42 ^e	0.239 ^f
11	2.345	1.42 ^e	0.221 ^f
12	2.030	1.45	0.176
13	2.189	1.42 ^e	0.198 ^f
14	1.973	1.42	0.193
15	1.958	1.37	0.102
16	1.923	1.41	0.115
17	1.930 (1.959) ^g	1.57 (1.33) ^g	0.190 (0.109) ^g
18	2.244	1.42 ^e	0.422 ^f
19	1.975	1.42 ^e	0.175 ^f
20	2.366	1.42 ^e	0.184 ^f

^a From PBE0/6-311++G(2d,p). ^b See Fig. 3.4 for structures. ^c See Fig. 3.8 for choice of $\nabla^2\rho$ isosurface. ^d The “ ρ -on- $\nabla^2\rho$ ” value, see text. ^e BH_3 $\nabla^2\rho$ value, see text. ^f Obtained from the BH_3 $\nabla^2\rho$ value, see text. ^g Values from the constrained geometry of BH_2NO_2 , see text.

The QTAIM charges, like the NBO charges, do not seem to have any particular trend. A comparison of the computed charges using these two methods can be found in S 3 of Appendix A.

3.3.2. Acetophenone-borane complexes

Geometries and structures:

The carbonyl oxygen of acetophenone can complex to an electron-deficient boron atom of a borane. Selected geometric parameters of complexes **1k-20k** are summarised in Table 3.4, and their molecular graphs are shown in Figs. 3.10 and 3.11. The notation of the complexes follows that of the boranes, with an added **k** to signify complexation to a ketone, acetophenone.

Borane-acetophenone complexation will occur through a B \cdots O interaction, with potentially different conformations. Firstly, the boron atom and the phenyl group can be *anti* (B-O-C_{C=O}-C_{Ph} 180°) or *syn* (B-O-C_{C=O}-C_{Ph} 0°). Secondly, with the addition of substituents on boron, the R-B-O-C_{C=O} dihedral angle can describe different conformational arrangements.

A conformational search was performed through a series of relaxed scans on **2k** by twisting the B-O-C_{C=O}-C_{Ph} and F-B-O-C_{C=O} dihedral angles in 10° increments (Fig. 3.12). The torsions confirm that the global minimum of **2k** is as given in Fig. 3.10. As the B-O-C_{C=O}-C_{Ph} is twisted from 180° to 0° an increase in the B-O-C angle (125.3° to 139.4°, respectively) is observed. The distortion of the B-O-C angle towards a more linear geometry causes a small increase in energy⁹². Further difference in energy is most likely due to steric hindrance. A second conformer is located at a F-B-O-C_{C=O} dihedral of 50° and is destabilized by approximately 0.5 kcal·mol⁻¹. It exhibits a C $_{\alpha}$ -H \cdots F interaction that is also present in the global minimum of **5k** (Fig. 3.10), where it cannot be avoided.

Table 3.4: Selected geometric properties (distances in pm, dihedral angles and bond angles in °) in complexes **1k-20k**, from PBE0/6-311++G(2d,p).^a

	B···O	C=O	B···O=C-C_{Ph}	ΣR-B-R
1k	157.5	124.3	-179.87	339.4
2k	159.2	124.3	180.0	342.2
3k	155.9	124.6	180.0	337.8
4k	154.8	124.7	180.0	336.4
5k	164.3	124.0	180.0	343.5
6k	161.9	123.7	-179.0	341.6
7k	168.4	123.2	180.0	342.4
8k	175.1	122.9	180.0	344.8
9k	167.2	123.8	177.7	344.7
10k	293.5	121.4	152.5	359.9
11k	304.3	121.3	180.0	359.9
12k	170.6	123.7	178.4	346.6
13k	290.9	121.4	-153.9	359.9
14k	336.9	121.2	-177.7	360.0
15k	150.9	126.9	180.0	331.1
16k	155.4	124.7	180.0	335.9
17k	152.1	124.7	180.0	333.2
18k	160.8	125.0	153.2	339.7
19k	157.4	124.7	-177.0	338.2
20k	162.9	124.0	179.0	346.4

^a See Figs. 3.9 and 3.10 for structures.

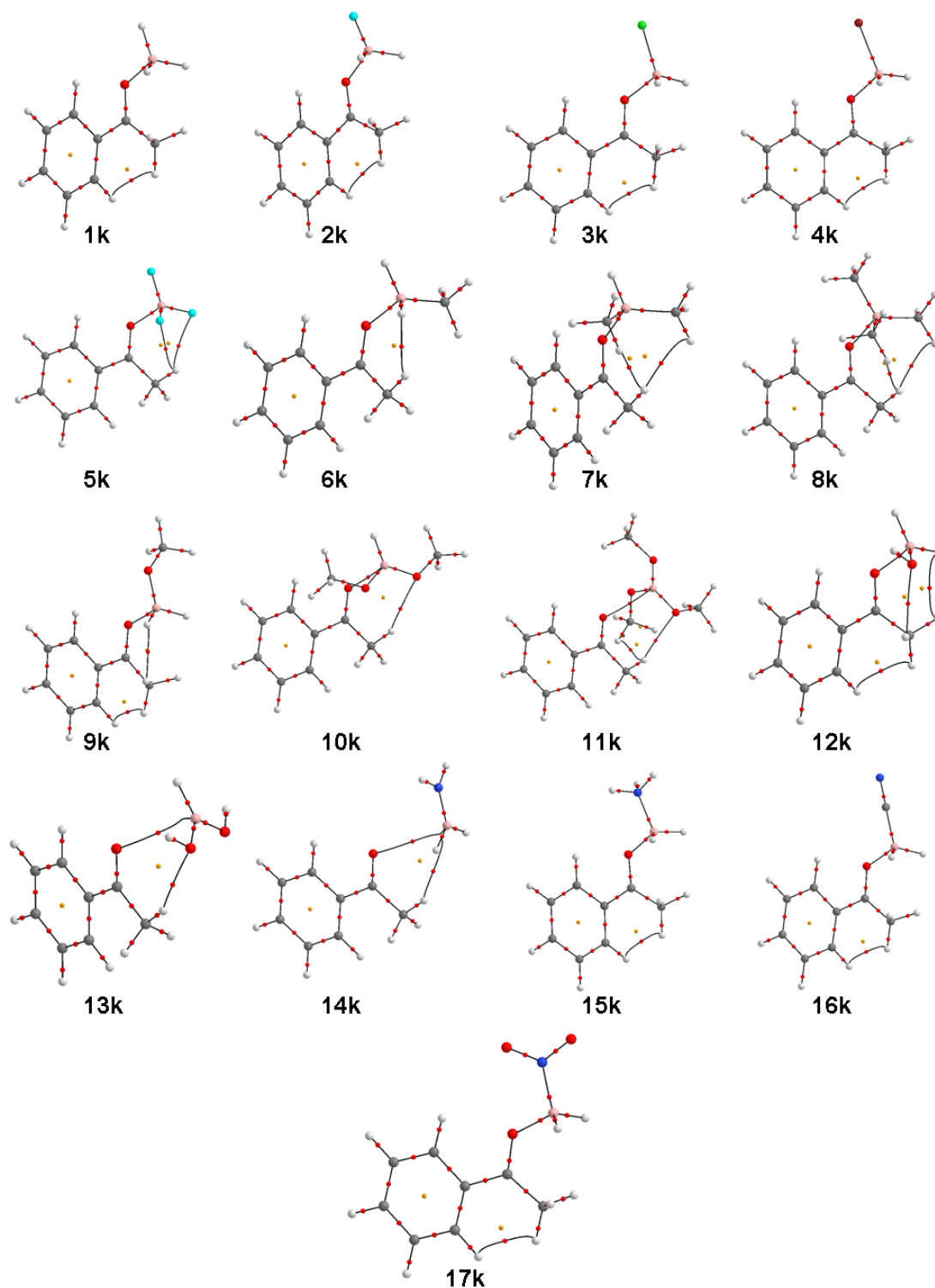


Figure 3.10: Molecular graphs of substituted borane-acetophenone complexes **1k-17k**, from PBE0/6-311++G(2d,p). Atoms are represented by large spheres: carbon (grey), hydrogen (white), oxygen (red), nitrogen (blue), boron (pink), fluorine (cyan), chlorine (lime green) and bromine (maroon). Bond critical points are indicated by small red spheres, ring critical points by small yellow spheres and cage critical points by small green spheres.

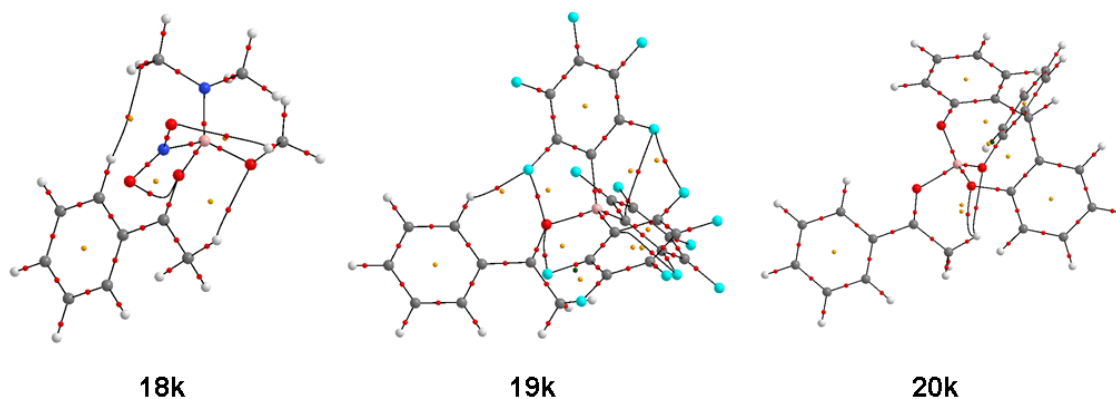


Figure 3.11: Molecular graphs of substituted borane-acetophenone complexes **18k-20k**, from PBE0/6-311++G(2d,p). Atoms are represented by large spheres: carbon (grey), hydrogen (white), oxygen (red), nitrogen (blue), boron (pink), fluorine (cyan), chlorine (lime green) and bromine (maroon). Bond critical points are indicated by small red spheres, ring critical points by small yellow spheres and cage critical points by small green spheres.

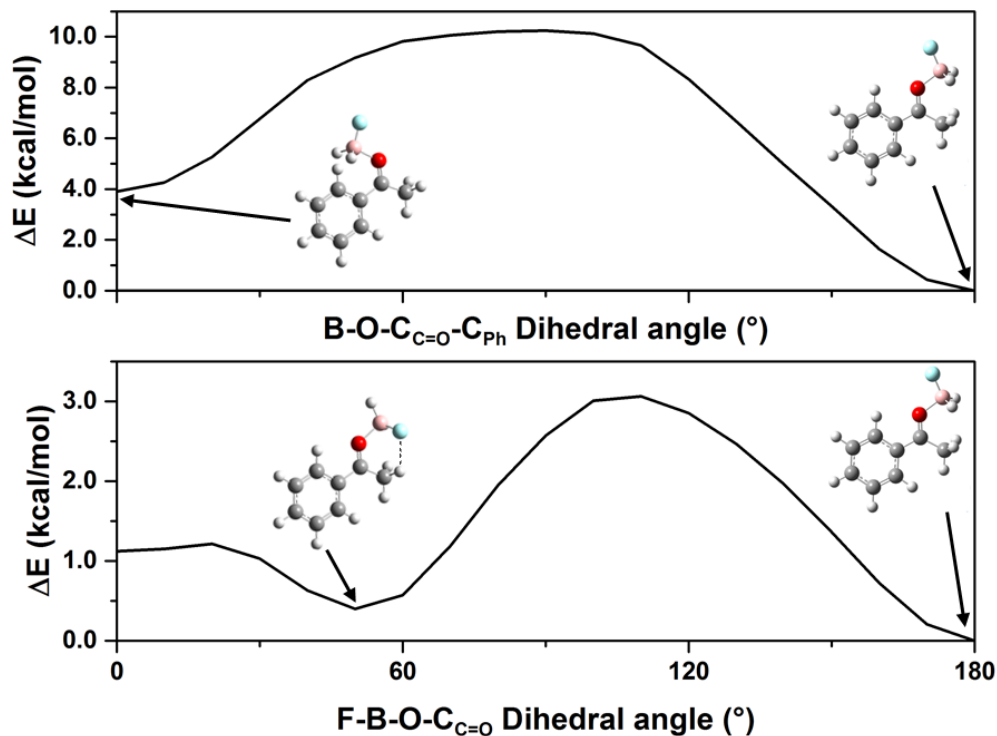


Figure 3.12: Relative energies for relaxed scans of dihedral torsions in a conformational search for the fluoroborane-acetophenone complex **2k**. Torsion (in 10° increments) of the (top) B-O-C_{C=O}-C_{Ph} dihedral and (bottom) F-B-O-C_{C=O} dihedral. Structures shown represent minima. Dashed line added using Gaussview software⁹³. Atoms are represented by large spheres: carbon (grey), hydrogen (white), oxygen (red), fluorine (cyan) and boron (pink). From PBE0/6-311++G(2d,p).

Table 3.4 allows a sorting into distinct sets of binding. The borane coordinates closely ($B\cdots O$ distance below 180 pm) with acetophenone in most complexes analyzed, causing the once trigonal planar boron geometry to become tetrahedral (as given through the sum of the three bond angles on boron, $\Sigma R-B-R$, without considering $B\cdots O$). With the $B\cdots O$ distance much longer than the standard standard single-bond length of 137 pm⁹⁴, the coordinating bond is not a fully formed single bond. In contrast, very weak binding is observed in **10k** (dimethoxyl), **11k** (trimethoxyl), **13k** (dihydroxyl) and **14k** (amino), with $B\cdots O$ distances greater than 290 pm. These boranes remain trigonal planar, in accord with their high B $2p_z$ occupancy (Table 3.2) and their congruently large $\rho\text{-on-}\nabla^2\rho$ value (Table 3.3), and are clearly not to be considered electron-deficient. Along with the geometry values above, the $\rho\text{-on-}\nabla^2\rho$ value seems better suited for the sorting of borane complexes into the two sets of binding. For example, the trifluoroborane in **5k**, if uncoordinated, possesses the same B $2p_z$ value as the dihydroxylborane (**13**), however its boron atom still shows a tetrahedral environment, and the $B\cdots O$ distance in **5k** is still short, marking trifluoroborane as possessing an electron-deficient boron. This is well reflected in the smaller $\rho\text{-on-}\nabla^2\rho$ value of **5** as compared to that of **13** (Table 3.3).

Complexes **11k** and **13k**, despite their large $B\cdots O$ distances (292.7 pm and 306.9 pm respectively), maintain a $C_\alpha\text{-H}\cdots O$ interaction to the methyl group on acetophenone (Fig. 3.13). As demonstrated through the fact that complexes for the electron-rich boranes **11** and **13** are located at all, these interactions (shown by black arrows), though weak, stabilize the complexes. In addition to the $C_{CH_3}\text{-H}\cdots O$ interaction, **13k** demonstrates stabilizing $C\text{-H}\cdots H\text{-C}$ contacts between the methoxyl and methyl groups. Complexes **10k** and **12k** also show evidence of $C_\alpha\text{-H}\cdots O$ interactions.

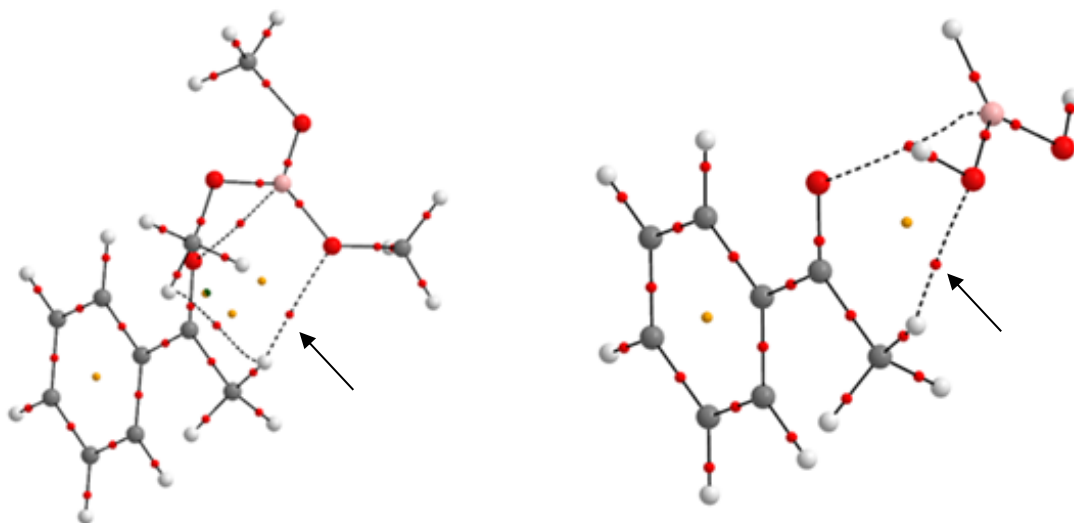


Figure 3.13: Molecular graphs of acetophenone-borane complexes **11k** and **13k**, highlighting the weak interactions (arrows indicate $C\alpha-H\cdots O$). Atoms are represented by large spheres: carbon (grey), hydrogen (white), oxygen (red) and boron (pink). Bond critical points are indicated by small red spheres, ring critical points by small yellow spheres and a cage critical point by a small green sphere. From PBE0/6-311++G(2d,p).

Finally, the carbonyl oxygen in **17k** seems to be more suitable for interaction with the boron atom in **17** than the oxygen atom of its nitro group, because Fig. 3.10 illustrates the displacement of the latter and the change in geometry of the nitro group from Fig. 3.4.

Energies:

The binding energies of the complexes as well as selected electronic properties are summarised in Table 3.5. For all complexes, the basis set superposition error (BSSE) calculated with PBE0/6-311++G(2d,p) ranges from 0.1 to 2.5 kcal·mol⁻¹, while the zero-point vibrational energy ranges from 0.3 to 3.7 kcal·mol⁻¹. As expected, the addition of the BSSE correction (and zero-point vibrational energies) yields weaker interaction energies but does not alter the relative interaction strengths in the acetophenone complexes.

The MP2 binding energies, though they can be higher or lower than those from PBE0, are in general good agreement, and the ordering of the binding energies remains mostly consistent. Due to their size, complexes **18k**, **19k** and **20k** were not computed using MP2/6-311++G(2d,p). In addition, minima for complexes **10k**, **11k** and **13k** with the boron atom bound to the carbonyl oxygen were not present using MP2/6-311++G(2d,p). The calculated binding energy of **12k** using MP2/6-311++(2d,p) is drastically different to the one calculated with PBE0/6-311++(2d,p). This is in part due to geometrical changes in the two optimized complexes. However, it is unclear at this time the exact nature of the large energy differences.

Complexation:

Bonding interactions between two atoms may be classified as shared or closed-shell, based on the values of ρ_{BCP} and $\nabla^2\rho_{\text{BCP}}$ ⁷⁸. Generally, shared interactions, such as covalent bonds, are characterised by relatively large values of ρ_{BCP} (on the order of $10^{-1} \text{ e}\cdot\text{\AA}^{-3}$) and a negative value of $\nabla^2\rho_{\text{BCP}}$, while closed-shell interactions are characterised by a lower value of the electron density (on the order of $10^{-1} - 10^{-2} \text{ e}\cdot\text{\AA}^{-3}$) and a positive value of the $\nabla^2\rho_{\text{BCP}}$.

The ρ_{BCP} and $\nabla^2\rho_{\text{BCP}}$ values for the B \cdots O interaction in complexes **1k-20k** are reported in Table 3.5. All $\nabla^2\rho_{\text{BCP}}$ values are positive, and thus all B \cdots O interactions might be considered closed-shell, in accord with a dative nature, despite the large ρ_{BCP} values of the more tightly bound complexes. As already judged from the geometric changes, an electronic effect of a substituent on the boron atom is reflected in the electron density, and therefore strength, of the B \cdots O interaction, and effects are additive as more groups on boron are introduced. The effect can be small, as on going from **2k** to **5k**, or dramatic (**9k** to **11k**), according to the available π -electron donating capacity (here methyl versus methoxyl).

Table 3.5: Uncorrected and corrected binding energies ($\text{kcal}\cdot\text{mol}^{-1}$) and selected electronic properties (electron density in $\text{e}\cdot\text{\AA}^{-3}$, Laplacian in $\text{e}\cdot\text{\AA}^{-5}$) at the bond critical point of the $\text{B}\cdots\text{O}$ interaction in complexes **1k-20k**, from PBE0/6-311++G(2d,p).^{a,b}

	$E_{\text{bind}}^{b,c}$	$E_{\text{bind}}^{\text{CC},d}$	$E_{\text{bind}}^{\text{CC+ZPVE},e}$	q_{B}	ρ_{BCP}	$\nabla^2\rho_{\text{BCP}}$
1k	22.0(18.6)	21.6	17.9	1.861	0.702	13.62
2k	13.9(11.2)	13.1	10.6	2.075	0.702	10.83
3k	17.5(16.1)	16.6	13.9	1.933	0.768	13.32
4k	19.1(18.1)	18.3	15.7	1.823	0.792	13.12
5k	13.8(13.5)	12.1	10.7	2.428	0.668	5.89
6k	13.7(14.0)	13.2	10.0	1.894	0.616	11.74
7k	5.4(8.8)	4.9	2.2	1.921	0.519	9.07
8k	1.3(6.9)	0.7	-1.7	1.943	0.444	6.66
9k	2.7(4.0)	2.0	0.5	2.050	0.576	7.54
10k	2.4	1.8	1.4	2.185	0.055	0.62
11k	1.4	0.8	0.5	2.350	0.043	0.54
12k	3.8(20.2)	3.1	1.1	2.047	0.532	6.42
13k	2.6	2.1	1.6	2.195	0.057	0.64
14k	0.5(1.7)	0.4	0.1	1.981	0.024	0.30
15k	65.3(61.4)	64.6	60.9	1.991	0.908	14.08
16k	28.0(25.8)	27.4	24.3	1.934	0.770	13.46
17k	25.7(25.2)	24.8	22.3	1.976	0.848	14.75
18k	-4.2	-5.8	-6.6	2.281	0.714	7.64
19k	12.4	9.9	8.4	1.994	0.751	11.35
20k	10.4	9.0	8.1	2.375	0.680	6.94

^a See Figs. 3.9 and 3.10 for structures. ^b Values from MP2/6-311++G(2d,p) in parentheses. ^c Uncorrected binding energy. ^d Including counterpoise correction. ^e Including counterpoise and zero-point vibrational energy corrections.

The exponential dependence between ρ_{BCP} and distance has been reported, and it provides a measure of the strength of the interaction^{29,43}. This relationship is once again, over a large range, observed for the $\text{B}\cdots\text{O}$ interaction in Figure 3.14a, where higher density values relate to shorter distances. The substantial gap in the two sets of data points further illustrates the two modes of binding (strong and weak interactions) observed from the $\text{B}\cdots\text{O}$ distance from Table 3.4.

Interestingly, it is unclear if the gap could be bridged through a judicious choice of substituents on the borane. Figure 3.14b, which evaluates whether the strength of the B \cdots O interaction as given by its electron density can be related to the change in charge on boron upon complexation, demonstrates that the range in Δq_B is the same for both sets of complexes, strongly bound or not. As the change in $\rho(\text{B}\cdots\text{O})$ within a set is small, only the fact that two sets of complexes exist can be learned from the plot. With q_B of the boranes instead of Δq_B , a scatter plot is obtained (not shown). Overall, and not surprisingly, q_B , which as a charge does not allow a distinction between σ - and π -effects that give rise to its changes, is a poor choice for observing dependencies in these complexes.

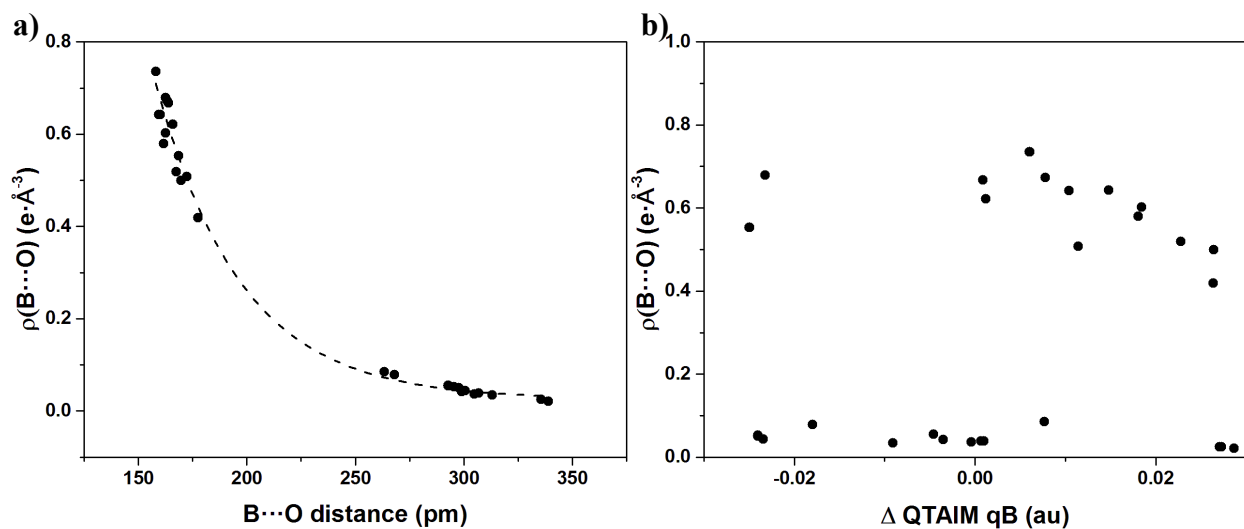


Figure 3.14: Structural and electronic relationships in borane-acetophenone complexes: a) expected exponential relation between ρ_{BCP} and distance^{29,43}; b) scatter plot between ρ_{BCP} and the change in charge upon complexation, Δq_B (borane minus borane-complex).

In contrast to the failure of q_B , the binding energy can be related to the B $2p_z$ occupancy. Figure 3.15 shows that, as expected, an increase in B $2p_z$ orbital occupancy results in a decrease

in binding. Thus, once the electron demand on boron is met through substitution, $B\cdots O$ complexation is prevented.

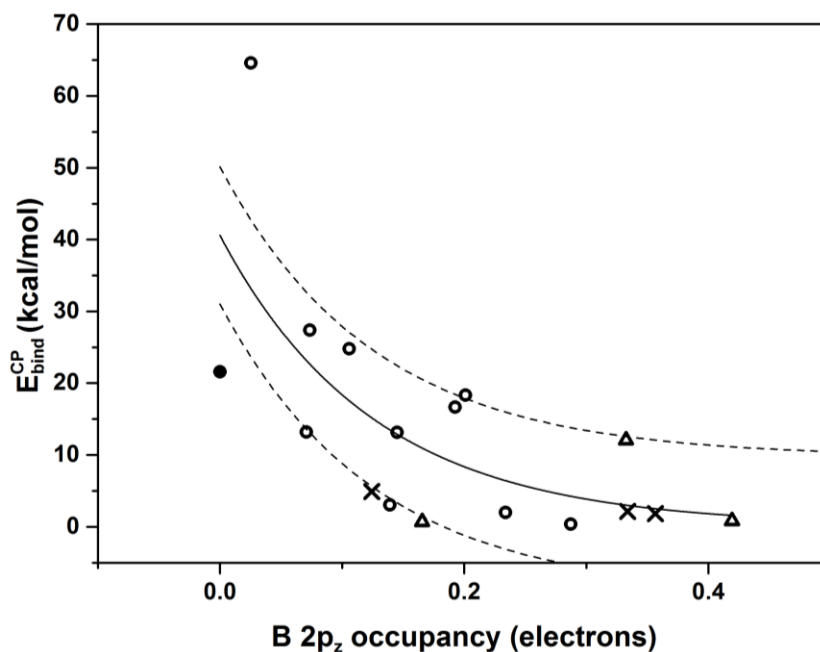


Figure 3.15: Relationship between counterpoise-corrected binding energy in a set of borane-acetophenone complexes and B $2p_z$ occupancy for the corresponding set of boranes. Symbols are BH₃ (●), mono-substituted (○), di-substituted (×) and tri-substituted (Δ) boranes. The y-error incorporated by dashed lines represents $\pm 1 \sigma_y$ of the fitted curve.

While the B $2p_z$ occupancy offers a somewhat satisfactory explanation of the changes in binding energy (Fig. 3.15), utilizing the ρ -on- $\nabla^2\rho$ values above B provides a slightly tighter fit and strengthens the viability of the here-derived methodology, and this holds for the relation with binding free energies as well (Fig 3.16).

Some outliers warrant further analysis and are discussed here with their counterpoise-corrected binding energies (Fig. 3.16 top). While **1k** (●) falls just outside the y-error (dashed lines), its x-uncertainty places it within.

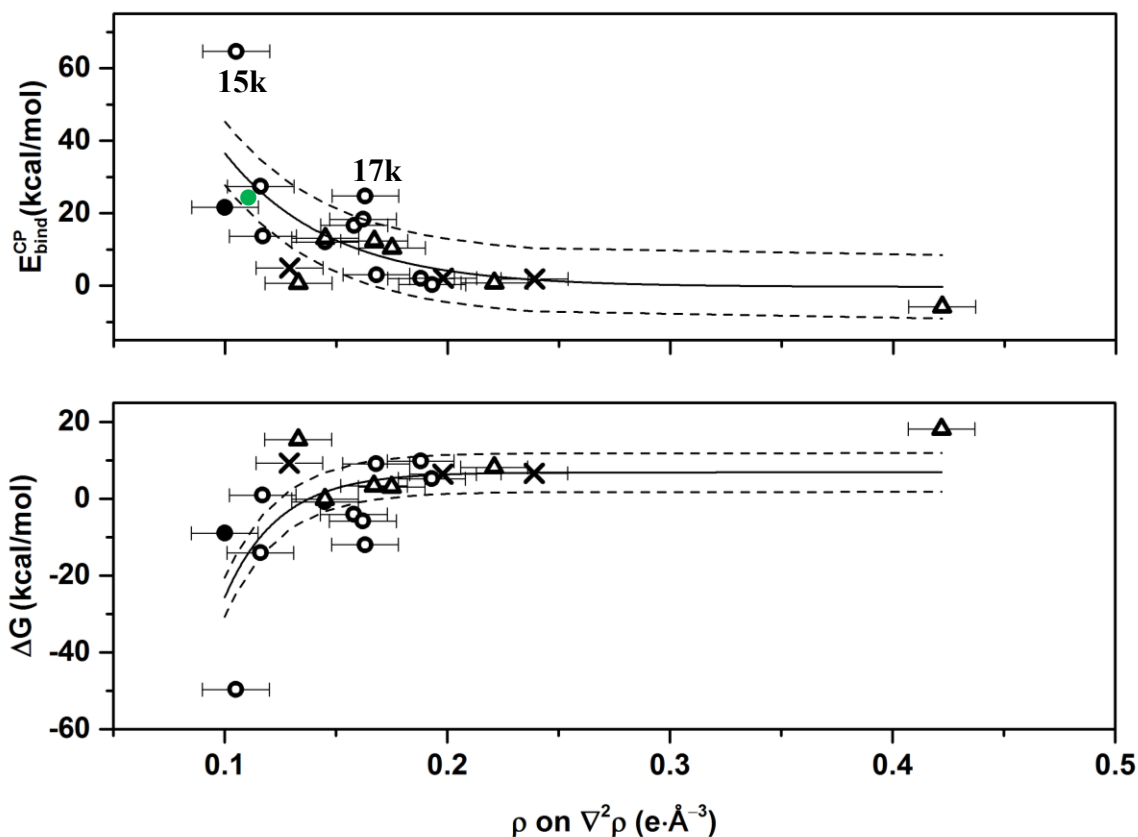


Figure 3.16: Relationship between binding (free) energies in borane-acetophenone complexes and ρ -on- $\nabla^2\rho$ values on boron in the corresponding set of boranes. Symbols are BH_3 (\bullet), mono-substituted (\circ), di-substituted (\times) and tri-substituted (Δ) boranes. The position of the “corrected” nitroborane density value from its restrained geometry is given by (\bullet) (see text for details). x-error bars represent the largest error ($0.015 e\cdot\text{\AA}^{-3}$, from **17**) identified in the determination of ρ -on- $\nabla^2\rho$ values. y-error incorporated by dashed lines represented $\pm 1 \sigma_y$ of the fitted curve.

As previously mentioned, the bent geometry of nitroborane (**17**, Fig. 3.17a) is not maintained after complexation (Fig 3.16c). As such, the $\text{B}\cdots\text{O}$ interaction in **17** results in a misleadingly large ρ -on- $\nabla^2\rho$ value. The more appropriate ρ -on- $\nabla^2\rho$ value of the restrained geometry (Fig. 3.17b) falls almost exactly on the fitted trendline (\bullet).

The set of outliers belonging to **6k**, **7k** and **8k**, i.e., the methyl-substitution series, follows a predictable pattern (Fig 3.18). The increasing substitution on the boron atom causes more crowding upon re-hybridization and results in a decrease (exponential digression) in the binding energy of the complexes. Figure 3.19 demonstrates that contacts between methyl substituents on

borane and ketone moieties are only avoided for mono-substitution (**6k**); **7k** and **8k** exhibit C-H \cdots H-C contacts, which, while still stabilizing, are repulsive (see S5 of Appendix A for the graphical definition of a stabilizing-repulsive interaction).

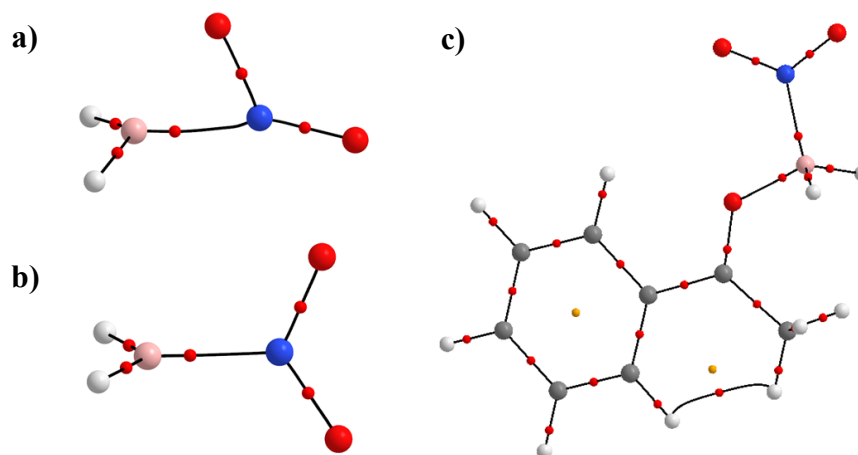


Figure 3.17: Molecular graphs of the a) nitroborane (**17**) optimized geometry, b) nitroborane constrained geometry, and c) optimized nitroborane-acetophenone complex (**17k**), from PBE0/6-311++G(2d,p). Atoms are represented by large spheres: carbon (grey), hydrogen (white), oxygen (red), nitrogen (blue) and boron (pink). Bond critical points are indicated by small red spheres, ring critical points by small yellow spheres.

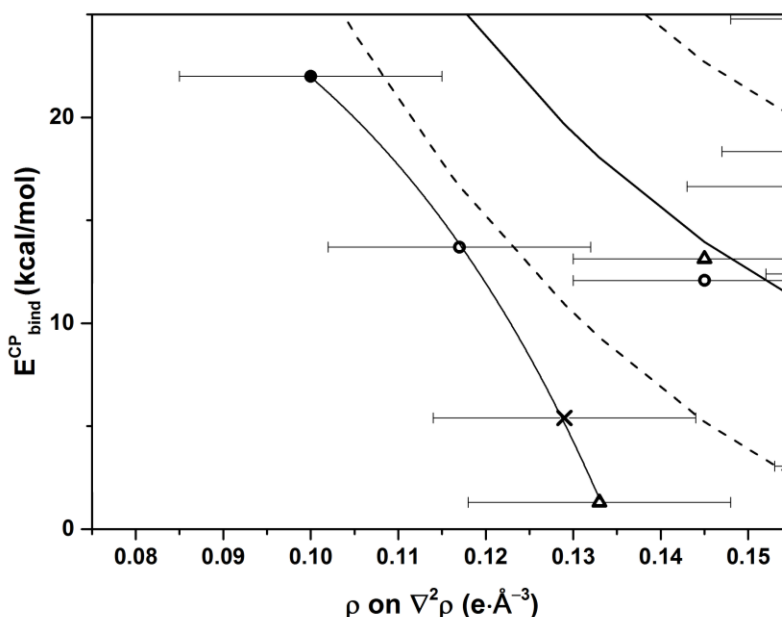


Figure 3.18: Relationship between counterpoise-corrected binding energy in methyl-substituted borane-acetophenone complexes **6k-8k** and ρ -on- $\nabla^2\rho$ values on boron in the corresponding set of boranes. Symbols used are borane (●), methylborane (○), dimethylborane (×) and trimethylborane (Δ).

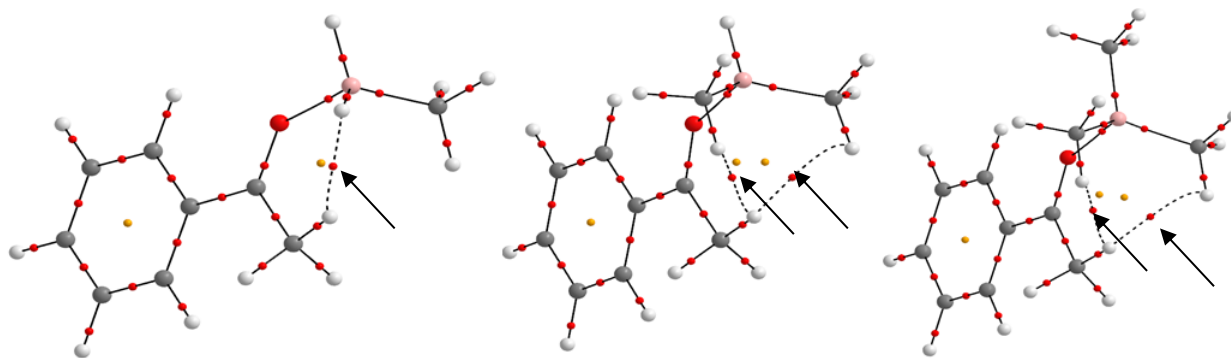


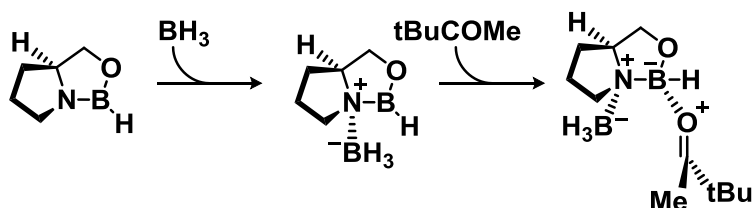
Figure 3.19: Molecular graphs of methylborane-acetophenone complexes **6k-8k** highlighting the weak interactions (arrows indicate H···H contacts). Atoms are represented by large spheres: carbon (grey), hydrogen (white), oxygen (red) and boron (pink). Bond critical points are indicated by small red spheres, ring critical points by small yellow spheres. From PBE0/6-311++G(2d,p).

Boranes with N and O substitution, such as $\text{BHOCH}_3\text{N}(\text{CH}_3)_2$ or $\text{BCH}_3\text{OCH}_3\text{N}(\text{CH}_3)_2$, are unable to bind to acetophenone (and are therefore not included in Section 3.3.1). With their much higher $\rho\text{-on-}\nabla^2\rho$ values ($0.281 \text{ e}\cdot\text{\AA}^{-3}$ and $0.306 \text{ e}\cdot\text{\AA}^{-3}$, respectively), it would seem that a $\rho\text{-on-}\nabla^2\rho$ cut-off value for binding to boron could be established. However, the introduction of the electron-withdrawing nitro group in **18** leads to **18k**, despite the still higher $\rho\text{-on-}\nabla^2\rho$ value of $0.422 \text{ e}\cdot\text{\AA}^{-3}$. An interpretation for this is currently unavailable.

Finally, knowledge of the exact electron demand on boron in a borane can be beneficial to the experimental chemist. For example, in the CBS reduction of prochiral ketones, the crucial ketone complexation only proceeds upon prior addition of borane, and this is correctly attributed to the B=N character in the oxazaborolidine⁹⁵⁻⁹⁷. Scheme 3.1 shows the process for an unsubstituted oxazaborolidine catalyst and *t*-butyl methyl ketone, which will be discussed in detail in Chapter 4.

From the point of view of the electron density, such a system can be readily analyzed and understood and, if necessary, modified through further substitution (e.g., on boron). From the above, it seems that substituted boranes with $\rho\text{-on-}\nabla^2\rho$ on boron of less than $0.19 \text{ e}\cdot\text{\AA}^{-3}$ bind and

those with greater values do not. With the participation of the nitrogen electron lone pairs, ρ -on- $\nabla^2\rho$ on boron in the oxazaborolidine is $0.346 \text{ e}\cdot\text{\AA}^{-3}$, a high value that precludes ketone complexation. The coordination of borane to the oxazaborolidine nitrogen atom causes this value to decrease to $0.194 \text{ e}\cdot\text{\AA}^{-3}$, a value for which, within error, complexation becomes possible.



Scheme 3.1: Reaction scheme of a *t*-butyl methyl ketone reduction catalyzed by an unsubstituted oxazaborolidine catalyst using borane.

3.4. Conclusions

For a set of boranes with widely differing electron demand on boron, as dictated through the choice of substituents, NBO and NRT calculations corroborate Lewis structures that attempt to satisfy the electron demand on boron. As expected, π -electron donating groups fill the empty B $2p_z$ orbital through resonance, and less effective hyperconjugative interactions are also demonstrated in cases where π -electron donation is impossible. Decreasing the electron demand on boron through π -electron donating groups decreases the strength of the $\text{B}\cdots\text{O}$ interaction in complexes between boranes and acetophenone and can lead to loss of complexing ability.

The quantification of a binding cut-off was determined by evaluating the relation between the binding energy and the estimated π -electron density within the B $2p_z$ orbital. From an NBO analysis, substituted boranes with a B $2p_z$ occupancy of less than 0.25 electrons bind acetophenone; from an electron density analysis, the cut-off is $0.19 \text{ e}\cdot\text{\AA}^{-3}$.

In the question on whether or not a ketone will bind to a borane a degree of quantification thus has been achieved; it remains to be seen if this holds for a range of different ketones and a wider selection of boranes.

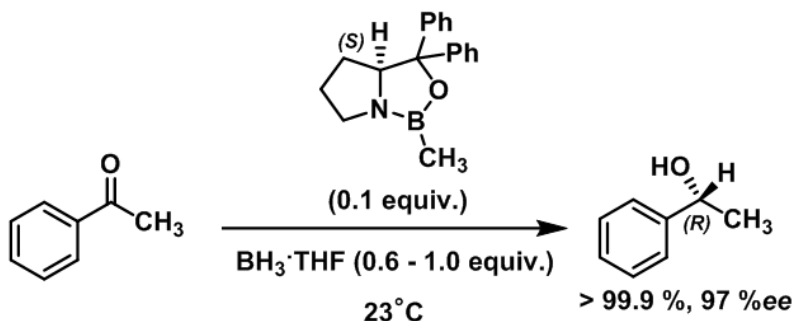
Chapter 4.

Origin of the enantioselectivity in the *t*-butyl methyl ketone reduction with a chiral oxazaborolidine catalyst

4.1. Introduction

A key task in the life sciences is the understanding of molecular chirality because it dictates life at the molecular level. All of life's building blocks (proteins, enzymes, DNA, RNA) are chiral, and so are most substrates with which these macromolecules interact within our bodies. Most medicinal drugs nowadays are administered enantiomerically pure. While isolation of the desired enantiomer from a (racemic) mixture is often feasible, the challenge for the chemical community is its enantioselective synthesis, as recognized in the 1990 Nobel Prize in Chemistry to Corey as well as the 2001 Nobel Prize in Chemistry to Sharpless, Noyori and Knowles. Thus, providing the necessary chiral information through a chiral catalyst has become an important methodology for the formation of chirality from prochiral compounds^{23,98,99}. Synthetic organic chemists are developing an ever larger number of reactions that proceed with high to very high enantioselectivities. Yet, the origin of the enantioselectivity from a prochiral compound is usually not understood, and it is one of the largely unexplored fields in computational organic chemistry. The approach to simply determine the transition state of lower free energy and then argue via this lower free energy is insufficient; rather, the interactions that lead to the energetic differentiation in the two transition states need to be explored if any useful insight for predictive purposes is to be gained.

As an example, in a keystone study for the field, Houk has speculated on such interactions in the enantioselective hetero Diels-Alder addition between a prochiral diene and a prochiral aldehyde under catalysis with a chiral catalyst¹⁰⁰. The seminal experimental work by Rawal, using a diol (TADDOL) as a chiral solvating agent, demonstrated extraordinarily high enantioselectivities^{101,102}. A coordinating hydrogen bond between the TADDOL catalyst and benzaldehyde, the first point of interaction, was determined from a crystal structure¹⁰³. A second point of interaction, in the form of a C-H... π interaction was determined by computational work, precluding free rotation of the aldehyde within the complex and leading to one of the carbonyl faces being hindered for attack by the diene¹⁰⁰. This work followed two computational models that had recently appeared in the literature where ONIOM:PM3¹⁰⁴ and molecular mechanics based docking methods^{105,106} had been used to study the TADDOL catalyzed reaction. Houk's conclusions, for the second anchoring point, were attained based on the proximity of the aldehydic hydrogen to a naphthyl group on the TADDOL catalyst. While Houk states that the M06-2X method has been found to accurately compute weak dispersion type interactions¹⁰⁷, their physical and electronic properties within the complex were never evaluated. Additionally, a more extensive conformational search of the complexes that lead to the hetero Diels-Alder product is lacking and therefore more work is needed to accurately investigate such a reaction and its source of facial selectivity. It is important to note that while Houk's work may have certain shortcomings, the underlying notion offers ideas to consider when investigating other systems that may contain similar weak interactions to ensure they are not overlooked.



Scheme 4.1: CBS reduction of acetophenone using a chiral oxazaborolidine catalyst with borane in THF. (Redrawn from ref. 40)

We are interested in applying these types of studies to other enantioselective reactions that involve other chiral catalysts. For example, the hydroboration of terpenoids has provided a range of chiral boranes that act as valuable chiral reducing agents^{108–113}. One such chiral framework is the oxazaborolidine catalyst developed by Corey, Bakshi and Shibata (the CBS catalyst, after its developers)⁹⁵. After extensive experimental evidence, a mechanism for the enantioselective reduction of prochiral ketones with borane catalyzed by the CBS oxazaborolidine catalyst was formulated^{95,114–116}. According to the authors, this mechanism provides explanations for the regioselectivity (in case multiple carbonyl groups are available in the reactant), enantioselectivity (R configuration), rate enhancement and catalyst turnover of the reduction^{40,95,114}. With respect to the enantioselectivity, though, the proposed mechanism only provides information on a single point of interaction, between the catalyst's boron atom and the carbonyl oxygen. While this interaction is critical, it leaves unaddressed the question of rotational freedom of the ketone within the complex, a question that is at the heart of the observed enantioselectivity.

Previous work by Nevalainen on the quantum chemical modeling of chiral catalysis provides preliminary work on mostly smaller modelled systems using *ab initio* calculations^{96,97,117–133}. These systems range from simple boranamine-borane adducts to larger substituted (typically alkyl or aryl) CBS-borane structures. Additionally, Nevalainen studied the reduction of

formaldehyde, acetaldehyde, acetone as well as some prochiral ketones which were reported to have high enantiomeric excess⁹⁵. In his work, Nevalainen confirmed Corey's speculation that the formation of the catalyst-borane adduct was exothermic and that the adducts did indeed adopt a cis configuration upon complexation (with respect to the hydrogen on the asymmetric carbon of the catalyst framework) of BH₃ with the catalyst in contrast to a trans configuration^{40,96,134,135}. Additionally, various ketone orientations with B...O connectivity were obtained, yet little importance was placed on the B-O-C-R_{large} torsion angle for the generation of additional complexes. Finally, a computational explanation for the dimeric aggregates of the oxazaborolidine catalysts was provided based on their speculation from previous NMR experiments⁹⁵. In his studies, Nevalainen focused on the characterization of the intermediates rather than the transition states.

A conflict between the Nevalainen assertion that ketone complexation was endothermic¹²¹ and Corey's statement that the complexation was highly exothermic⁹⁵ brought upon the interest of Alagona and co-workers, who confirmed the endothermicity¹³⁶. Based on accurate reproductions of experimental enantiomeric excess on the substituted catalyst, Alagona speculated that the CBS reduction could be used and exploited to predict stereoselectivity in reduction compounds not yet carried out experimentally¹³⁷. However, once again there was no insight into a possible second site of anchoring that would "lock-in" the ketone for a favoured pre-orientation to yield the observed enantiomer.

Certain experimental findings, such as a drop in enantioselectivity from 97 to 28 %ee when the diphenyl substituted CBS catalyst is replaced with one that possesses di(*ortho*-anisyl) substitution in the reduction of acetophenone⁴⁰, raised our interest in pursuing the source of

enantioselectivity of the CBS reduction by investigating the weak interactions that lead to the differences in the transition state barriers.

As our first step in this work, reported here, computational methods are used to investigate the pre-reaction complexes and transition states of the un-substituted CBS catalyst with *t*-butyl methyl ketone. Previously, the un-substituted catalyst has been studied by Li computationally^{138,139}. Li established that while Nevalainen's work supported Corey's mechanism of the enantioselective reduction, several intermediate complexes, such as the catalyst-borane-ketone and catalyst-alkoxyborane adducts, were not well described¹³⁸ and needed to be explored for a better understanding of the reaction process. While the work does not elucidate the source of facial selectivity of the reduction reaction, much structural information is provided as well as NBO^{79,80} (Natural Bond Orbital) results that proved to be an excellent starting point for this work.

With the hydride transfer as the rate-limiting step, the reduction relies on the chiral catalyst-borane adduct approaching the prochiral ketone from the preferred face. It thus becomes critical to establish, first, all reasonable ketone orientations within the complex. We will show that the often-assumed B \cdots O=C complexation⁴⁰, in fact, is disfavoured due to the reduced electron demand of the catalytic framework's boron atom and leads to only one particular set of reasonable ketone orientations.

4.2. Computational Details

All calculations were performed using the Gaussian09 program⁶⁵. Geometries were obtained using density-functional theory (DFT) using Becke's 3-parameter exchange functional and the Lee-Yang-Parr correlation functional (B3LYP)¹⁴⁰⁻¹⁴², the "parameter-free" hybrid DFT method

by Perdew, Burke and Ernzerhof (PBE0)⁶⁶⁻⁶⁹, and Head-Gordon's long-range corrected hybrid functional with dispersion correction (ω B97X-D)¹⁴³, all with the 6-31+G(2d,2p) basis set. Frequency analyses with the same model chemistries established the optimized geometries as being minima or first-order saddle points. Electronic and free energies are given in S1 of Appendix B. For a transition state, the connection to its corresponding pre-reaction complex was ascertained through an intrinsic reaction coordinate scan. In light of the involvement of weak interactions in the complexes, the B3LYP results were compared to those from PBE0, ω B97X-D and the second order Møller-Plesset (MP2) perturbation theory⁷⁰⁻⁷⁴. For this purpose, the basis set size was increased to 6-311++G(2d,p). Relaxed scans (energy profiles) were obtained for the B-N-B angle change in the catalyst-borane adducts in one-degree increments and the remaining geometry was allowed to fully optimize. The size of the basis set superposition error (BSSE) was evaluated using the counterpoise approach⁷⁵. The tabulated BSSE correction energies of selected complexes can be found in S2 of Appendix B.

Bonding interactions for each ketone complex and transition state were determined from computed electron densities, $\rho(r)$, using the program AIMAll⁷⁶ within the Quantum Theory of Atoms in Molecules (QTAIM)^{77,78}. Because of negligible differences between the computed $\rho(r)$ obtained from the different functionals used in this study, only the results from B3LYP/6-31+G(2d,2p) are presented here. Critical points in the topology of the electron density map onto established chemical entities: e.g., the position of a nucleus is represented, as expected, by an electron density maximum. In a molecule at minimum energy geometry, a line of maximum electron density (a so-called bond path) between two nuclei represents a bonding interaction. It is thus possible to determine which atoms are bonded, within and between molecules. Properties at the lowest-density point, the so-called bond critical point (BCP), along the bond path allow a

characterization of the nature of the bonding interaction. A large value of the electron density (ρ_{BCP}) and a negative value of its Laplacian (the second derivative of the electron density, $\nabla^2\rho_{\text{BCP}}$) indicate a shared interaction (or covalent bond), whereas a small value in ρ_{BCP} and a positive $\nabla^2\rho_{\text{BCP}}$ are representative of a closed-shell interaction (such as in dative and hydrogen bonds, van der Waals complexes). The network of all bond paths for a chemical system is termed the molecular graph. In the molecular graphs, bond critical points are shown by small red spheres; ring critical points, indicating structural ring features, by small yellow spheres.

Atomic charges were determined using AIMAll and the natural bond orbital (NBO)^{79,80} approach as implemented in Gaussian09. The NBO calculations were also used to validate the presence of π -bonding within the catalyst framework. Additional natural resonance theory (NRT)⁸¹⁻⁸⁴ evaluations were performed using NBO5.G^{80,85}. Only the first one or two major resonance contributors are given; resonance structures with smaller contributions exhibit cleaved single bonds and were not considered further.

4.3. Results and Discussion

4.3.1. CBS Catalyst

The C4 *S*-configured CBS catalyst framework consists of two fused five-membered rings (Fig. 4.1), a pyrrolidine and an oxazaborolidine with its O1–B2–N3 arrangement. The geometry of the unsubstituted CBS catalyst, with its relatively short B-N bond, has been described as a twisted chair¹³⁸, and little further insight is gained here on merely geometrical grounds^{117,137-139}.

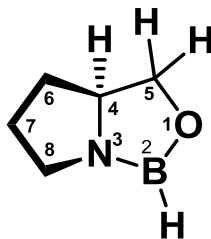


Figure 4.1: The unsubstituted CBS catalyst with ring atoms numbered.

According to an NBO analysis, and in agreement with the B=N formulation given earlier⁹⁵, as well as from an earlier NBO interpretation¹³⁸, the electron demand on boron with its formal electron sextet is satisfied by the lone pair of electrons on the adjacent nitrogen atom. This causes a substantial shortening of the N-B bond (142.9 pm from B3LYP/6-31+G(2d,2p)) from the calculated single-bond value of 149.2 pm (see Table 4.1 for this bond in the CBS-BH₃ adduct, which is in agreement with the standard single-bond length of approximately 150 pm⁹⁴) and the appearance of a double bond reminiscent of that in borazine (distance in the crystal structure¹⁴⁴ and calculated from B3LYP/6-31+G(2d,2p) is 142.9 pm). The N3 lone pair contributes 87.8% to the electron occupancy of the π -bond, which again is comparable to the NBO finding for borazine (88.7%; see S3 and S4 of Appendix B). The finding (HF/6-31G(d)) of a ‘much shortened’ B-O bond¹³⁸, though, is not reproduced from the here employed, larger model chemistry. The B-O bond length (137.6 pm from B3LYP/6-31+G(2d,2p)) is in full agreement with the standard single-bond length of 137 pm⁹⁴. In accordance, from an NRT analysis, the B=N resonance with 73.6% vastly dominates the electronic structure of the CBS catalyst, with an additional mere 8.9% for the B=O description. The electron densities at the B-N and B-O bond critical points are discussed in the context of borane complexation (Section 4.3.2).

Contrary to an earlier claim that the positive (NBO) charge on B2 of CBS leads to an easy complexation of the ketone oxygen atom¹³⁸, the blocking of the formal vacancy on B2 by the N3 lone pair should prevent the formation of a CBS-ketone adduct. This is indeed in agreement with

the fact that experimentally, for the diphenyl-substituted oxazaborolidine, enantiomeric excesses as high as 92% are observed in the reduction of *t*-butyl methyl ketone when the reducing BH₃ is added slowly to a CBS-ketone mix⁹⁵, presumably because a CBS-ketone adduct is not achieved in the absence of BH₃ (and because the CBS-uncatalyzed reaction is slow⁹⁵). In corroboration, and in analogy to the lack of a minimum along the B...O approach path between acetone and an unsubstituted and unfused oxazaborolidine¹³⁶, a CBS-ketone adduct with B...O interaction was not obtained with the model chemistries chosen here.

It is the proximity of N3 with its π -electron donation capability that interferes with the formation of such a CBS-ketone adduct. As demonstrated, the N3 lone pair of electrons fill the empty 2p_z orbital and thus satisfy the electron demand on boron.

4.3.2. Catalyst-borane adducts

According to ¹¹B NMR spectroscopic results, the introduction of BH₃ to the CBS catalyst leads to N3-BH₃ adduct formation⁹⁵. Representations of the optimized catalyst-borane adduct are shown in Fig. 4.2 as molecular graphs, and selected geometric parameters are given in Table 4.1. Complexation (free) energies are listed in Table 4.2.

Table 4.1: Selected geometric parameters (distances in pm, angles in °) of catalyst-borane adducts^a from various model chemistries.

	B3LYP^b		PBE0^b		ωB97X-D^b		MP2^c	
	CBS-BH₃	CBS-dBH₃	CBS-dBH₃	CBS-BH₃	CBS-dBH₃	CBS-BH₃	CBS-dBH₃	
O1-B2	134.5	139.8	140.0	134.3	140.0	135.0	141.0	
B2-N3	149.2	154.9	155.0	149.0	154.5	149.5	155.5	
N3-B_{BH3}	166.0	157.1	155.9	164.6	156.0	165.3	156.3	
O1-B2-N3	112.0	108.1	108.0	111.8	107.8	111.8	107.8	
B2-N3-B_{BH3}	101.8	79.2	77.7	101.7	78.6	102.3	78.2	
O1-B2-N3-B_{BH3}	105.8	114.1	114.0	105.3	114.2	103.7	114.6	
H-B2-N3-B_{BH3}	-77.3	-101.6	-103.3	-78.0	-102.7	-78.9	-103.1	

^a See Fig. 4.2 for structures. ^b 6-31+G(2d,2p) basis set. ^c 6-311++G(2d,p) basis set.

Table 4.2: Relative^a electronic and Gibbs free energies (kcal·mol⁻¹) of catalyst-borane adducts.^b

	B3LYP ^c		PBE0 ^c		ωB97X-D ^c		MP2 ^d	
	ΔE	ΔG	ΔE	ΔG	ΔE	ΔG	ΔE	ΔG
CBS-BH₃	-22.6	-8.2	N/A	N/A	-29.1	-14.5	-31.0	-17.0
CBS-dBH₃	-24.8	-9.2	-35.4	-19.8	-33.0	-17.4	-34.4	-18.9

^a With respect to the free reactants. ^b See Fig. 4.2 for structures. ^c 6-31+G(2d,2p) basis set. ^d 6-311++G(2d,p) basis set.

Figure 4.2 shows that the complexation of the CBS catalyst with BH₃ leads to two arrangements, the more flexible ‘dangling’ conformation (CBS-BH₃) and the lower-energy (by 2.2 kcal·mol⁻¹ in electronic energy, Table 4.2) conformation of diborane-like character (CBS-dBH₃) with its bridging hydrogen atom. In both cases, and in accord with previous work on the substituted^{40,137} and the unsubstituted¹³⁹ catalyst, the adducts form by borane binding with N3 on the oxazaborolidine nitrogen’s α-face (i.e., ‘under’ the catalyst). As the B-N-B angle increases on going from CBS-dBH₃ to CBS-BH₃, there are two further distinct geometrical changes: B2 re-hybridizes causing the N-B-O-H moiety to become nearly planar (177.6°), and the pyrrolidine ring undergoes a small conformational change.

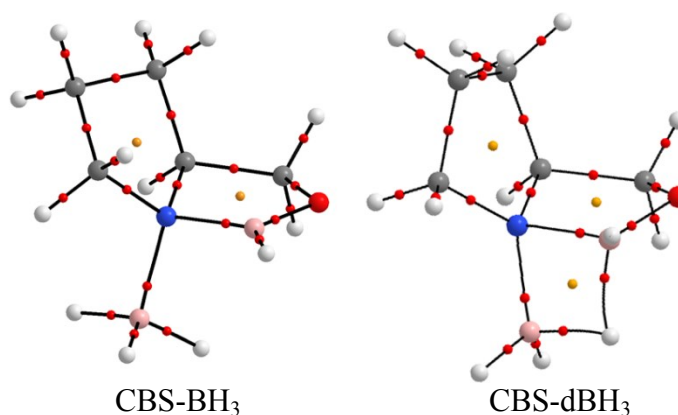


Figure 4.2: Molecular graphs of catalyst-borane adducts, showing non-diborane-like character (CBS-BH₃) and diborane-like character (CBS-dBH₃), from B3LYP/6-31+G(2d,2p). Atoms are represented by large spheres: carbon (grey), hydrogen (white), oxygen (red), nitrogen (blue) and boron (pink). Bond critical points are indicated by small red spheres, ring critical points by small yellow spheres.

While both minima are located with B3LYP (Fig. 4.2) and ω B97X-D, as well as MP2, only the diborane-like CBS-dBH₃ adduct is found with PBE0. In previous work, curiously, and based on an assessment of the out-of-plane distortion on boron B2, only the ‘dangling’ BH₃ adduct was reported from Hartree-Fock theory for the unsubstituted and unfused oxazaborolidine¹³⁶, as well as for the unsubstituted but pyrrolidine-fused CBS¹³⁸ (the “CBS-BH₃” of this work); the diborane-like adduct was located with B3LYP and MP2 only once polarization functions on heavy atoms were introduced into the basis set¹³⁶. The presence of both species in equilibrium has not been reported.

As the absence of CBS-BH₃ with PBE0 was puzzling, a series of relaxed scans were performed by increasing the B2-N3-B_{BH3} bond angle starting from CBS-dBH₃ (Fig. 4.3). The energy increases with the bond angle, revealing the relative amount of energy required to break the bond between the bridging hydride and B2 in the catalyst framework. The reaction coordinates for B3LYP (solid line) and ω B97X-D (dotted line) develop a plateau or saddle point (at 2.1 and 4.0 kcal·mol⁻¹, respectively), and at around 102° this corresponds in energy to that of the respective optimized CBS-BH₃ minimum (indicated by an ✕). A relaxed scan using MP2/6-311++G(2d,p) shows a pronounced minimum in this region (Fig. 4.3), supporting the B3LYP and ω B97X-D results. For further support, these two functionals were also tested using the larger 6-311++G(2d,p) basis set, with fundamentally no different results (S5 of the supplementary information). In contrast, with PBE0, bond angle opening results in a steeper rise of the energy with the absence of a minimum around 102° (Fig. 4.3). With an increase in the size of the basis set from double zeta (6-31+G(2d,2p)) to triple zeta (6-311++G(2d,2p)), the same curve is observed (S5 of the supplementary material). Even by forcing the pyrrolidine ring to adopt a different conformation (half-chair instead of envelope, to prevent the observed conformational

changes), the results persists, and an offset curve with an adduct of slightly higher energy is produced (S5 in the supplementary information). From these scans, it would seem that PBE0 treats the bridging hydrogen as much more effective in satisfying the electron demand on B2 than is the case for the other two functionals and MP2.

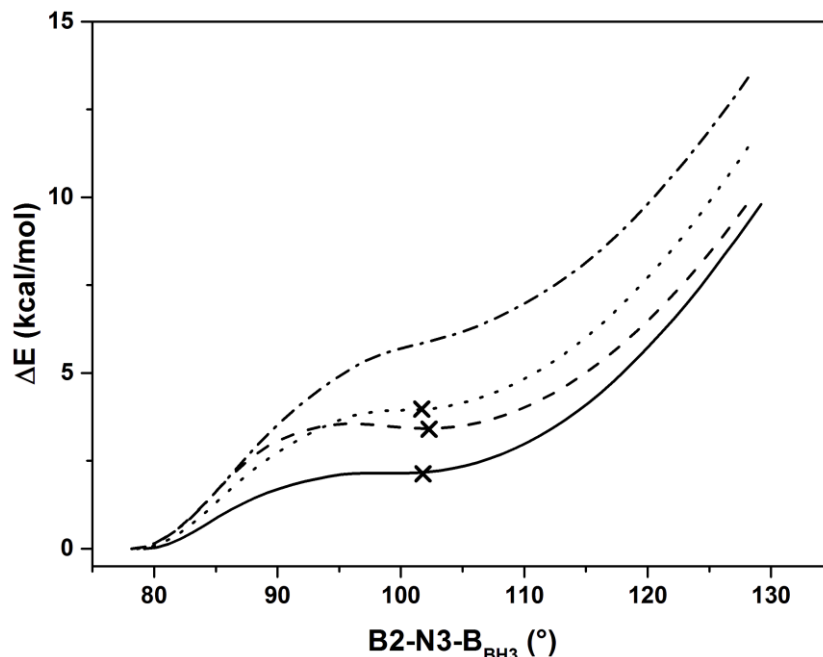


Figure 4.3: Energy profiles (relaxed scans, in $\text{kcal}\cdot\text{mol}^{-1}$) for the B-N-B angle change in the catalyst-borane adducts. B3LYP/6-31+G(2d,2p) (solid line), MP2/6-311++G(2d,p) (dashed line), ω B97X-D/6-31+G(2d,2p) (dotted line) and PBE0/6-31+G(2d,2p) (dash-dotted line). The three \times points represent the optimized CBS-BH₃ minima calculated with the respective model chemistries. The energies of the CBS-dBH₃ complexes from each functional are set to relative zero; the B-N-B bond angle was increased by one-degree increments.

Interestingly, the crystal structures of the substituted (diphenyl substitution on the oxazaborolidine ring and B-CH₃ substituent) catalyst-borane adduct only show the dangling CBS-BH₃ conformation^{145,146}. The relative free energies of the CBS-BH₃ and CBS-dBH₃ of the substituted catalyst, using B3LYP/6-31+G(2d,2p), are approximately $1.4 \text{ kcal}\cdot\text{mol}^{-1}$ in favour of the diborane-like character, i.e., similar to the situation in the unsubstituted catalyst. An

alignment of the CBS-BH₃ crystal structures with the B3LYP/6-31+G(2d,2p) optimized geometry is shown in Fig. 4.4. The CBS framework overlay, excluding hydrogen positions and substituents, shows a low RMS value of 0.082 Å, indicating that B3LYP is able to reproduce the geometries of these complexes with a high degree of accuracy. Crystal structures showing the diborane-like character have apparently not been reported. Based on the Boltzmann distribution and using the free energies obtained from B3LYP/6-31+G(2d,2p), in a room temperature equilibrium of CBS-dBH₃ and CBS-BH₃, the population ratio is 85:15 (91:9 for the substituted catalyst). Why, then, only the less stable CHS-BH₃ arrangement is found in the crystal remains unknown.

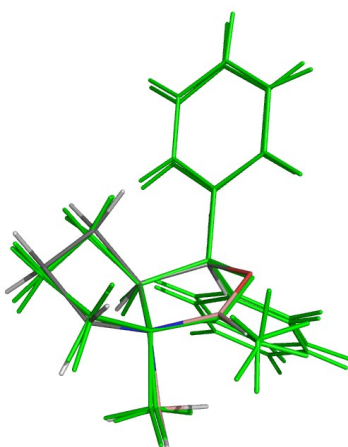


Figure 4.4: Alignment of the substituted CBS-BH₃ geometry observed in the crystal^{145,146} (green) with that of the optimized unsubstituted CBS-BH₃ from B3LYP/6-31+G(2d,2p) (coloured by element).

It is instructive to analyze the electronic structures of the two complexes from Fig. 4.2 as compared to that of the catalytic framework itself. From an NBO perspective, and in analogy to the B₂=N description for CBS, CBS-BH₃ shows a B₂=O description, which could, in principle, thwart ketone complexation. In CBS, though, an NRT analysis reveals that both N₃ and O₁ electron lone pairs donate to the deficient B₂ atom, with a resonance structure description of 73.6% (B=N) and 8.9% (B=O), respectively (Fig. 4.5). Accordingly, less energetic importance

must be assigned to the B=O interaction, and this holds for “B=O” in the CBS-BH₃ adduct as well. Thus, while the B=O resonance with 76.8% dominates its electronic structure (Fig. 4.5), B··O complexation to the ketone is now possible (see Section 4.3.3.1), rendering CBS-BH₃ the reactive species. The relative importance of the “B=O” can also be seen from the NRT results for CBS-dBH₃. As in CBS itself, the B=O description with 2.5% is small, whereas the diborane-like character is described through three resonance structures totaling 71.4% (Fig. 4.5, and S6 of Appendix B).

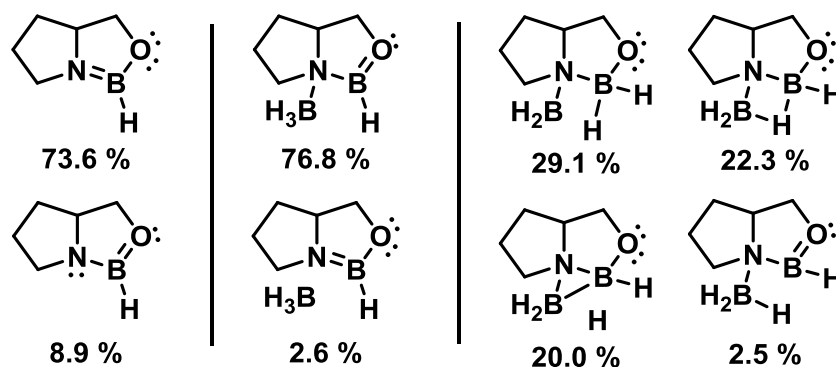


Figure 4.5: NRT structures of CBS (left), CBS-BH₃ (middle) and CBS-dBH₃ (right) with their associated resonance weights in percent. For simplicity, only the lone pairs are represented and the formal charges have been omitted. (From B3LYP/6-31+G(2d,2p).)

Table 4.3: Value of the electron density ($e \cdot \text{\AA}^{-3}$) at the bond critical point of N3-B2 and B2-O1 interactions of the catalyst and catalyst-borane adducts.^a Values in parentheses give the densities at the N3-B_{BH3} bond critical point.

	B3LYP ^b		PBE0 ^b		ω B97X-D ^b		MP2 ^c	
	N-B	B-O	N-B	B-O	N-B	B-O	N-B	B-O
CBS	1.438	1.390	1.437	1.399	1.439	1.403	1.391	1.346
CBS-BH₃	1.266 (0.698)	1.512	N/A	N/A	1.267 (0.754)	1.524	1.228 (0.726)	1.463
CBS-dBH₃	1.060 (0.952)	1.335	1.053 (0.978)	1.325	1.063 (0.974)	1.329	1.025 (0.951)	1.276

^a See Figs. 4.1 and 4.2 for structures. ^b 6-31+G(2d,2p) basis set. ^c 6-311++G(2d,p) basis set.

These changes in bonding are also reflected in the electron density (Table 4.3). The value of the electron density at the N3-B2 bond critical point decreases upon addition of BH₃ to N3. Without the N3 lone pair available, those on O1 donate to the empty 2p_z orbital on B2 and an increase in electron density at the O1-B2 bond critical point is observed for CBS-BH₃.

4.3.3. Pre-reaction complexes

4.3.3.1. B \cdots O complexation

Geometries:

In a systematic search, involving changes in dihedral angles, to locate pre-reaction complexes that would lead to the two enantiomeric products, catalyst-borane-ketone (CBK) complexes **1-6** with B \cdots O interactions were identified. Their optimized geometries are shown in Fig. 4.6 and selected geometric parameters are given in Table 4.4. Figure 4.7 gives an overlay of **1-6** that illustrates the B \cdots O complexation landscape.

As expected, ketone complexation to the catalytic framework affects the carbonyl bond length, and the shortest C=O bond is found in the loosest (as given by its complexation distance B2-O_{C=O}) complex, **6**; the longest C=O bond in the tightest complex, **5**. In fact, this B \cdots O_{C=O} distance varies distinctly between 156.8 and 173.1 pm (Table 4.4), and, in line with the long-distance cut-off in the visualization program, Fig. 4.6 only shows the B \cdots O interaction for complex **5**, the complex with the shortest distance in the set (Table 4.4). The values for the remaining distances and bond angles in Table 4.4 change less noticeably as they involve the rather rigid oxazaborolidine ring.

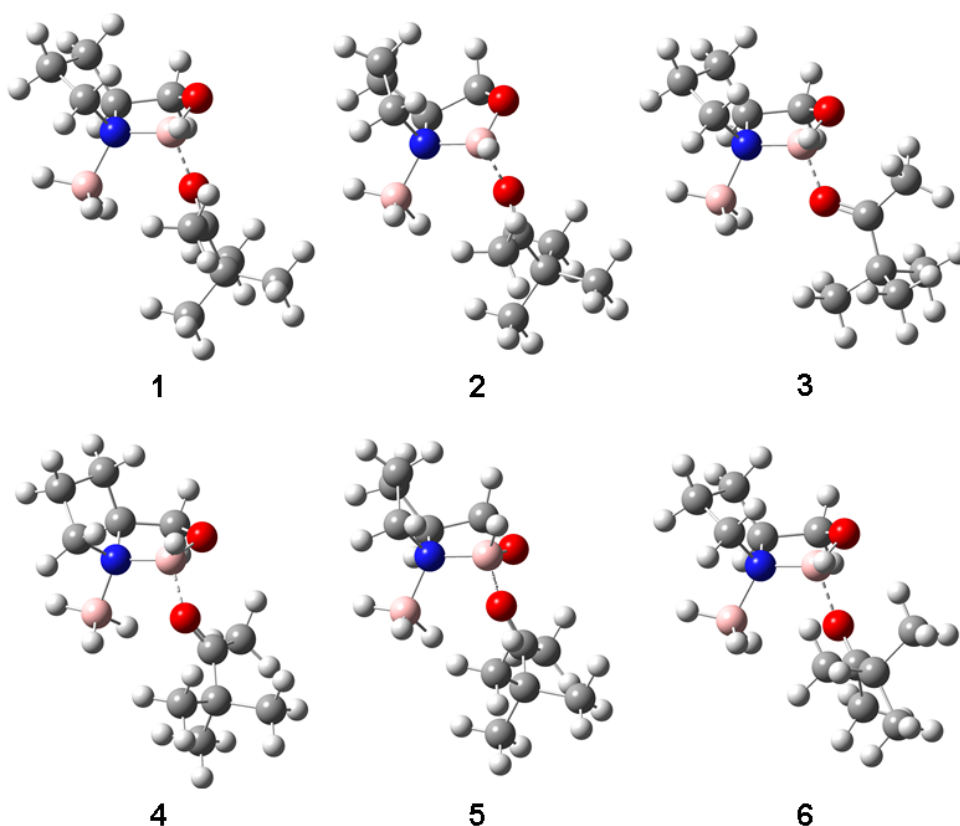


Figure 4.6: Representations of B \cdots O CBK complexes **1-6**, from B3LYP/6-31+G(2d,2p). The dashed lines (added using Gaussview software⁹³) indicate the carbonyl oxygen interaction with the catalyst framework.

Table 4.4: Selected geometric parameters (distances in pm, angles in $^{\circ}$) of B \cdots O CBK complexes **1-6**, from B3LYP/6-31+G(2d,2p).

	1	2	3	4	5	6
O1-B2	140.6	140.3	141.7	141.5	142.6	139.6
B2-N3	157.3	156.6	156.3	158.4	159.0	156.1
N3-B_{BH3}	163.1	162.8	164.0	163.8	163.1	164.1
B2-O_{C=O}	165.7	166.7	165.2	163.6	156.8	173.1
O_{C=O}-C_{C=O}	123.7	123.8	123.8	123.7	124.2	123.1
O1-B2-N3	107.0	106.7	107.3	107.3	105.7	108.0
B2-N3-B_{BH3}	117.7	118.8	117.1	115.5	114.9	118.1
O1-B2-N3-B_{BH3}	134.7	150.7	128.5	102.0	98.1	132.3
H-B2-N3-B_{BH3}	-93.6	-77.0	-99.6	-127.6	-133.7	-92.3
H-B2-O_{C=O}-C_{C=O}	20.9	25.4	-57.9	-133.5	-138.7	1.8
B2-O_{C=O}-C_{C=O}-C_{tBu}	-179.0	-178.0	177.8	177.7	-175.7	-5.3

In contrast, large ranges are observed for the various torsion angles, and those for the ketone orientation, $\text{H-B2-O}_{\text{C=O}}\text{-C}_{\text{C=O}}$ and $\text{B2-O}_{\text{C=O}}\text{-C}_{\text{C=O}}\text{-C}_{\text{tBu}}$, are most important considering the experimentally observed outcome of the reduction. Thus, in complexes **1** and **2**, the ketone presents its carbonyl *Si*-face to the catalytic hydride on the dangling BH_3 , allowing for eventual formation of the observed R configuration in the product. In contrast, complexes **4**, **5** and **6** expose the *Re*-face of the carbonyl to the bound borane, eventually leading to the unobserved (or very minor) S-configured enantiomer⁴⁰. In complex **3**, a catalytic hydride would lie in the carbonyl plane of the ketone, rendering it unreactive. For the reduction to occur, a re-orientation within the complex is required: a counter-clockwise rotation about $\text{H-B2-O}_{\text{C=O}}\text{-C}_{\text{C=O}}$ leads to complexes **1** or **2**, a clockwise rotation to complexes **4**, **5** or **6**.

In order to illustrate the complexation landscape for $\text{B}\cdots\text{O}$ complexation, Fig. 4.7 shows a superposition of complexes **1-6**, with an RMS of 0.990 Å (determined from all atoms within the catalyst framework). The complexity observed in the ketone region is expected from the differences in torsion angles, but one further feature stands out. The fused pyrrolidine ring in complex **2**, though **2** presents a ketone orientation similar to that in **1** (Fig. 4.6), possesses a different conformation (C7 of the envelope pointed inwards); so does complex **5**. To highlight these differences further, the CBS- BH_3 component was extracted from complexes **1-6**, and all six fragments are presented together with the optimized CBS- BH_3 adduct in Fig. 4.8.

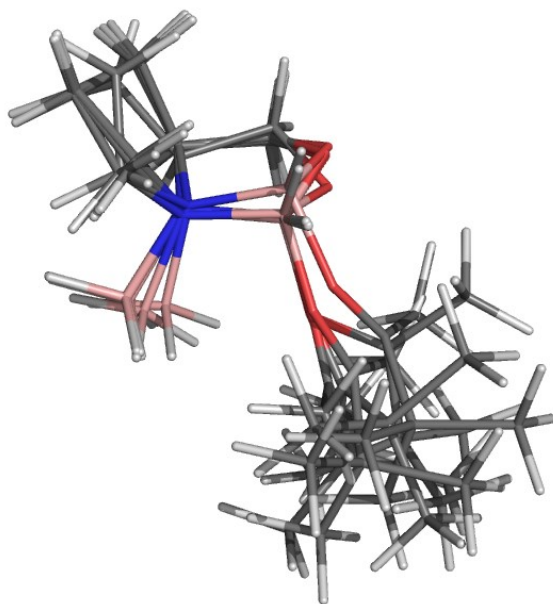


Figure 4.7: Alignment of the catalytic framework of B \cdots O CBK complexes **1-6**, from B3LYP/6-31+G(2d,2p), illustrating the B \cdots O complexation landscape.

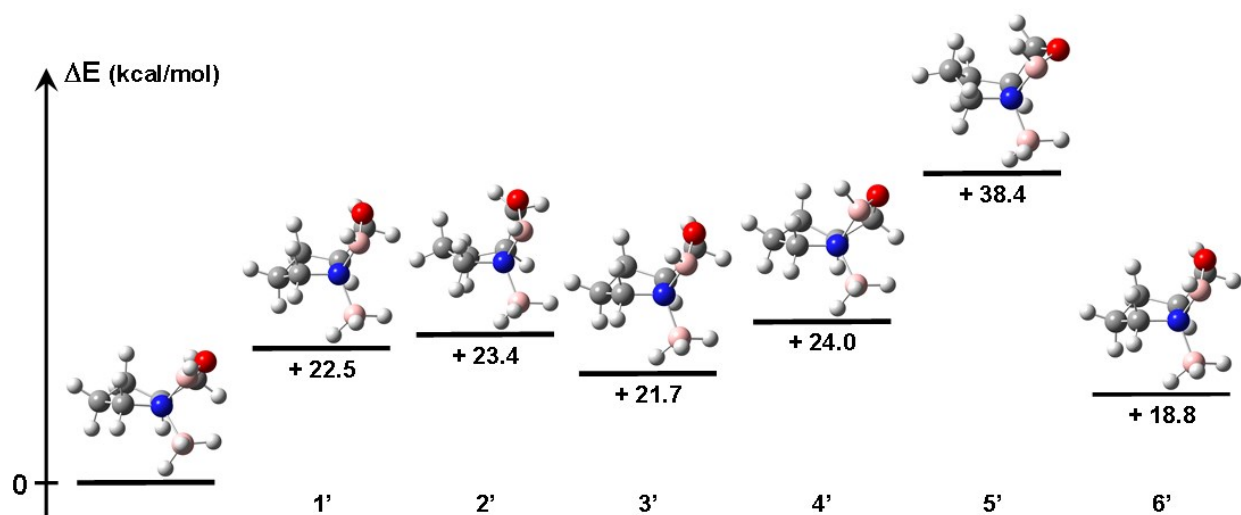


Figure 4.8: Relative energies (kcal·mol⁻¹) for various “conformations” of the CBS-BH₃ adduct, with that of the optimized B3LYP/6-31+G(2d,2p) geometry set to relative zero. A higher-energy conformation, identified with a prime on the number of the original complex, is isolated from its respective CBK complex **1-6**, and its energy evaluated with the same model chemistry.

Energies:

The BSSE for B \cdots O complex **1** (S2 of the supplementary information) was determined to be minor, around 1 kcal·mol⁻¹ (depending on the basis set) for the treatment of CBS-BH₃ and *t*-

butyl methyl ketone as individual fragments, in agreement with previous work¹³⁶ on a closely related complex exhibiting negligible counterpoise correction. Therefore the relative energies reported here are uncorrected.

The relative (free) energies, reported with respect to the free reactants CBS and BH₃, for complexes **1-6** are given in Table 4.5. With respect to the order of the relative energies, that of the relative free energy values remains the same. The complexation is endergonic, with a substantial range of approximately 7 kcal·mol⁻¹ between **1** and **6**. In contrast, the process may be just exergonic when PBE0 and ωB97X-D results are considered, yet the range remains. Complexes **1** and **2**, whose major difference consists in the conformation of their pyrrolidine rings, are the most energetically favourable of the six B···O CBK complexes, which is a promising result with respect to the experimental outcome (R configuration) seeing that the *Si*-face is presented to the catalytic hydride.

Table 4.5: Relative^a electronic and Gibbs free energies (kcal·mol⁻¹) of pre-reaction complexes **1-6** with B···O interactions.

	B3LYP ^b		PBE0 ^b		ωB97X-D ^b	
	ΔE	ΔG	ΔE	ΔG	ΔE	ΔG
1	-22.3	6.6	-34.2	-4.9	-38.2	-7.5
2	-21.7	7.8	-33.7	-3.9	-37.8	-7.2
3	-20.1	9.2	-31.2	-2.5	-34.6	-4.3
4	-19.9	9.8	-31.8	-2.2	-36.0	-3.7
5	-19.2	10.8	-31.4	-1.5	-35.3	-3.1
6	-15.6	13.3	-27.0	2.7	-31.6	-0.4

^a With respect to the free reactants. ^b 6-31+G(2d,2p) basis set.

Whereas there is a relation between complexation distance (B2-O_{C=O}) and carbonyl bond length (Table 4.4), the complexation distance alone does not allow a ranking of the complexation energy (ΔE in Table 4.5), and the tightest complex **5** does not distinguish itself as being either

the most or the least stabilized. Given the geometrical changes from Table 4.4, this is hardly surprising. The lengthening of the carbonyl bond, for example, ranging from 1.5 to 2.6 pm, increases the energies of the complexes by 1.6 to 2.3 kcal·mol⁻¹, respectively (as determined from independent calculations on a C=O stretch in *t*-butyl methyl ketone).

More importantly, though, the tightness of the complexation also influences the hybridization on B2 from trigonal planar to tetrahedral, of which one measure is given in Table 4.4 (H-B2-N3-B_{BH3}). Thus, the different ketone orientations in complexes **1-6**, through their different B···O interactions, express different effects on the catalyst framework, and these can be evaluated energetically (Fig. 4.8). With the optimized CBS-BH₃ as relative zero, **4'**, which closely resembles the calculated CBS-BH₃ in structure, save for the change in hybridization of B2, has a deformation energy of 24 kcal·mol⁻¹. Accordingly, the deformation energy attributed to this particular degree of rehybridization of B2 would be approximately 24 kcal·mol⁻¹. Complexes **1**, **2**, **3** and **6** all have weaker complexation (Table 4.5) and therefore lower deformation energies (Fig. 4.8), with **6** being the weakest.

Complex **5** with the longest C=O bond length has the strongest complexation if judged by complexation distance (Table 4.4) and also possesses the largest deformation energy (Fig. 4.8), which is doubtlessly due in part to its higher degree of rehybridization. In addition, though, while **2'** and **5'** have like pyrrolidine geometries, the envelope in **5'** is more pronounced. Because the oxazaborolidine ring in **5'** is also in an envelope conformation (Fig. 4.8), its C5 methylene hydrogens find themselves in proximity to those on C7 in the pyrrolidine ring. The overall effect of these conformational changes results in complex **5**, while possessing the strongest complexation, not possessing the greatest complexation energy (Table 4.5).

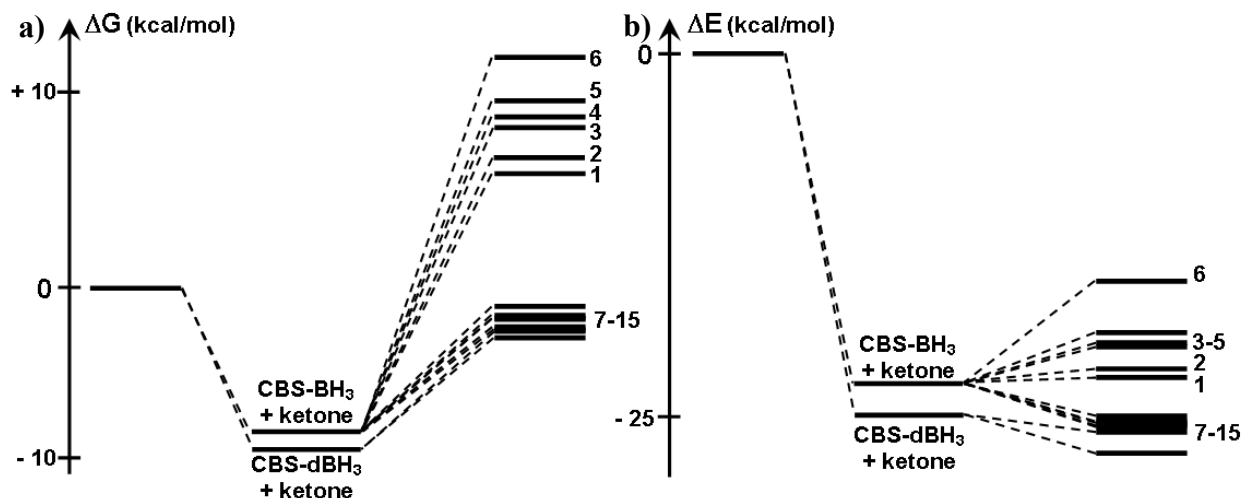


Figure 4.9: Complexation profiles for CBS-(d)BH₃ and subsequent CBK formation, with the reactants (ketone, CBS, BH₃) at relative zero, from B3LYP/6-31+G(2d,2p). Relative a) free energy and b) electronic energy (kcal·mol⁻¹).

Part of Figure 4.9 illustrates the relative complexation (free) energies for the B···O complexes **1-6** and the pronounced decrease in entropy that is associated with the tight binding of the ketone.

Electron densities:

The molecular graphs for complexes **1-6** showing all interactions are given in Fig. 4.10. All three model chemistries are in good agreement, and therefore the following discussion is presented for the B3LYP functional. Selected electron density values for complexes **1-6** are summarized in Table 4.6.

From Table 4.6, it can be seen that, even though complexes **1-6** derive from CBS-BH₃, in each case the electron density in the immediate environment of B2, i.e., O1-B2 and B2-N3, resembles more that in the tetracoordinate CBS-dBH₃ (Table 4.3). The entries also demonstrate that the electron density recovers the trends noted already in the geometries (Table 4.4). For example, complex **5**, which possesses the shortest complexation distance in the set, shows the

highest electron density value at the corresponding bond critical point ($B2-O_{C=O}$). The $B\cdots O$ interaction is of course the first and most obvious anchoring point for the ketone to the catalytic framework.

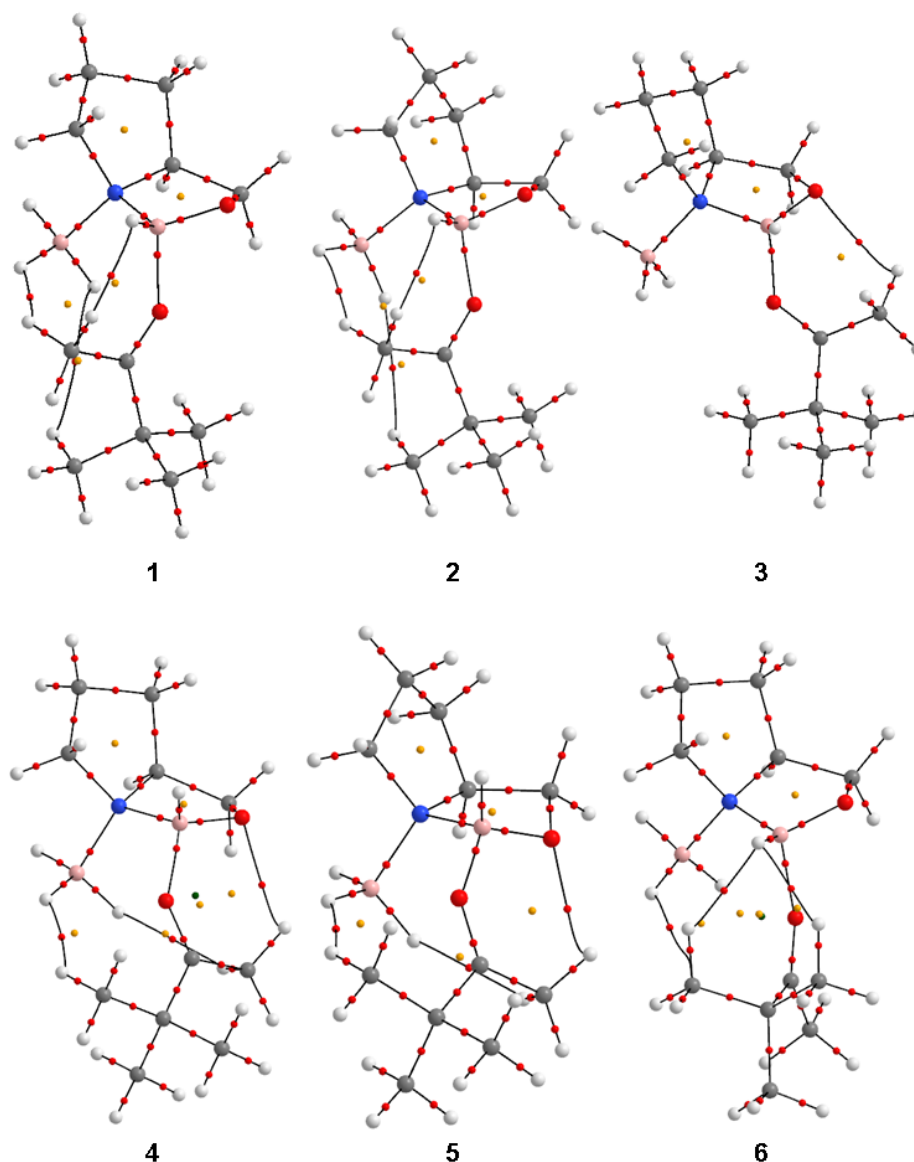


Figure 4.10: Molecular graphs of pre-reaction complexes **1-6** from B3LYP/6-31+G(2d,2p). Atoms are represented by large spheres: carbon (grey), hydrogen (white), oxygen (red), nitrogen (blue) and boron (pink). Bond critical points are indicated by small red spheres, ring critical points by small yellow spheres, cage critical points (indicating cage features) by small green spheres.

Table 4.6: Value of the electron density ($e \cdot \text{\AA}^{-3}$) at the bond critical point of selected interactions of B \cdots O CBK complexes **1-6**, from B3LYP/6-31+G(2d,2p).

	1	2	3	4	5	6
O1-B2	1.319	1.324	1.279	1.278	1.259	1.350
B2-N3	1.071	1.084	1.100	1.047	1.033	1.105
N3-B_{BH3}	0.819	0.834	0.792	0.804	0.820	0.792
B2-O_{C=O}	0.611	0.599	0.630	0.635	0.746	0.493
O_{C=O}-C_{C=O}	2.636	2.631	2.639	2.620	2.584	2.653

The second anchoring point for the ketone, which prevents its rotation within the complex, can be recovered from the electron densities or, more accurately, from the molecular graphs (Fig. 4.10). Anchoring the ketone in complexes **1** and **2** is an H \cdots H interaction between the partially negatively charged hydride on B2 of the catalytic framework and the partially positively charged protons of the methyl group on the ketone. While such interactions are often simply seen as “contact points” in crystallographic studies, QTAIM shows a path of maximum density of $0.071 e \cdot \text{\AA}^{-3}$ and $0.072 e \cdot \text{\AA}^{-3}$, for **1** and **2** respectively, between the two atoms and the presence of a bond critical point, and therefore a bonding interaction.

In analogy, complexes **4** and **5** contain a C_{methyl}-H \cdots O interaction ($0.103 e \cdot \text{\AA}^{-3}$ and $0.105 e \cdot \text{\AA}^{-3}$ for **4** and **5**, respectively) with the catalyst framework in addition to the B \cdots O interaction. While it is unclear of the effects this interaction has on the catalyst framework, it is important to not a large change in O1-B2-N3-B_{BH3}, for **4** and **5** compared to the other B \cdots O pre-reaction complexes (Table 4.4). In **6**, a *Re*-face attack will occur, but due to a significant difference in ketone orientation (Fig 4.10) the second anchoring points are two H \cdots H interactions ($0.065 e \cdot \text{\AA}^{-3}$ and $0.069 e \cdot \text{\AA}^{-3}$) and not a C-H \cdots O interaction.

To prevent the ketone to rotate freely in the catalytic complex, as this would lead to loss of enantioselectivity, it needs to be anchored through two interactions. In the B \cdots O complexes, the second anchoring point differs for the *Si*- and *Re*-face attacks. Whereas a ketone offering its *Si*-

face is anchored through an H \cdots H interaction that results in a twisted chair six-membered ring, a ketone offering its *Re*-face prefers a C-H \cdots O anchoring interaction to the catalyst framework that results in a boat-like six-membered ring.

4.3.3.2. C-H \cdots O complexation

Geometries:

The systematic search for B \cdots O complexation referred to in Section 4.3.3.1, involving changes in dihedral angles, also resulted in unexpectedly large movements of the ketone during the optimization that produced C-H \cdots O complexes **7-15**. The optimized geometries of these are shown in Fig. 4.11, and Fig. 4.12 gives an overlay of **7-15** that illustrates part of the C-H \cdots O complexation landscape. An extensive search to locate further complexes was not conducted.

Figure 4.12, in particular, illustrates two regions of complexation for the ketone, and because the reactive BH₃ is found “below” the chiral framework while the ketone in complexes **13-15** is found “above”, an intra-complex reaction is precluded. As reactions between complexes are not considered in this study, **13-15** are excluded from further analysis, and Table 4.7 presents selected geometric parameters for complexes **7-12** only.

The dashed lines in Fig. 4.11 identify the interactions between the carbonyl oxygen and the methylene hydrogens on the catalyst framework. These, in comparison to the B \cdots O interaction in **1-6**, weaker interactions in **7-12** do not induce large changes in the geometries of either their uncomplexed, constituent CBS-BH₃ or ketone. In particular, the large conformational changes observed in the CBS moiety upon B \cdots O complexation (Fig. 4.7) are absent for C-H \cdots O complexation (Fig. 4.12), and Table 4.7 is invariant in the C=O bond length (which is shortened from that in **1** and **2** by about 2 pm, Table 4.4).

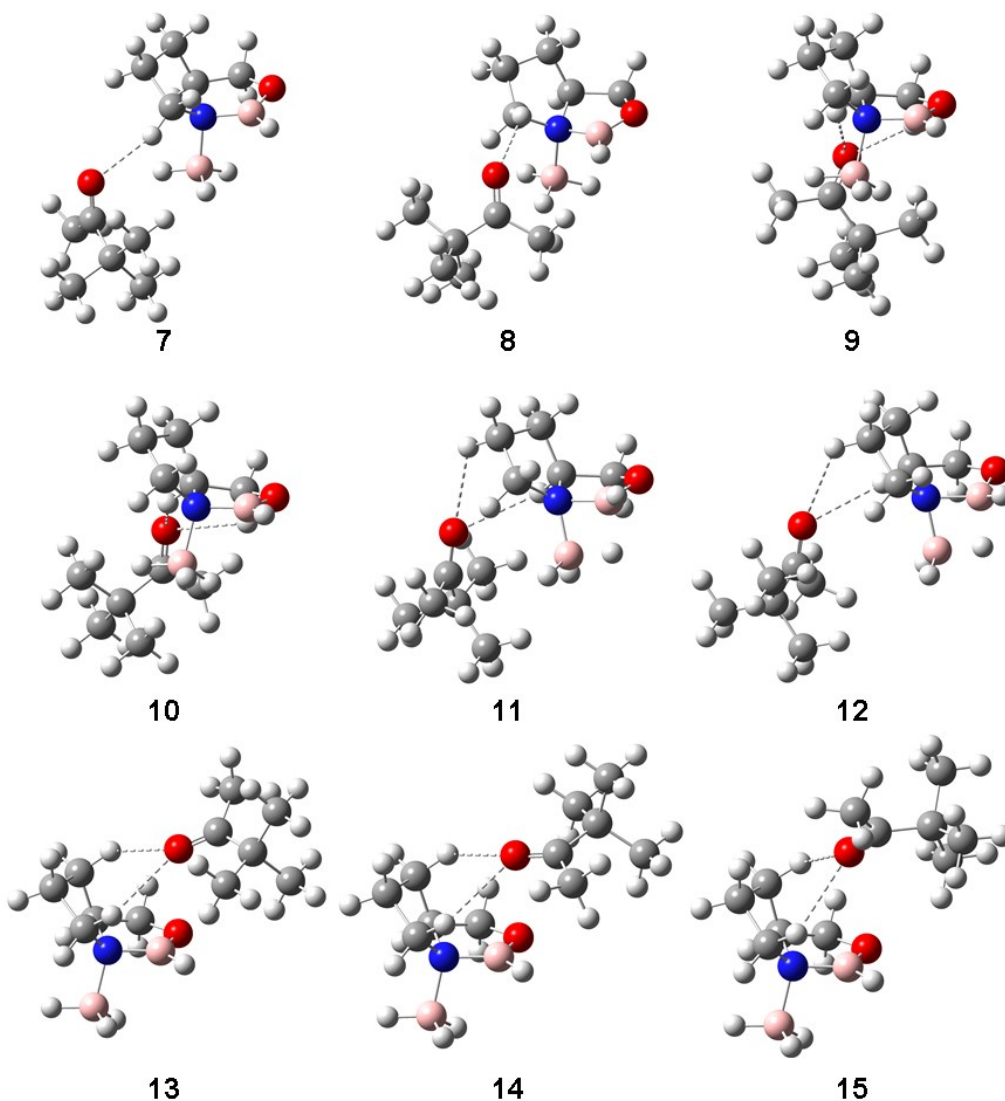


Figure 4.11: Representations of C-H \cdots O CBK complexes 7-15, from B3LYP/6-31+G(2d,2p). Bonds to the bridged hydrogen atom in **11** and **12** were not given in the Gaussview software and were not added manually. The dashed lines (added using Gaussview software⁹³) indicate the carbonyl oxygen interaction with the catalyst framework.

As can be seen from Fig. 4.11, complexes **11** and **12**, in contrast to **7-10**, possess the diborane-like character of CBS-dBH₃. Keeping in mind that, with B3LYP (and ω B97X-D and MP2) both CBS-BH₃ and CBS-dBH₃ were located, the fact that both types can be found for the larger CBK complexes is therefore not surprising. As noted with the catalyst-borane adducts

themselves (Section 4.3.2), CBS-BH₃ was not located by PBE0, and this is again reflected in the larger CBK complexes.

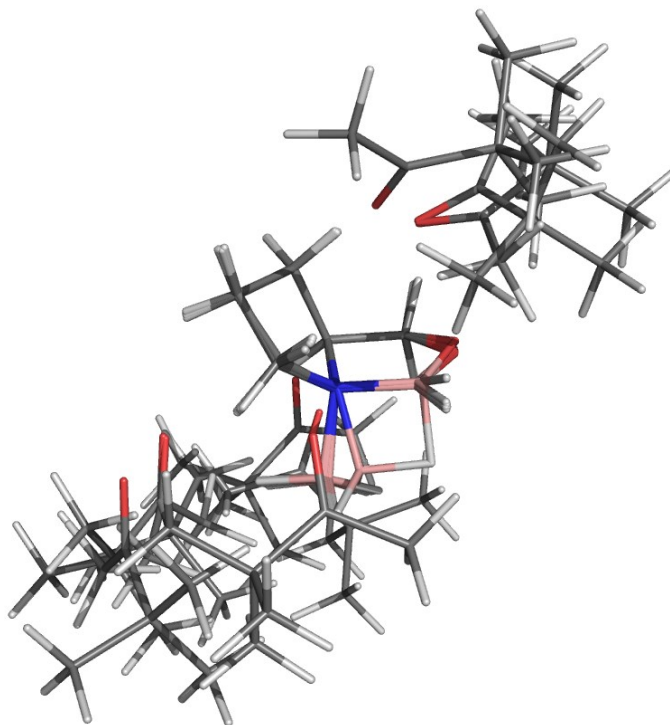


Figure 4.12: Alignment of the catalytic framework of C-H...O CBK complexes **7-15**, from B3LYP/6-31+G(2d,2p), illustrating part of the C-H...O complexation landscape.

Table 4.7: Selected geometric parameters (distances in pm, angles in °) of C-H...O CBK complexes **7-12**, from B3LYP/6-31+G(2d,2p).

	7	8	9	10	11	12
O1-B2	134.5	134.6	134.2	134.3	139.6	139.7
B2-N3	149.3	149.4	149.4	149.3	154.5	154.6
N3-B_{BH3}	165.3	165.5	165.3	165.4	157.3	157.2
O_{C=O}-C_{C=O}	121.6	121.6	121.7	121.6	121.6	121.6
O1-B2-N3	112.1	112.0	112.2	112.1	108.6	108.6
B2-N3-B_{BH3}	101.8	101.5	103.2	102.5	79.2	79.2
O1-B2-N3-B_{BH3}	105.7	104.9	106.7	106.0	113.1	113.1
H-B2-N3-B_{BH3}	-77.2	-77.5	-75.8	-76.7	-101.3	-101.5

Energies:

The BSSE correction was assessed for the C-H \cdots O complexes **10** and **12** and was determined to be even smaller (0.3 to 0.5 kcal \cdot mol $^{-1}$, respectively) than that for B \cdots O complexation (S2 of the supplementary information) and therefore negligible.

Table 4.8: Relative^a electronic and Gibbs free energies (kcal \cdot mol $^{-1}$) of pre-reaction complexes **7-15** with C-H \cdots O interactions.

	B3LYP ^b		PBE0 ^b		ω B97X-D ^b	
	ΔE	ΔG	ΔE	ΔG	ΔE	ΔG
7	-25.3	-1.0	-39.0	-13.8	-41.9	-13.3
8	-24.9	-1.5	-37.7	-13.0	-36.9	-10.0
9	-26.0	-2.4	-39.1	-13.4	-38.3	-10.5
10	-25.6	-2.4	– ^c	– ^c	-38.1	-11.9
11	-27.5	-2.8	-39.1	-13.4	-42.2	-12.4
12	-29.8	-2.6	-39.0	-13.8	-41.9	-13.3
13	-25.4	-1.7	-38.3	-13.3	-37.3	-9.0
14	-25.6	-1.7	-39.1	-12.8	-38.2	-10.5
15	-25.1	-2.2	-38.8	-12.8	-42.0	-13.5

^a With respect to the free reactants. ^b 6-31+G(2d,2p) basis set. ^c A minimum was not found.

The relative (free) energies for complexes **7-15** are given in Table 4.8. In contrast to Table 4.5 for **1-6**, and as a direct result from the lack of deformation upon complex formation, all complexation free energies are negative. As seen for **1-6** (Table 4.5), the degree of binding for **7-15** changes with the functional employed, yet the relative order remains the same. A comparison of the B3LYP values with those from Table 4.5 for complexes **1-6** reveals a smaller range of complexation energies. Whereas the electronic and free energies for **1-6** are spread over a range of 6.7 kcal \cdot mol $^{-1}$, **7-15** only span 4.9 kcal \cdot mol $^{-1}$ in electronic and 1.8 kcal \cdot mol $^{-1}$ in free energy. These numbers are shown graphically in Fig. 4.9 and agree well with the lack of change in geometry upon formation of **7-15** (or **7-12** as given in Table 4.7). Figure 4.9 also shows that

these C-H \cdots O complexes are lower in (free) energy than their B \cdots O counterparts, and the gap between the two sets is 7.6 kcal \cdot mol $^{-1}$ (free energy, Fig. 4.9a) or 2.6 kcal \cdot mol $^{-1}$ (electronic energy, Fig. 4.9b). Thus, the entropy contribution to the looser binding of the ketone in **7-15** is much less than that in the tighter bound B \cdots O complexes **1-6**.

Electron densities:

With only small changes to the catalyst framework geometry, changes in the electron density are expected to be small as well. The salient electron density values for complexes **7-12** are summarized in Table 4.9, and the molecular graphs of **7-15** are shown in Fig. 4.13. All three model chemistries are in good agreement, and therefore the following is presented for the B3LYP functional.

Table 4.9: Value ($e\cdot\text{\AA}^{-3}$) of the electron density at the bond critical point of selected interactions of C-H \cdots O CBK complexes **7-12**, from B3LYP/6-31+G(2d,2p).

	7	8	9	10	11	12
O1-B2	1.512	1.510	1.526	1.520	1.340	1.339
B2-N3	1.268	1.263	1.262	1.265	1.074	1.073
N3-B_{BH3}	0.750	0.746	0.751	0.747	0.954	0.955
O_{C=O}-C_{C=O}	2.812	2.814	2.808	2.811	2.812	2.813

Judged against complexes **1-6** (Table 4.6), Table 4.9 shows a substantial increase in electron density at the O1-B2 bond critical point for **7-10** with their tricoordinate B2 atom. This situation is similar to that in CBS-BH₃ (Fig. 4.2 and Table 4.3), and a B2=O1 resonance contribution can be expected in **7-10**. Complexes **11** and **12**, on the other hand, with their tetracoordinate B2, resemble CBS-dBH₃ and **1-6** in this respect. The remaining electron density values in Table 4.9

are unremarkable and reminiscent of the CBS-BH₃ and CBS-dBH₃ values as well. Clearly, the electronic influence of the ketones in the C-H···O complexes is minimal (Fig 4.13).

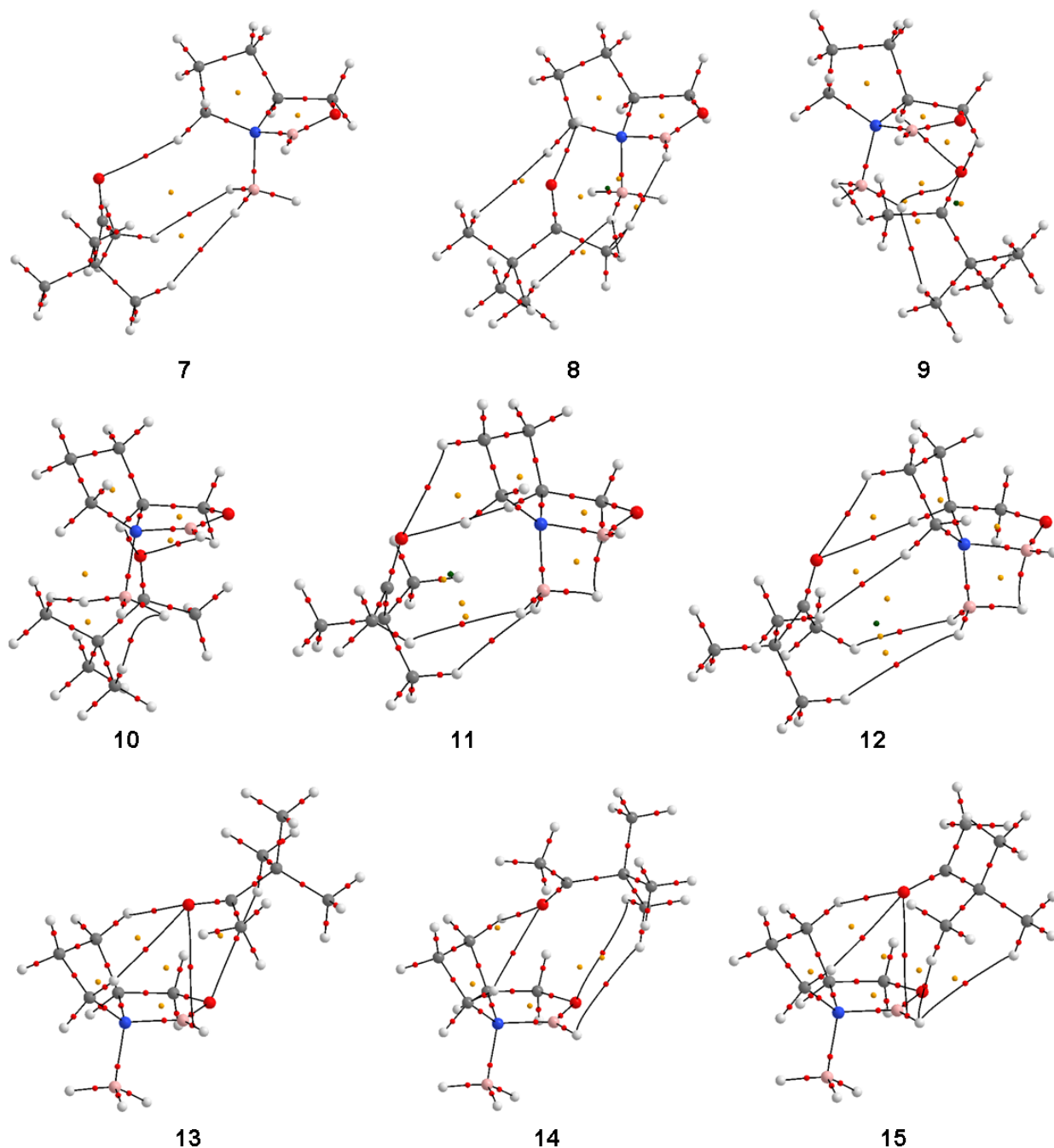


Figure 4.13: Molecular graphs of pre-reaction complexes **7-15** from B3LYP/6-31+G(2d,2p). Atoms are represented by large spheres: carbon (grey), hydrogen (white), oxygen (red), nitrogen (blue) and boron (pink). Bond critical points are indicated by small red spheres, ring critical points by small yellow spheres, cage critical points (indicating cage features) by small green spheres.

4.3.4. Reaction pathways (Transition States)

Based on experimental results, it has been established that the *Si*-face of the ketone should be the preferred face of attack in order to give the *R*-configured product in excess^{40,95}. As the reaction is catalyzed by the CBS framework and to put the required activation energies into perspective, the uncatalyzed reaction was studied first with the here-employed model chemistries. In the following, the uncatalyzed reaction up to its transition state will be presented, followed by the catalyzed reaction.

4.3.4.1. Uncatalyzed reaction

The optimized geometries for the un-catalyzed reaction (we chose *t*-butyl methyl ketone plus BH₃) are shown in Fig. 4.14, and total and free energies can be found in the supplementary material (S1). Each stationary point (pre-reaction complex, transition state, product) was optimized with all three functionals; the IRC calculation to validate the transition state connected to the correct pre-reaction complex and borinate product was only performed with B3LYP.

Due to the fact that both the ketone and BH₃ are achiral, product formation would be racemic, and only the transition state for the *Si*-face attack was calculated and is shown in Fig. 4.14. The IRC path for the un-catalyzed reaction shows a shoulder in both the forward and reverse path from the transition state. These shoulders are due to conformational changes: the borane is moving from within the carbonyl plane of the pre-reaction complex (given as ΔE relative zero) to being out-of-plane in the transition state and finally falling back into the former carbonyl plane in the borinate product. The calculated transition state free energy for the uncatalyzed reaction with respect to the reactants is 12.5 kcal·mol⁻¹ (B3LYP), 6.2 kcal·mol⁻¹ (PBE0) and 8.5 kcal·mol⁻¹ (ω B97X-D). The binding free energy of the pre-reaction complex

from the ketone and BH_3 is $32.4 \text{ kcal}\cdot\text{mol}^{-1}$ (B3LYP), $8.5 \text{ kcal}\cdot\text{mol}^{-1}$ (PBE0) and $6.4 \text{ kcal}\cdot\text{mol}^{-1}$ ($\omega\text{B97X-D}$), i.e., the complexation is exergonic. Thus, from the associated pre-reaction complex, the barrier (activation free energy) increases to $44.9 \text{ kcal}\cdot\text{mol}^{-1}$ (B3LYP), $14.7 \text{ kcal}\cdot\text{mol}^{-1}$ (PBE0) and $14.9 \text{ kcal}\cdot\text{mol}^{-1}$ ($\omega\text{B97X-D}$).

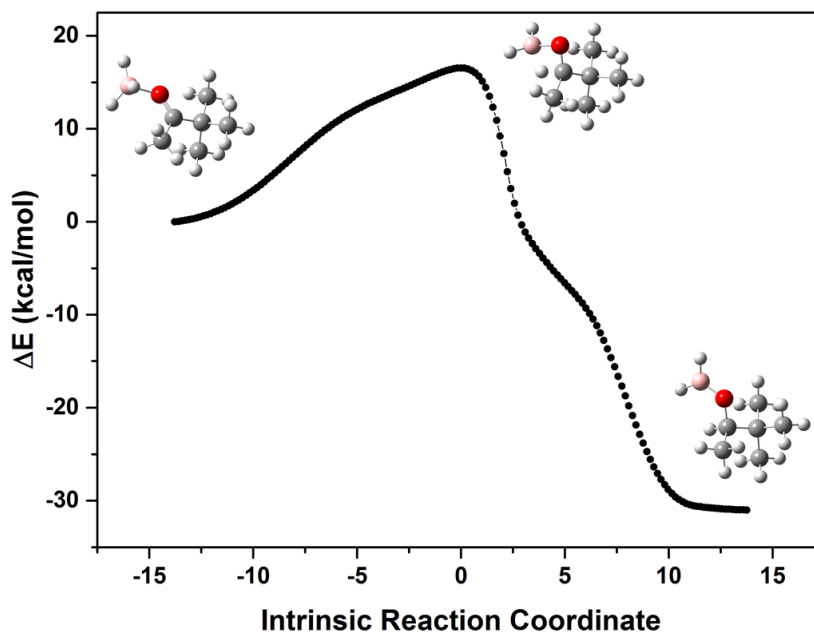


Figure 4.14: Intrinsic reaction coordinate for the uncatalyzed reduction of *t*-butyl methyl ketone by BH_3 , B3LYP/6-31+G(2d,2p). The points of inflection discussed (see text) are indicated with arrows.

Obviously, the activation free energies obtained vary with the functional, but even for the smaller barriers, at room temperature, the uncatalyzed reduction would be very slow. Even an unfused, achiral oxazaborolidine in which the framework-boron B2 is unsubstituted greatly increases the rate of reduction of acetophenone at room temperature⁹⁵.

4.3.4.2. Catalyzed reaction

The catalyzed reaction, to achieve enantioselectivity, requires the ketone, BH_3 and the chiral CBS framework. In Section 4.3.3, the various ways in which these three components can combine were presented, specifically, reaction can occur from $\text{B}\cdots\text{O}$ and from $\text{C-H}\cdots\text{O}$ complexes. In the following, reaction barriers (Table 4.10 and Fig. 4.15) are discussed and then the reactions are analyzed by type: Pathway 1 describes the reaction of a *Si*-face attack from $\text{B}\cdots\text{O}$ pre-reaction complexes **1** and **2**, through **TS1** (Fig. 4.16); Pathway 2 the reaction of a *Re*-face attack from $\text{B}\cdots\text{O}$ pre-reaction complexes **4**, **5** and **6**, through **TS2**, **TS3** and **TS4**, respectively (Fig. 4.17); and Pathway 3 the *Re*-face and *Si*-face attacks from two $\text{C-H}\cdots\text{O}$ pre-reaction complexes, **11** and **12**, through **TS5** and **TS6**, respectively (Fig. 4.18). **TS7**, which derives from $\text{B}\cdots\text{O}$ complex **3**, is related to the uncatalyzed reaction in that the $\text{C}=\text{O}\cdots\text{B}_2\text{-H}$ hydride is transferred, exhibits reaction barriers comparable to that of the uncatalyzed reaction, and is therefore only included in Table 4.10 but not analyzed further (the molecular graph is presented in S7 of Appendix B).

All three functionals are in qualitative agreement, and therefore more detailed results will be presented from the B3LYP functional.

The reactions barriers in Table 4.10 are presented with respect to the free reactants. Because BH_3 complexation to CBS is a highly exothermic event (more than $20 \text{ kcal}\cdot\text{mol}^{-1}$ from B3LYP, Table 4.2 and Fig. 4.9b), the activation energies presented for **TS1-TS4** are in fact (still) negative. The large entropy loss upon formation of complexes **1-6** (Fig. 4.9a and Fig. 4.15) leads to positive activation free energies from B3LYP. In accord with these transition states representing catalyzed reactions, the barrier on going from, e.g., pre-reaction complex **1** to **TS1** is only $2.8 \text{ kcal}\cdot\text{mol}^{-1}$ (B3LYP), compared to $44.9 \text{ kcal}\cdot\text{mol}^{-1}$ for the uncatalyzed reaction (i.e.,

lacking the CBS unit, Section 4.3.4.1). This, of course, is in part due to the lengthened, and therefore activated,¹⁴⁷ C=O bond of the ketone in complex **1** and the more favourable geometry for hydride transfer from the dangling BH₃. In the uncatalyzed reaction, as in **TS7** from complex **3**, hydride transfer involves an energetically unfavourable 4-membered ring transition state.

Table 4.10: Relative^a electronic and Gibbs free energies (kcal·mol⁻¹) of transition states **TS1-TS7**.

	B3LYP^b		PBE0^b		ωB97X-D^b	
	ΔE	ΔG	ΔE	ΔG	ΔE	ΔG
TS1	-19.4	11.7	-32.8	-1.8	-36.8	-4.5
TS2	-15.0	15.8	-28.6	2.3	-32.0	0.6
TS3	-16.3	14.8	-29.7	1.5	-32.8	-0.7
TS4	-13.5	17.8	-26.7	4.6	-31.0	2.0
TS5	29.6	58.4	17.4	46.4	13.8	43.5
TS6	29.8	58.7	17.7	46.7	14.0	44.7
TS7^c	6.5	35.9	-9.2	19.9	-11.5	18.7

^a With respect to the three reactants (CBS, BH₃, ketone). ^b 6-31+G(2d,2p) basis set. ^c The hydride of the catalytic framework (B2-H) is transferred.

Whereas Table 4.10, with entries **TS1-TS4** and **TS7**, considers all B···O complexes **1-6**, C-H···O complexes **7-12** are only represented through two transition states, **TS5** and **TS6**, from **11** and **12**, respectively. The carbonyl carbon in **7** and **8** is more than 400 pm distant from the reactive borane, precluding hydride transfer within the complex; **9** and **10** cannot exist for the experimentally employed C5-diphenyl-substituted CBS. All four were thus discarded. Even though the C-H···O pre-reaction complexes **11** and **12** are lower in energy than the B···O complexes **1-6**, their respective transition states are enormously higher in (free) energy, and Pathway 3 is implausible at room temperature. In Fig. 4.9a, the already substantial gap in free energy between the two sets of complexes appears relatively small in light of the gap between

the transition states ($6.1 \text{ kcal}\cdot\text{mol}^{-1}$ vs. $40.6 \text{ kcal}\cdot\text{mol}^{-1}$, respectively); the extremely large difference in activation free energies is currently not understood (Fig 4.15, see S8 and S9 of Appendix B results of all three functionals).

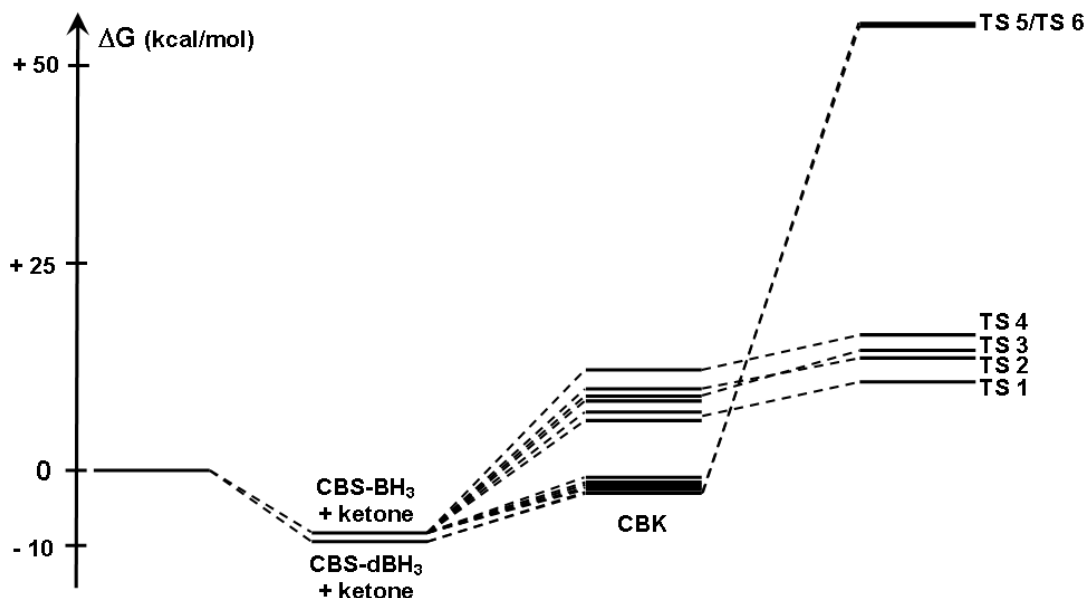


Figure 4.15: *t*-Butyl methyl ketone reduction reaction profile from reactants (ketone, CBS, BH₃) at relative zero to the rate limiting step: the hydride transfer transition state. Relative free energies ($\text{kcal}\cdot\text{mol}^{-1}$) with the three reactants at relative zero, from B3LYP/6-31+G(2d,2p).

The rate constants calculated from the free energy barriers are given in Table 4.11. Considered were, following Fig. 4.15, the largest possible barrier (that from CBS-BH₃ or CBS-dBH₃ plus the free ketone), given as k_1 , and the barrier from the free reactants (CBS, BH₃, ketone), given as k_2 . The relative rates clearly show that Pathway 1 is vastly favoured irrespective of whether k_1 or k_2 are chosen; it is this pathway that, through **TS1**, leads to the experimentally observed major enantiomer. Pathway 2 leads to the experimentally observed (very) minor enantiomer. The rates associated with **TS1** and any Pathway 2 transition state (**TS2**-**TS4**) produce a ratio (k_1/k_{p1} or k_2/k_{p1}) between 99 % and 100 % with all three functionals which

matches the experimental enantiomeric excess (97 %) of this reaction using the diphenyl substituted CBS catalyst.

Table 4.11: Calculated rate constants k (s^{-1}) and relative rates k/k_{P1} for the hydride transfer reaction, using the 6-31+G(2d,2p) basis set.

		B3LYP			
		k_1	k_1/k_{P1}^a	k_2^b	$k_2/\text{P1}^c$
Pathway 1	TS1	$1.58 \cdot 10^{-02d}$	1.00	$1.63 \cdot 10^{+04}$	1.00
Pathway 2	TS2	$1.56 \cdot 10^{-05d}$	0.00	$1.61 \cdot 10^{+01}$	0.00
	TS3	$8.42 \cdot 10^{-05d}$	0.01	$8.69 \cdot 10^{+01}$	0.01
	TS4	$5.31 \cdot 10^{-07d}$	0.00	$5.48 \cdot 10^{-01}$	0.00
Pathway 3	TS5	$1.65 \cdot 10^{-37e}$	0.00	$9.20 \cdot 10^{-31}$	0.00
	TS6	$9.93 \cdot 10^{-38e}$	0.00	$5.55 \cdot 10^{-31}$	0.00
		PBE0			
		k_1	k_1/k_{P1}^a	k_2^b	$k_2/\text{P1}^c$
Pathway 1	TS1	$3.91 \cdot 10^{-01e}$	1.00	$1.30 \cdot 10^{+14}$	1.00
Pathway 2	TS2	$1.49 \cdot 10^{-03e}$	0.00	$4.93 \cdot 10^{+11}$	0.00
	TS3	$7.11 \cdot 10^{-0.5e}$	0.00	$1.28 \cdot 10^{+11}$	0.00
	TS4	$9.37 \cdot 10^{-06e}$	0.00	$2.63 \cdot 10^{+09}$	0.00
Pathway 3	TS5	$2.08 \cdot 10^{-36e}$	0.00	$5.81 \cdot 10^{-22}$	0.00
	TS6	$1.25 \cdot 10^{-36e}$	0.00	$3.50 \cdot 10^{-22}$	0.00
		ωB97X-D			
		k_1	k_1/k_{P1}^a	k_2^b	$k_2/\text{P1}^c$
Pathway 1	TS1	$2.88 \cdot 10^{+05d}$	1.00	$1.24 \cdot 10^{+16}$	1.00
Pathway 2	TS2	$4.70 \cdot 10^{+02d}$	0.00	$2.02 \cdot 10^{+13}$	0.00
	TS3	$5.24 \cdot 10^{+01d}$	0.00	$2.25 \cdot 10^{+12}$	0.00
	TS4	$5.83 \cdot 10^{+00d}$	0.00	$2.12 \cdot 10^{+11}$	0.00
Pathway 3	TS5	$1.35 \cdot 10^{-32e}$	0.00	$7.78 \cdot 10^{-20}$	0.00
	TS6	$1.78 \cdot 10^{-33e}$	0.00	$1.03 \cdot 10^{-20}$	0.00

^a Relative rate referenced to that for Pathway 1. ^b Calculated from the reactants (sum of free energies for CBS, BH_3 , ketone). ^c Relative rate referenced to that for Pathway 1. ^d Calculated from the sum of free energies for the CBS- BH_3 complex and the ketone. ^e Calculated from the sum of free energies for the CBS-d BH_3 complex and the ketone.

4.3.4.2.1. Pathway 1. B···O complexation – *Si*-face attack

With the reactive BH₃ group “under” the CBS framework, in order for the *Si*-face attack on the ketone to occur, the ketone must approach the catalyst-borane adduct with the *t*-butyl group under the catalyst framework. For the transition state to be reached, the CBK complex tightens, bringing the sp² carbon closer to one of the BH₃ hydrides. This requires a rotation around the N3-B_{BH3} bond and is accompanied by a slight change in catalyst framework conformation.

Table 4.12: QTAIM oxygen charge (au) and electron density (e·Å⁻³) at the bond critical point of selected interactions of transition states **TS1-TS6**, from B3LYP/6-31+G(2d,2p).

	qO	O _{C=O} -C _{C=O}	B _{BH2} -H	C _{C=O} -H	H···H	C-H···O1
TS1	-1.244	2.532	0.986	0.253	0.078	
TS2	-1.263	2.477	0.976	0.275		0.122
TS3	-1.261	2.490	0.973	0.291		0.118
TS4	-1.246	2.525	0.993	0.234	0.093	
TS5	-1.200	2.216	0.410	1.423		
TS6	-1.198	2.218	0.413	1.421		

Figure 4.16 depicts this Pathway 1 for pre-reaction complexes **1** and **2**. The two complexes are rather similar in geometry (Table 4.4), with the main differences localized within the pyrrolidine ring, and it proved impossible to locate different transition states for each. Complex **2**, being slightly higher in energy (Table 4.5), exhibits the larger rate constant and was used for the Pathway 1 rates. As expected, in **TS1**, the molecular graph shows the hydride being transferred (Fig. 4.15), with interactions from the hydride to both boron and carbon atoms. As would be expected, formation of the transition state is also accompanied by a further decrease in electron density at the carbonyl bond critical point (Table 4.6 and Table 4.12 and an increase in charge, *q*, on the carbonyl oxygen (QTAIM qO: -1.196 au in **1** and -1.198 au in **2** to -1.244 au in **TS1**). This pathway depicts an early transition state, which is substantiated by the decrease in

B-H density and in the forming of the C-H bond (a fully formed methyl C-H bond of the secondary alcohol has a ρ value of $1.908 \text{ e} \cdot \text{\AA}^{-3}$ using B3LYP/6-31+G(2d,2p)) as well as the largely sp^2 character of the carbonyl carbon as given through the sum of the three bond angles on carbon, $\Sigma R-C-R$, without considering the newly forming C-H (357.2°). Importantly, while these changes occur as the reaction progresses, the transition state maintains the $H \cdots H$ interaction between methyl proton and B2 hydride already present in (**1** and **2**).

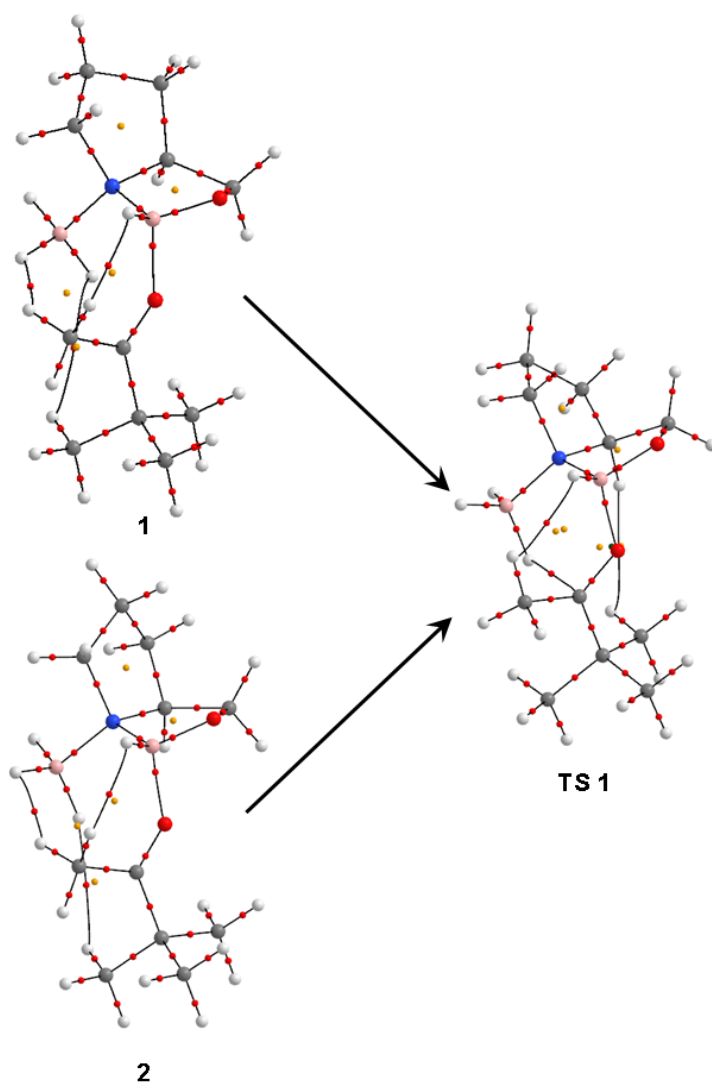


Figure 4.16: Molecular graphs for Pathway 1, leading to the experimentally observed enantiomer: pre-reaction complexes **1** and **2** and transition state **TS1**, from B3LYP/6-31+G(2d,2p). See text for the two conformations of the pre-reaction complex.

4.3.4.2.2. Pathway 2. B \cdots O complexation – *Re*-face attack

In order for the *Re*-face attack to occur, the ketone must approach the catalyst-borane adduct with the *t*-butyl group away from the catalyst framework, limiting steric interference from the bulky group. Overall, the changes observed in going from a pre-reaction complex to its transition state are similar to those for Pathway 1. Again the CBK complex tightens, bringing the sp² carbon closer to one of the BH₃ hydrides. A slight change in the conformation of the catalyst framework arises as well as a rotation about the N3-B_{BH3} bond.

Figure 4.17 depicts this Pathway 2 for pre-reaction complexes **4**, **5** and **6**. In contrast to Pathway 1, each complex is associated with its discrete transition state (**TS2**, **TS3** and **TS4**, respectively). Changes in geometry between **TS2** and **TS3** are largely restricted to the catalyst framework; **TS4** differs in that its ketone orientation follows that in **6** with its close-to-zero H-B2-O_{C=O}-C_{C=O} dihedral (Table 4.4), rather than the transoid conformation in **4** and **5**. The molecular graphs of the three transition states again display the hydride being transferred from BH₃ to the carbonyl carbon. Just like in Pathway 1, a decrease in the electron density at the carbonyl bond critical point and an increase in charge on its oxygen atom are observed (Table 4.12). These pathways also depict an early transition state which is substantiated by the decrease in B-H density (approximately 1.151 e \cdot Å⁻³ in pre-reaction complexes) and in the forming of the C-H bond. However, with a somewhat greater density decrease at the B-H bond critical point, the transition states of Pathway 2, **TS2**, **TS3**, and **TS4**, have progressed slightly further in the reaction than **TS1**. This can also be seen with a slightly further decrease in the sum of the three bond angles on carbon, Σ R-C-R, without considering the newly forming C-H (**TS2** 356.4°; **TS3** 356.1°; **TS4** 356.9°). Finally, as was found for **TS1**, **TS2** and **TS3** maintain the C_{methyl}-H \cdots O interaction (Table 4.12) with the catalyst framework already present in **4** and **5**, and **TS4**

maintains one of the two proton-hydride interactions from **6**. The *Re*-face attacks are slower than the *Si*-face attacks due to the greater displacement necessary to obtain the transition state. As previously mentioned (Section 4.3.4.2), **TS7** reduces the carbonyl by the creation of an unfavourable 4-membered ring. While it does undergo a *Re*-face attack, the reaction barrier is too high and so the H on the catalyst framework is an un-reactive hydride.

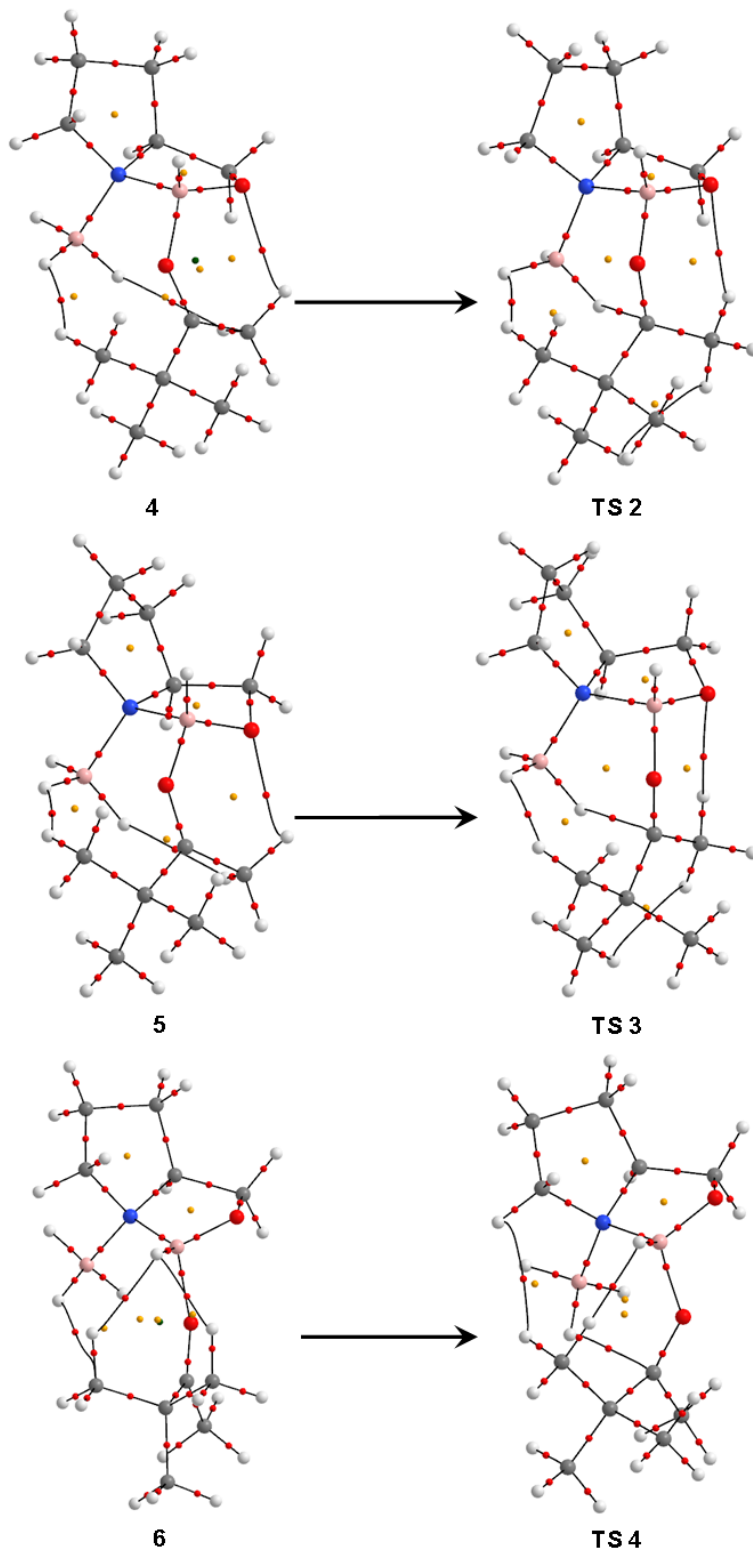


Figure 4.17: Molecular graphs for Pathway 2, leading to the experimentally unobserved enantiomer: pre-reaction complexes **4**, **5** and **6** and their respective transition states **TS2-TS4**, from B3LYP/6-31+G(2d,2p). Cage critical points, indicating structural cage features, are shown by small green spheres.

4.3.4.2.3. Pathway 3. C-H \cdots O complexation

For Pathway 3, C-H \cdots O pre-reaction complexes were evaluated, and both *Si*- and *Re*-face attacks were considered (Fig. 4.18), although with activation barriers greater than 60 kcal \cdot mol $^{-1}$ that translate into rate constants on the order of 10 $^{-33}$ s $^{-1}$, this pathway is unlikely to occur.

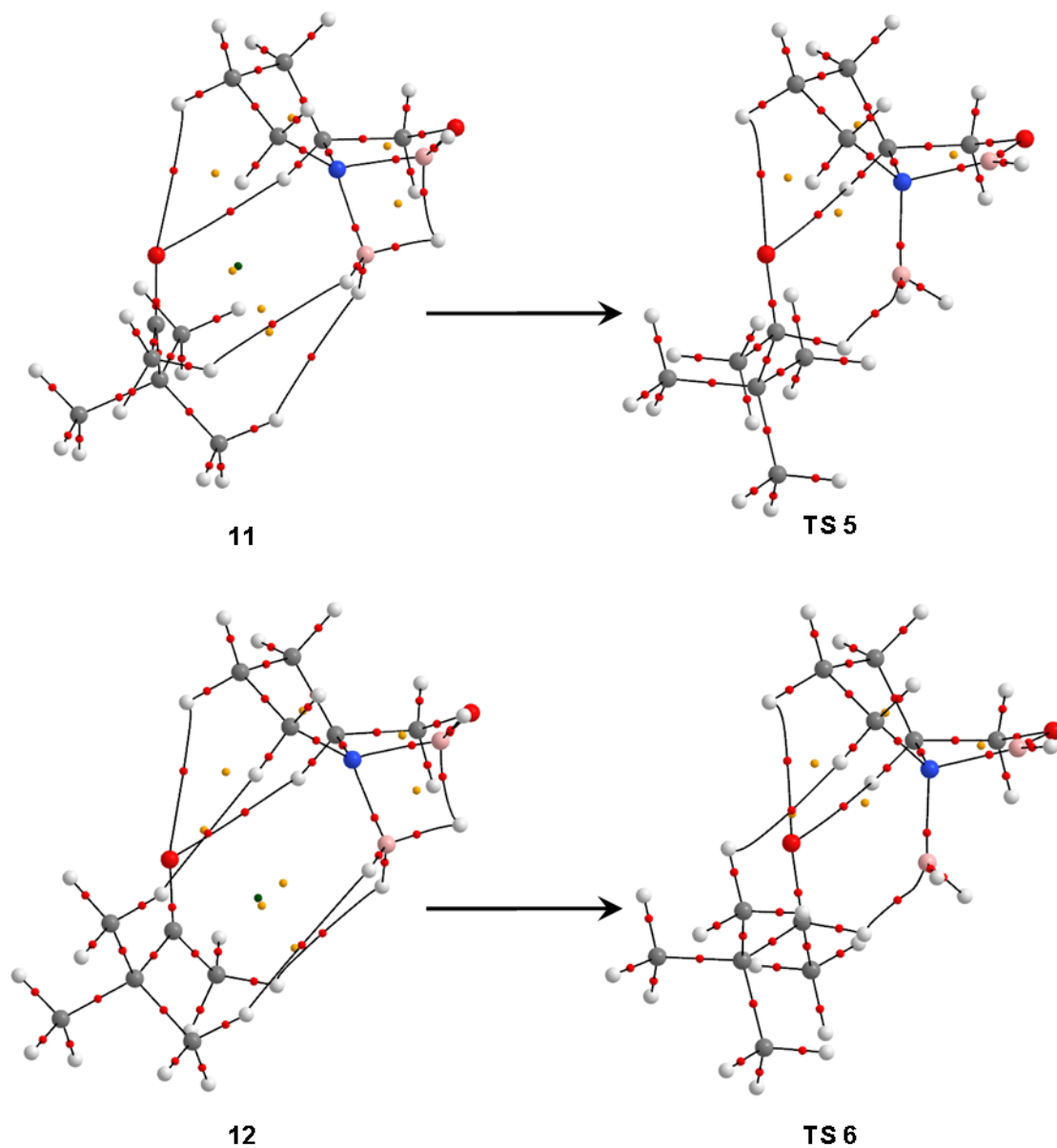


Figure 4.18: Molecular graphs for Pathway 3: pre-reaction complex 11 (12) and corresponding TS5 (TS6) (leading to the experimentally (un)observed enantiomer), from B3LYP/6-31+G(2d,2p).

In contrast with Pathways 1 and 2, and in agreement with the much larger activation energies in Pathway 3, **TS5** and **TS6** are late transition states in which the sp^2 -hybridized carbon of the ketone has more than halfway completed its re-hybridization into an sp^3 carbon with tetrahedral geometry as seen in the sum of the three bond angles on carbon, $\Sigma R-C-R$, without considering the newly forming C-H (**TS5** 341.4°; **TS6** 341.3°). The density at the B-H bond critical point has decreased substantially and the C-H bond is almost completely formed (Table 4.12). As expected, the complexation tightens as the borane breaks its diborane-like character and swings towards the ketone, increasing the B2-N3-B_{BH3} angle while rotating the N3-B_{BH3} bond for optimal hydride orientation. As the hydride shift nears completion, the negatively charged oxygen interacts with the now partially positive charged boron atom, forming a borinate intermediate. This simultaneous action produces a much larger imaginary frequency from those describing **TS1-TS4** where only the hydride is being transferred with minimal further motions, and is likely responsible for the very high activation energy (see S10 of Appendix B for **TS5** IRC).

4.4. Conclusions

In the reduction of *t*-butyl methyl ketone, using an unsubstituted, pyrrolidine-fused, *S*-configured oxazaborolidine catalyst with borane, the calculated enantiomeric excess by transition state theory lies in favour of the *R*-product. The excess is 99 % or greater, depending on whether the activation free energies are determined from B3LYP/6-31+G(2d,2p), PBE0/6-31+G(2d,2p) or ω B97X-D/6-31+G(2d,2p). This is nicely in accord with experimental observations where a substituted *S*-configured oxazaborolidine catalyst will produce the *R*-product through a *Si*-face attack onto the ketone. The catalytic effect was evaluated in comparison to the uncatalyzed

reaction of *t*-butyl methyl ketone with borane, and the higher activation barrier demonstrates that the chiral oxazaborolidine does act as a catalyst by decreasing the activation energy.

The unsubstituted catalyst proved to be much more flexible than originally anticipated causing deformation energies far greater than those contributed by any weak interaction in the pre-reaction complexes. Consequently, the source of enantioselectivity cannot be attributed to changes in anchoring interactions of the ketones within the catalytic system as the energy differences are dominated by the conformational changes of the catalyst framework.

In future work, with the addition of aromatic substitution on the catalyst as well as the use of acetophenone, the potential emergence of C-H \cdots π or π -stacking interactions would hopefully decrease the flexibility of the catalytic framework sufficiently to properly evaluate the weak interactions involved in the enantioselectivity of this reduction reaction.

Chapter 5.

Conclusions and future work

The incentive for carrying out this computational study was to determine the source of facial selectivity of the enantioselective reduction of prochiral ketones using a chiral oxazaborolidine catalyst with borane.

Previous experimental and computational work on this reaction served as a validation and complimentary reasoning to the new findings in this study. While the previous work was extensive, it failed to answer the fundamental question of the source of facial selectivity at the molecular level. Not much had been done in exploring borane-ketone complexation, however, previous studies involving aldehyde provided a basis of exploration and understanding on how to proceed further.

The first aspect of this work dealt with the complexation of substituted boranes to a prochiral ketone, acetophenone, in order to better understand the modes of complexation during the reduction reaction. It was confirmed that these complexes, with their general B \cdots O binding scheme, can adopt different conformations with further weak interactions, such as C $_{\alpha}$ -H \cdots F and C $_{\alpha}$ -H \cdots O.

A selection of π -electron donating along with non- π -electron donating groups exposed boron's electron deficiency. NBO and NRT calculations corroborate Lewis structures that attempt to satisfy the electron demand on B. Boranes substituted with π -electron donating groups fill the empty 2p $_z$ orbital through the presence of adjacent electron lone pairs. In contrast,

substituted boranes lacking these electron lone pairs supply electrons through hyperconjugation, but the stabilizing effect is necessarily smaller.

A ρ -on- $\nabla^2\rho$ approach was developed to estimate the electron density of the B $2p_z$ orbital using QTAIM, serving as a comparative to the NBO analysis. While values of the $\nabla^2\rho$ isosurface remained similar for the substituted boranes, the observed ρ -on- $\nabla^2\rho$ values pointed to clear differences between substituents that provide π -electron donation and those that do not. π -electron donating groups increased the density values of the B $2p_z$ orbital, but ρ -on- $\nabla^2\rho$ values for all boranes exceeded that of borane itself.

All substitution patterns studied here allow for the formation of gas-phase complexes. However, an increased electron demand on boron escalates the strength of the B \cdots O interaction and therefore binding energy. The quantification of a binding cut-off was determined by evaluating the relation between the binding energy and the estimated π -electron density for B $2p_z$. It was found that substituted boranes with ρ -on- $\nabla^2\rho$ less than $0.19 \text{ e}\cdot\text{\AA}^{-3}$ bind through a B \cdots O interaction with according boron re-hybridization, whereas those with values greater do not exhibit re-hybridization and only form van der Waals-type assemblies.

The second aspect of this work dealt with the enantioselective reduction of a prochiral ketone, *t*-butyl methyl ketone, using borane and a chiral oxazaborolidine catalytic framework, with the goal of elucidating the molecular source of the experimentally observed enantioselectivity. Even though experimental details for the particular unsubstituted oxazaborolidine employed in this study were not available, it was chosen here for computational efficiency.

In the reduction of *t*-butyl methyl ketone, using an S-configured oxazaborolidine catalyst and borane, the calculated enantiomeric excess by transition state theory lies in favour of the *R*-

product. The excess is 99.5 % or greater, depending on the activation free energies and the functional from which these were determined. This is nicely in accord with experimental observations where a substituted *S*-configured oxazaborolidine catalyst will produce the *R*-product through a *Si*-face attack onto the ketone.

The catalytic effect was evaluated in comparison to the uncatalyzed reaction of *t*-butyl methyl ketone with borane, and the higher activation barrier demonstrates that the chiral oxazaborolidine does act as a catalyst by decreasing the activation energy.

The unsubstituted catalyst proved to be much more flexible than originally anticipated, in that the oxazaborolidine and pyrrolidine rings change conformation depending on the orientation and mode of complexation of the ketone. The potential energy landscape is thus fairly pocketed. The free energy values for B \cdots O complexes show a much larger range and a distinct destabilization compared to those of the C-H \cdots O complexes. This effect is likely attributed to the larger conformational changes in the catalytic framework upon B \cdots O complexation and to entropic differences.

To prevent the ketone to rotate freely in the catalytic complex, as this would lead to loss of enantioselectivity, it needs to be anchored through two interactions. In the B \cdots O complexes, the second anchoring point differs for the *Si*- and *Re*-face attacks. Whereas a ketone offering its *Si*-face is anchored through an H \cdots H interaction that results in a twisted chair six-membered ring, a ketone offering its *Re*-face prefers a C-H \cdots O anchoring interaction to the catalyst framework that results in a boat-like six-membered ring.

In contrast to C-H \cdots O complexation, B \cdots O complexation activates the carbonyl group, which results in an energetically more favourable hydride shift. The C-H \cdots O complexes, while lower in

complexation energy, lead to transition states that are immensely high in energy and therefore preclude reaction.

Any change in the conformation of the catalytic framework upon B \cdots O complexation requires substantial energy, which nicely reduces the number of complexes in final consideration to two, one for *Si*- and one for *Re*-face attack, with the former energetically more stable. The activation free energies from either of these pre-reaction complexes are more or less the same, and thus the source for the enantioselectivity can be sought, in principle, in either differences in interactions in the two transition states or in the two pre-reaction complexes. Unfortunately, the energy differences are dominated by changes in conformation of the catalyst framework, rather than by changes in anchoring interactions of the ketones within the catalytic system.

Future work will focus on CBS catalysts as they are used in the reduction experiments. For example, diphenyl substitution on the oxazaborolidine ring and methyl substitution on its boron atom should be employed. While this increases the computational demand, it is also expected to increase the rigidity of the catalyst and to reduce the number of potential pre-reaction complexes, and therefore transition states for hydride transfer. Once aryl substitution on the catalyst is considered, the choice of ketone will also fall on aromatic rather than aliphatic substitution. With acetophenone as ketone, C-H \cdots π and π - π interactions can be expected, which may lead to additional complexes and which may be responsible for the enantioselectivity. Additionally, as the CBS reduction is performed in THF (and the results presented so far are gas phase calculations), it will be important to investigate solvation effects, through implicit or explicit inclusion of the solvent.

References

- (1) Eliel, E. L.; Mander, L. N.; Wilen, S. H. *Stereochemistry of organic compounds*; Wiley: New York, 1994.
- (2) Moss, G. P. *Pure Appl. Chem.* **1996**, *68*, 2193–2222.
- (3) Cahn, R. S.; Ingold, C.; Prelog, V. *Angew. Chem. Int. Ed. Engl.* **1966**, *5*, 385–415.
- (4) Bommel, A. J. van; Peerdeman, A. F.; Bijvoet, J. M. *Nature*, **1951**, *168*, 271–272.
- (5) Seebach, D.; Imwinkelried, R.; Weber, T. "EPC Syntheses with C, C Bond Formation via Acetals and Enamines", Scaffold, R. Ed. *Modern Synthetic Methods* **1986**, *4*, Springer, Berlin, 125–259.
- (6) Kagan, H. B.; Fiaud, J. C. *Top. Stereochem.* **1978**, *10*, 175–285.
- (7) Gladysz, J.; Michl, J. *Chem. Rev.* **1992**, *92*, 739–739.
- (8) Brown, H. C.; Zweifel, G. *J. Am. Chem. Soc.* **1959**, *81*, 247–247.
- (9) Schlesinger, H. I.; Brown, H. C.; Hoekstra, H. R.; Rapp, L. R. *J. Am. Chem. Soc.* **1953**, *75*, 199–204.
- (10) Brown, H. C. *Science* **1980**, *210*, 485–492.
- (11) Noyori, R.; Ohkuma, T.; Kitamura, M.; Takaya, H.; Sayo, N.; Kumobayashi, H.; Akutagawa, S. *J. Am. Chem. Soc.* **1987**, *109*, 5856–5858.
- (12) Ramachandran, P. V.; Brown, H. C. *Recent Advances in Asymmetric Reductions with B-Chlorodiisopinocampheylborane* 1996; pp. 84–97.
- (13) Mashima, K.; Kusano, K.; Sato, N.; Matsumura, Y.; Nozaki, K.; Kumobayashi, H.; Sayo, N.; Hori, Y.; Ishizaki, T. *J. Org. Chem.* **1994**, *59*, 3064–3076.
- (14) Ohkuma, T.; Ooka, H.; Yamakawa, M.; Ikariya, T.; Noyori, R. *J. Org. Chem.* **1996**, *61*, 4872–4873.

- (15) Noyori, R. *Angew. Chem., Int. Ed.*, **2002**, *41*, 2008–2022.
- (16) Dalko, P. I.; Moisan, L. *Angew. Chem. Int. Ed.* **2004**, *43*, 5138–5175.
- (17) List, B. *Chem. Rev.* **2007**, *107*, 5413–5415.
- (18) Leadbeater, N. E.; Marco, M. *Angew. Chem.* **2003**, *115*, 1445–1447.
- (19) Leadbeater, N. E.; Marco, M. *Angew. Chem. Int. Ed.* **2003**, *42*, 1407–1409.
- (20) Leadbeater, N. E.; Marco, M. *J. Org. Chem.* **2003**, *68*, 5660–5667.
- (21) Ikushima, Y.; Zhao, F.; Sato, M.; Zhang, R. *Chem. Commun.* **2003**, 1548–1549.
- (22) Ma, J.-A.; Cahard, D. *Angew. Chem. Int. Ed.* **2004**, *43*, 4566–4583.
- (23) Cheong, P. H.-Y.; Legault, C. Y.; Um, J. M.; Çelebi-Ölçüm, N.; Houk, K. N. *Chem. Rev.* **2011**, *111*, 5042–5137.
- (24) Greenwood, N. N.; Earnshaw, A. *Chemistry of the elements*; Butterworth-Heinemann: Oxford; Boston, 1997.
- (25) Wang, W.; Zhang, Y.; Huang, K. *J. Phys. Chem. B* **2005**, *109*, 8562–8564.
- (26) Larkin, J. D.; Bhat, K. L.; Markham, G. D.; James, T. D.; Brooks, B. R.; Bock, C. W. *J. Phys. Chem.* **2008**, *112*, 8446–8454.
- (27) Soloway, A. H.; Tjarks, W.; Barnum, B. A.; Rong, F.-G.; Barth, R. F.; Codogni, I. M.; Wilson, J. G. *Chem. Rev.* **1998**, *98*, 1515–1562.
- (28) Toyota, S.; Asakura, M.; Sakaue, T. *Bull. Chem. Soc. Jpn.* **2002**, *75*, 2667–2671.
- (29) Grabowski, S. J. *J. Phys. Org. Chem.*, **2004**, *17*, 18–31.
- (30) Nelson, P. C.; Radosavljevic, M.; Bromberg, S. *Biological physics: energy, information, life*; W.H. Freeman and Co.: New York, 2004.
- (31) June Sutor, D. *J. Chem. Soc.* **1963**, *0*, 1105–1110.
- (32) Chaney, J. D.; Goss, C. R.; Folting, K.; Santarsiero, B. D.; Hollingsworth, M. D. *J. Am.*

Chem. Soc. **1996**, *118*, 9432–9433.

- (33) Cubero, E.; Orozco, M.; Hobza, P.; Luque, F. J. *J. Phys. Chem.* **1999**, *103*, 6394–6401.
- (34) Patel, U. H.; Patel, P. D.; Thakker, N. *Acta Crystallogr., Sect. C: Cryst. Struct. Commun.* **2007**, *63*, 337–339.
- (35) Grabowski, S. J. *Relationships between QTAIM and the Decomposition of the Interaction Energy – Comparison of Different Kinds of Hydrogen Bond*, 2007, 453–469.
- (36) Matta, C. F.; Boyd, R. J. *The quantum theory of atoms in molecules: from solid state to DNA and drug design*; Wiley-VCH: Weinheim, 2007.
- (37) Corey, E. J.; Barnes-Seeman, D.; Lee, T. W. *Tetrahedron Lett.* **1997**, *38*, 1699–1702.
- (38) Corey, E. J.; Rohde, J. J. *Tetrahedron Letters*, **1997**, *38*, 37–40.
- (39) Corey, E. J.; Lee, T. W. *Chem. Commun.* **2001**, 1321–1329.
- (40) Corey, E. J.; Helal, C. J. *Angew. Chem. Int. Ed.* **1998**, *37*, 1986–2012.
- (41) Jeffrey, G. A. *An introduction to hydrogen bonding*; Oxford University Press: New York, 1997.
- (42) Steiner, T. *Angew. Chem., Int. Ed.* **2002**, *41*, 48–76.
- (43) Hugas, D.; Simon, S.; Duran, M. *J. Phys. Chem.* **2007**, *111*, 4506–4512.
- (44) Furuta, K.; Miwa, Y.; Iwanaga, K.; Yamamoto, H. *J. Am. Chem. Soc.* **1988**, *110*, 6254–6255.
- (45) Furuta, K.; Shimizu, S.; Miwa, Y.; Yamamoto, H. *J. Org. Chem.* **1989**, *54*, 1481–1483.
- (46) Gao, Q.; Maruyama, T.; Mouri, M.; Yamamoto, H. *J. Org. Chem.* **1992**, *57*, 1951–1952.
- (47) Corey, E. J.; Loh, T. P.; Roper, T. D.; Azimioara, M. D.; Noe, M. C. *J. Am. Chem. Soc.* **1992**, *114*, 8290–8292.
- (48) Hayashi, Y.; Rohde, J. J.; Corey, E. J. *J. Am. Chem. Soc.* **1996**, *118*, 5502–5503.

- (49) Corey, E. J.; Barnes-Seeman, D.; Lee, T. W. *Tetrahedron Lett.* **1997**, *38*, 4351–4354.
- (50) Corey, E. J.; Barnes-Seeman, D.; Lee, T. W.; Goodman, S. N. *Tetrahedron Lett.* **1997**, *38*, 6513–6516.
- (51) Corey, E. J.; Rohde, J. J.; Fischer, A.; Azimioara, M. D. *Tetrahedron Lett.* **1997**, *38*, 33–36.
- (52) Reetz, M. T.; Huellmann, M.; Massa, W.; Berger, S.; Rademacher, P.; Heymanns, P. *J. Am. Chem. Soc.* **1986**, *108*, 2405–2408.
- (53) Gung, B. W. *Tetrahedron Lett.* **1991**, *32*, 2867–2870.
- (54) Gung, B. W.; Wolf, M. A. *J. Org. Chem.* **1992**, *57*, 1370–1375.
- (55) Gung, B. W.; Karipides, A.; Wolf, M. A. *Tetrahedron Lett.* **1992**, *33*, 713–716.
- (56) Mackey, M. D.; Goodman, J. M. *Chem. Commun.* **1997**, 2383–2384.
- (57) Feng, Y.; Liu, L.; Zhao, S.-W.; Wang, J.-T.; Guo, Q.-X. *J. Phys. Chem.* **2004**, *108*, 9196–9204.
- (58) Ryu, D. H.; Corey, E. J. *J. Am. Chem. Soc.* **2005**, *127*, 5384–5387.
- (59) Ogoshi, S.; Yoshida, T.; Nishida, T.; Morita, M.; Kurosawa, H. *J. Am. Chem. Soc.* **2001**, *123*, 1944–1950.
- (60) Ryu, D. H.; Lee, T. W.; Corey, E. J. *J. Am. Chem. Soc.* **2002**, *124*, 9992–9993.
- (61) Morita, M.; Inoue, K.; Yoshida, T.; Ogoshi, S.; Kurosawa, H. *J. Organomet. Chem.* **2004**, *689*, 894–898.
- (62) Yasuda, M.; Yoshioka, S.; Nakajima, H.; Chiba, K.; Baba, A. *Org. Lett.* **2008**, *10*, 929–932.
- (63) Andrews, G. C.; Crawford, T. C. *Tetrahedron Lett.* **1980**, *21*, 693–696.
- (64) Fiaud, J.-C.; Mazé, F.; Kagan, H. B. *Tetrahedron: Asymmetry* **1998**, *9*, 3647–3655.

(65) Frisch, M. J.; Trucks, G. W.; Schlegel, H. B.; Scuseria, G. E.; Robb, M. A.; Cheeseman, J. R.; Scalmani, G.; Barone, V.; Mennucci, B.; Petersson, G. A.; Nakatsuji, H.; Caricato, M.; Li, X.; Hratchian, H. P.; Izmaylov, A. F.; Bloino, J.; Zheng, G.; Sonnenberg, J. L.; Hada, M.; Ehara, M.; Toyota, K.; Fukuda, R.; Hasegawa, J.; Ishida, M.; Nakajima, T.; Honda, Y.; Kitao, O.; Nakai, H.; Vreven, T.; Montgomery, J. A. J.; Peralta, J. E.; Ogliaro, F.; Bearpark, M.; Heyd, J. J.; Brothers, E.; Kudin, K. N.; Staroverov, V. N.; Kobayashi, R.; Normand, J.; Raghavachari, K.; Rendell, A.; Burant, J. C.; Iyengar, S. S.; Tomasi, J.; Cossi, M.; Rega, N.; Millam, J. M.; Klene, M.; Knox, J. E.; Cross, J. B.; Bakken, V.; Adamo, C.; Jaramillo, J.; Gomperts, R.; Stratmann, R. E.; Yazyev, O.; Austin, A. J.; Cammi, R.; Pomelli, C.; Ochterski, J. W.; Martin, R. L.; Morokuma, K.; Zakrzewski, V. G.; Voth, G. A.; Salvador, P.; Dapprich, S.; Daniels, A. D.; Farkas, Ö.; Foresman, J. B.; Ortiz, J. V.; Cioslowski, J.; Fox, D. J. Gaussian 09 Revision B.01, Gaussian, Inc., Wallingford CT, 2010.

(66) Perdew, J. P.; Ernzerhof, M.; Burke, K. *J. Chem. Phys.* **1996**, *105*, 9982–9985.

(67) Perdew, J. P.; Burke, K.; Ernzerhof, M. *Phys. Rev. Lett.* **1996**, *77*, 3865–3868.

(68) Perdew, J. P.; Burke, K.; Ernzerhof, M. *Phys. Rev. Lett.* **1997**, *78*, 1396.

(69) Adamo, C.; Barone, V. *J. Chem. Phys.* **1999**, *110*, 6158–6170.

(70) Møller, C.; Plesset, M. S. *Phys. Rev.* **1934**, *46*, 618–622.

(71) Pople, J. A.; Head-Gordon, M.; Frisch, M. J. *Chem. Phys. Lett.* **1988**, *153*, 503–506.

(72) Head-Gordon, M.; Frisch, M. J.; Pople, J. A. *Chem. Phys. Lett.* **1990**, *166*, 275–280.

(73) Frisch, M. J.; Head-Gordon, M.; Pople, J. A. *Chem. Phys. Lett.* **1990**, *166*, 281–289.

(74) Head-Gordon, M.; Head-Gordon, T. *Chem. Phys. Lett.* **1994**, *220*, 122–128.

(75) Boys, S. F.; Bernardi, F. *Mol. Phys.* **1970**, *19*, 553–566.

(76) Keith, T. A. AIMAll (Version 14.04.17), TK Gristmill Software, Overland Park KS USA,

2014.

(77) Bader, R. *Atoms in molecules: a quantum theory*; Clarendon Press: Oxford; New York, 1990.

(78) Popelier, P. *Atoms in Molecules An Introduction*; Pearson Education: Edinburgh Gate, UK, 2000.

(79) Weinhold, F.; Landis, C. R. *Chem. Educ.: Res. Pr. Eur.* **2001**, *2*, 91–104.

(80) Weinhold, F.; Landis, C. R. *Discovering chemistry with natural bond orbitals*, 2012.

(81) Glendening, E. D.; Weinhold, F. *J. Comput. Chem.* **1998**, *19*, 593–609.

(82) Feldgus, S.; Landis, C. R.; Glendening, E. D.; Weinhold, F. *J. Comput. Chem.* **2000**, *21*, 411–413.

(83) Glendening, E. D.; Weinhold, F. *J. Comp. Chem* **1998**, *19*, 610–627.

(84) Foster, J. P.; Weinhold, F. *J. Am. Chem. Soc.* **1980**, *102*, 7211–7218.

(85) Glendening, E. D.; Badenhop, J. K.; Reed, A. E.; Carpenter, J. E.; Bohmann, J. A.; Morales, C. M.; Weinhold, F. NBO 5.G, 2004.

(86) Hansch, C.; Leo, A.; Taft, R. W. *Chem. Rev.* **1991**, *91*, 165–195.

(87) Glendening, E. D.; Badenhop, J. K.; Weinhold, F. *J. Comput. Chem.* **1998**, *19*, 628–646.

(88) Bertrand, G.. *Reactive intermediate chemistry*; Eds Moss, R. A.; Platz, M.; Jones, M Wiley-Interscience: Hoboken, N.J., 2004. pp.329.

(89) MacDougall, P. J.; Bader, R. F. W. *Can. J. Chem.* **1986**, *64*, 1496–1508.

(90) Olah, G. A.; White, A. M. *J. Am. Chem. Soc.* **1968**, *90*, 1884–1889.

(91) Wentrup, C. *Reaktive Zwischenstufen II. Carbokationen, Carbanionen, Zwitterionen.*; Thieme: Stuttgart, 1979.

(92) LePage, T. J.; Wiberg, K. B. *J. Am. Chem. Soc.* **1988**, *110*, 6642–6650.

- (93) Dennington, Roy; Keith, Todd; Millam, John. Semichem Inc., GaussView, Version 5, Shawnee Mission, KS, 2009.
- (94) Haynes, W. M.; Lide, D. R. *CRC handbook of chemistry and physics a ready-reference book of chemical and physical data: 2011-2012*; CRC Press: Boca Raton (Fla.); London; New York, 2011.
- (95) Corey, E. J.; Bakshi, R. K.; Shibata, S. *J. Am. Chem. Soc.* **1987**, *109*, 5551–5553.
- (96) Nevalainen, V. *Tetrahedron: Asymmetry* **1991**, *2*, 63–74.
- (97) Nevalainen, V. *Tetrahedron: Asymmetry* **1991**, *2*, 429–435.
- (98) Deloux, L.; Srebnik, M. *Chem. Rev.* **1993**, *93*, 763–784.
- (99) Ager, D. J.; Prakash, I.; Schaad, D. R. *Chem. Rev.* **1996**, *96*, 835–876.
- (100) Anderson, C. D.; Dudding, T.; Gordillo, R.; Houk, K. N. *Org. Lett.* **2008**, *10*, 2749–2752.
- (101) Huang, Y.; Unni, A. K.; Thadani, A. N.; Rawal, V. H. *Nature* **2003**, *424*.
- (102) Stankovic, A. R.; Rawal, V. H.; Thadani, A. N. *Proc. Natl. Acad. Sci.* **2004**, *101*, 5846–5850.
- (103) Seebach, D.; Beck, A. K.; Heckel, A. *Angew. Chem. Int. Ed.* **2001**, *40*, 92–138.
- (104) Zhang, X.; Du, H.; Wang, Z.; Wu, Y.-D.; Ding, K. *J. Org. Chem.* **2006**, *71*, 2862–2869.
- (105) Harriman, D. J.; Deslongchamps, G. *J. Mol. Model.* **2006**, *12*, 793–797.
- (106) Harriman, D. J.; Lambropoulos, A.; Deslongchamps, G. *Tetrahedron Lett.* **2007**, *48*, 689–692.
- (107) Zhao, Y.; Truhlar, D. *Theor. Chem. Accounts* **2008**, *120*, 215–241.
- (108) Brown, H. C.; Jadav, P. K. *J. Org. Chem.* **1981**, *46*, 5047–5048.
- (109) Brown, H. C.; Jadhav, P. K.; Mandal, A. K. *Tetrahedron* **1981**, *37*, 3547–3587.
- (110) Brown, H. C.; Desai, M. C.; Jadhav, P. K. *J. Org. Chem.* **1982**, *47*, 5065–5069.

- (111) Midland, M. M. In *Asymmetric Synth.*; Academic, 1983; Vol. 2, pp. 45–69.
- (112) Brown, H. C.; Jadhav, P. K.; Singram, B. *Mod. Synth. Methods* **1986**, 4, 307–356.
- (113) Pelter, A.; Smith, K.; Brown, H. C. *Borane reagents*; Acad. Press: London, 1988.
- (114) Corey, E. J.; Bakshi, R. K.; Shibata, S.; Chen, C. P.; Singh, V. K. *J. Am. Chem. Soc.* **1987**, 109, 7925–7926.
- (115) Corey, E. J.; Shibata, S.; Bakshi, R. K. *J. Org. Chem.* **1988**, 53, 2861–2863.
- (116) Corey, E. J. *Pure Appl. Chem.* **1990**, 62, 1209–1216.
- (117) Nevalainen, V. *Tetrahedron: Asymmetry* **1991**, 2, 827–842.
- (118) Nevalainen, V. *Tetrahedron: Asymmetry* **1991**, 2, 1133–1155.
- (119) Nevalainen, V. *Tetrahedron: Asymmetry* **1992**, 3, 921–932.
- (120) Nevalainen, V. *Tetrahedron: Asymmetry* **1992**, 3, 933–945.
- (121) Nevalainen, V. *Tetrahedron: Asymmetry* **1992**, 3, 1441–1453.
- (122) Nevalainen, V. *Tetrahedron: Asymmetry* **1992**, 3, 1563–1572.
- (123) Nevalainen, V. *Tetrahedron: Asymmetry* **1993**, 4, 1505–1519.
- (124) Nevalainen, V. *Tetrahedron: Asymmetry* **1993**, 4, 1565–1568.
- (125) Nevalainen, V. *Tetrahedron: Asymmetry* **1993**, 4, 1569–1572.
- (126) Nevalainen, V. *Tetrahedron: Asymmetry* **1993**, 4, 1597–1602.
- (127) Nevalainen, V. *Tetrahedron: Asymmetry* **1993**, 4, 2001–2010.
- (128) Nevalainen, V. *Tetrahedron: Asymmetry* **1993**, 4, 2517–2530.
- (129) Nevalainen, V. *Tetrahedron: Asymmetry* **1994**, 5, 289–296.
- (130) Nevalainen, V. *Tetrahedron: Asymmetry* **1994**, 5, 387–394.
- (131) Nevalainen, V. *Tetrahedron: Asymmetry* **1994**, 5, 395–402.
- (132) Nevalainen, V. *Tetrahedron: Asymmetry* **1994**, 5, 767–772.

- (133) Nevalainen, V. *Tetrahedron: Asymmetry* **1994**, *5*, 903–908.
- (134) Self, C. R.; Williams, I. H.; Linney, L. P. *J. Chem. Soc., Chem. Commun.* **1994**, 1651–1652.
- (135) Corey, E. J.; Link, J. O.; Bakshi, R. K. *Tetrahedron Lett.* **1992**, *33*, 7107–7110.
- (136) Alagona, G.; Ghio, C.; Tomasi, S. *Theor. Chem. Acc.* **2004**, *111*, 287–302.
- (137) Alagona, G.; Ghio, C.; Persico, M.; Tomasi, S. *J. Am. Chem. Soc.* **2003**, *125*, 10027–10039.
- (138) Li, M.; Tian, A. *J. Mol. Struct.: THEOCHEM* **2001**, *544*, 25–35.
- (139) Li, M.; Tian, A. *J. Mol. Struct.: THEOCHEM* **2001**, *544*, 37–47.
- (140) Becke, A. D. *J. Chem. Phys.* **1993**, *98*, 5648–5652.
- (141) Lee, C.; Yang, W.; Parr, R. G. *Phys. Rev. B: Condens. Matter* **1988**, *37*, 785–789.
- (142) Stephens, P. J.; Devlin, F. J.; Chabalowski, C. F.; Frisch, M. J. *J. Phys. Chem.* **1994**, *98*, 11623–11627.
- (143) Chai, J.-D.; Head-Gordon, M. *Phys. Chem. Chem. Phys.* **2008**, *10*, 6615–6620.
- (144) Boese, R.; Maulitz, A. H.; Stellberg, P. *Chem. Berichte* **1994**, *127*, 1887–1889.
- (145) Corey, E. J.; Azimioara, M.; Sarshar, S. *Tetrahedron Lett.* **1992**, *33*, 3429–3430.
- (146) Mathre, D. J.; Thompson, A. S.; Douglas, A. W.; Hoogsteen, K.; Carroll, J. D.; Corley, E. G.; Grabowski, E. J. *J. Org. Chem.* **1993**, *58*, 2880–2888.
- (147) Corcoran, R. C.; Ma, J. *J. Am. Chem. Soc.* **1992**, *114*, 4536–4542.

Appendix A

Chapter 3 supplementary information

S 1. Total energies, zero-point corrected electronic energies and free energies (Hartree) of acetophenone and substituted boranes.^a

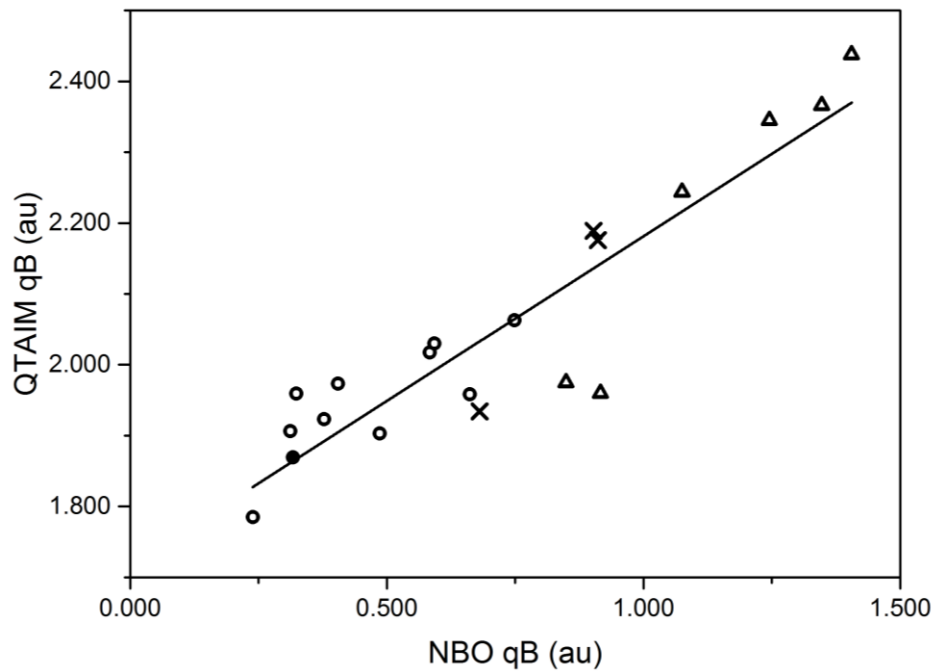
	PBE0		MP2	
	E	E + ZPVE	G	E
Acetophenone	-384.549291	-384.411142	-384.443917	-383.947469
BH₃	-26.564389	-26.538270	-26.555824	-26.499494
BH₂F	-125.827868	-125.805399	-125.827458	-125.688245
BH₂Cl	-486.092180	-486.071097	-486.093734	-485.636588
BH₂Br	-2599.839709	-2599.819122	-2599.843001	-2598.459164
BF₃	-324.353231	-324.340820	-324.366965	-324.065447
BH₂CH₃	-65.862692	-65.807141	-65.830425	-65.721197
BH(CH₃)₂	-105.159713	-105.075405	-105.102313	-104.943151
B(CH₃)₃	-144.454490	-144.342038	-144.374339	-144.164697
BH₂OCH₃	-141.076062	-141.012305	-141.037513	-140.862783
BH(OCH₃)₂	-255.577488	-255.478804	-255.509075	-255.217038
B(OCH₃)₃	-370.074815	-369.941629	-369.977493	-369.570822
BH₂OH	-101.818489	-101.783012	-101.805190	-101.655396
BH(OH)₂	-177.066343	-177.023510	-177.047981	-176.855374
BH₂NH₂	-81.957672	-81.909617	-81.932018	-81.817829
BH₂NH₃⁺	-82.255650	-82.195313	-82.219748	-82.114969
BH₂CN	-118.748235	-118.720340	-118.743642	-118.574292
BH₂NO₂	-230.968587 ^b	-230.935227	-230.961013	-230.687755
BNO₂OCH₃N(CH₃)₂	-479.374663	-479.231469	-479.270018	
B(C₆F₅)₃	-2206.769150	-2206.612189	-2206.673688	
B(cage)	-981.636447	-981.357780	-981.400315	

^a 6-311++G(2d,p) basis set. ^b The total energy for the restrained optimization is -230.960887 au.

S 2. Total energies, counterpoise corrected electronic energies, zero-point corrected electronic energies and free energies (Hartree) of acetophenone-borane complexes.^a

	PBE0			G	MP2
	E	E+CP	E +ZPVE		E
1k	-411.148740	-411.148073	-410.978608	-411.014062	-410.476539
2k	-510.3993368	-510.3980935	-510.234619	-510.271542	-509.6536314
3k	-870.6693027	-870.6679907	-870.505749	-870.54416	-869.6097313
4k	-2984.419408	-2984.418237	-2984.256456	-2984.296136	-2982.435476
5k	-708.924449	-708.921772	-708.771748	-708.812229	-708.034377
6k	-450.433766	-450.432997	-450.234918	-450.272868	-449.690970
7k	-489.717674	-489.716833	-489.490926	-489.531350	-488.904600
8k	-529.005834	-529.004862	-528.751450	-528.793746	-528.123215
9k	-525.629598	-525.628529	-525.425377	-525.465779	-524.816633
10k	-640.130560	-640.129701	-639.892997	-639.942465	
11k	-754.626381	-754.625440	-754.354444	-754.408480	
12k	-486.373837	-486.372658	-486.197114	-486.234643	-485.635071
13k	-561.619829	-561.619037	-561.437949	-561.481661	
14k	-466.507707	-466.507538	-466.320967	-466.367715	-465.767963
15k	-466.908988	-466.9079004	-466.704561	-466.742791	-466.1602503
16k	-503.3420748	-503.3411821	-503.171048	-503.210044	-502.5629154
17k	-615.5588026	-615.5573698	-615.383401	-615.424106	-612.5695616
18k	-863.917190	-863.917190	-863.634565	-863.684992	
19k	-2591.338207	-2591.338207	-2591.040735	-2591.112354	
20k	-1366.202285	-1366.202285	-1365.784002	-1365.839411	

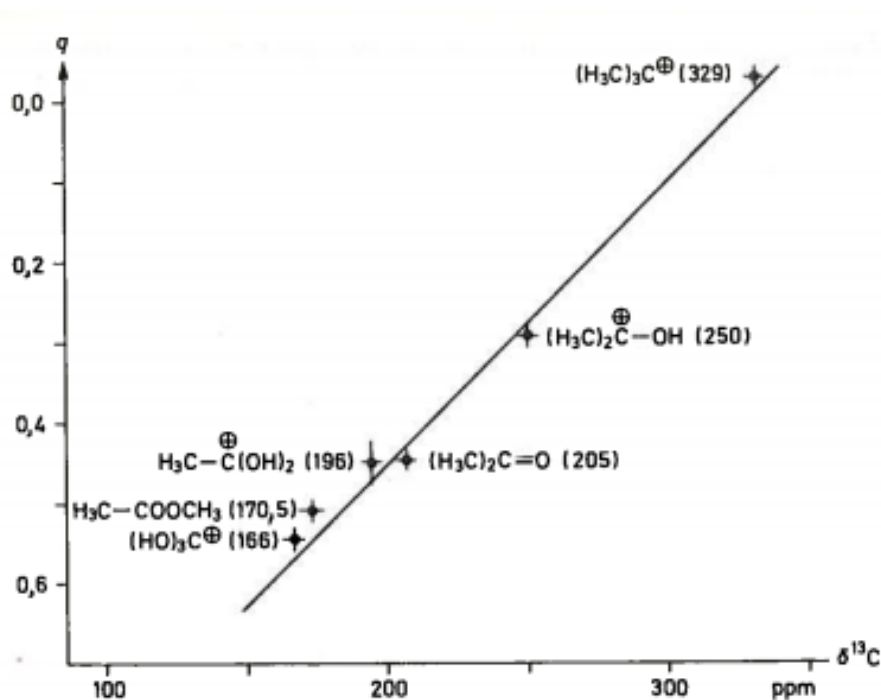
^a 6-311++G(2d,p) basis set.



S 3. Comparison of q_B obtained from QTAIM and NBO. Symbols are borane (●), mono-substituted boranes (○), di-substituted boranes (×) and tri-substituted boranes (Δ).

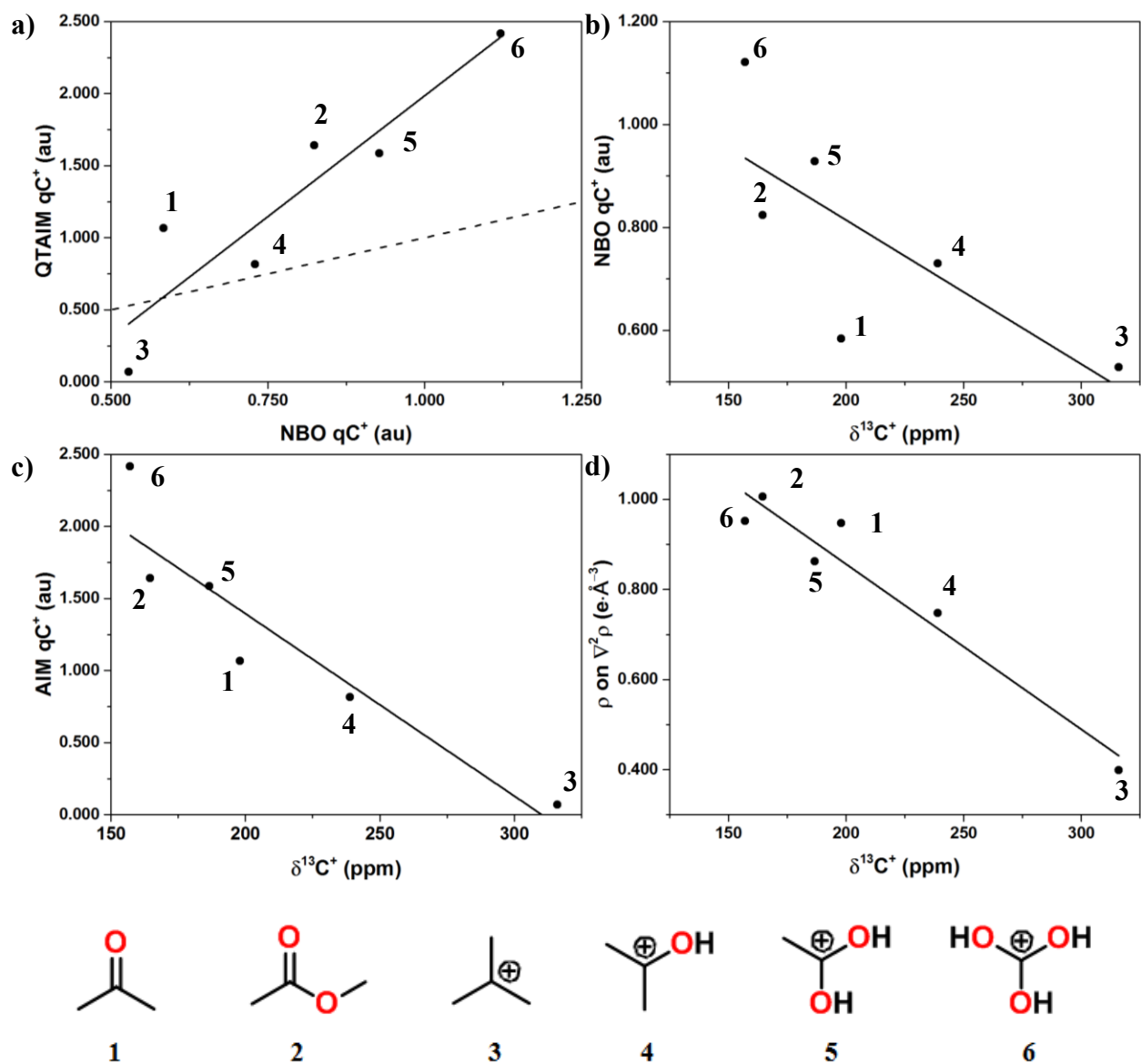
S 4: ρ -on- $\nabla^2\rho$ isosurface proof of principle

Concept: As the π -electron density at C^+ of a carboncation decreases, its ^{13}C chemical shift will increase.



S 4.1: Calculated π -electron densities using Hückel theory in a linear relationship with $\delta^{13}\text{C}^+$. Reproduced from Olah, G. A.; White, A. M. *J. Am. Chem. Soc.* **1968**, *90*, 1884–1889 and Wentrup, C. *Reaktive Zwischenstufen II. Carbokationen, Carbanionen, Zwitterionen*, Thieme, Stuttgart, 1979. p. 291

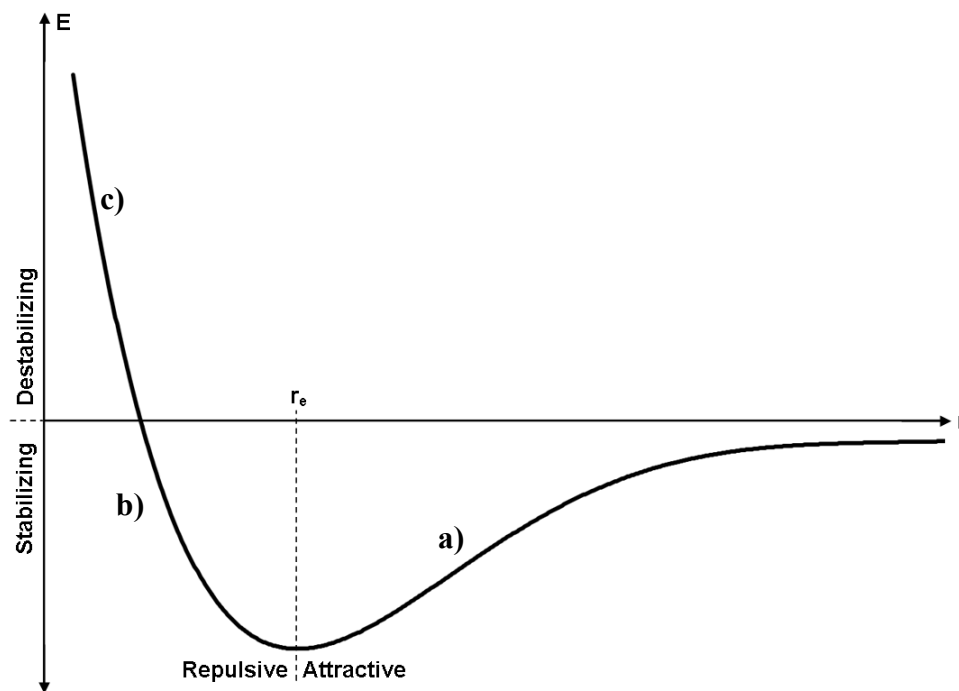
There are various ways that the π -electron density can be estimated; in this case, we are testing whether determining ρ on a particular $\nabla^2\rho$ isosurface can replicate the aforementioned concept. QTAIM and NBO charges were tested as well, even though σ and π effects from a substituent onto the atom in question, here C^+ , can be conflicting/opposed and render the charge as a monitor useless.



S 4.2: Electronic relationships for small molecules with partial (1 and 2) or formally full positive charge (3-6) on carbon: a) comparison of qC^+ from QAIM and NBO (the dashed line represents the 1:1 correspondance); b) NBO qC^+ relation with $\delta^{13}C^+$; c) QAIM qC^+ relation with $\delta^{13}C^+$; d) ρ on $-\nabla^2\rho$ relation with $\delta^{13}C^+$. Chemical shift values were calculated using OPBE/6-311++(2df,pd)//PBE0/6-311++(2df,pd).

While obviously not perfect, and not expected to be the same, qC^+ obtained from QTAIM and NBO are only somewhat comparable. The greater source of the scatter in S4.2a stems from the NBO charges, which are unable to replicate the relationship between qC^+ and $\delta^{13}C^+$ (S4.2b). QTAIM charges seem to be more promising as the correlation (S4.2c) seems improved over that in S4.2.b. As discussed in Section 3.2.1, mapping ρ onto an appropriate $\nabla^2\rho$ isosurface is meant to provide an estimate of the $2p_z$ occupancy (of B or here of C^+), i.e., the π -electron density at C^+ . As shown in S4.2d, these ρ -on- $\nabla^2\rho$ density values decrease as $\delta^{13}C^+$ increases, similar to the Hückel π -electron densities (S4.1). The advantage of the ρ -on- $\nabla^2\rho$ over the Hückel approach lies in the quantum chemical derivation of the former.

S 5: Morse potential curve with various types of interactions in a diatomic system



- a) stabilizing-attractive interactions
- b) stabilizing-repulsive interactions
- c) destabilizing-repulsive interactions

Appendix B

Chapter 4 supplementary information

S 1: Total energies and free energies (Hartree).^a

	B3LYP		PBE0		ωB97X-D	
	E	G	E	G	E	G
BH₃	-26.617764	-26.609032	-26.560641	-26.552023	-26.602603	-26.594030
Ketone	-311.133349	-310.998274	-310.756800	-310.620830	-311.038296	-310.902015
CBS	-351.484659	-351.361318	-351.069919	-350.945252	-351.376160	-351.250426
CBS-BH₃	-378.138503	-377.983442			-378.025082	-377.867526
CBS-dBH₃	-378.141901	-377.985079	-377.686978	-377.528774	-378.031400	-377.872224
1	-689.271226	-688.958099	-688.441873	-688.125939	-689.077919	-688.758491
2	-689.270298	-688.956159	-688.441000	-688.124386	-689.077232	-688.757971
3	-689.267872	-688.953924	-688.438284	-688.122115	-689.072188	-688.753316
4	-689.267422	-688.952986	-688.438104	-688.121553	-689.074343	-688.752403
5	-689.266337	-688.951487	-688.437405	-688.120423	-689.073318	-688.751421
6	-689.260699	-688.947503	-688.430396	-688.113744	-689.067335	-688.747131
7	-689.276162	-688.970260	-688.449565	-688.140144	-689.083821	-688.767666
8	-689.275490	-688.971067	-688.447495	-688.138720	-689.075807	-688.762435
9	-689.277251	-688.972388	-688.449697	-688.139524	-689.078075	-688.763133
10	-689.276519	-688.972497			-689.077778	-688.765474
11	-689.279539	-688.973070	-688.449697	-688.139516	-689.084268	-688.766259
12	-689.279489	-688.972773	-688.449565	-688.140146	-689.083822	-688.767693
13	-689.276220	-688.971392	-688.448411	-688.139266	-689.076477	-688.760752
14	-689.276558	-688.971283	-688.449706	-688.138431	-689.077889	-688.763151
15	-689.275829	-688.972193	-688.449130	-688.138546	-689.084051	-688.767991
TS 1	-689.266688	-688.950063	-688.439593	-688.120955	-689.075684	-688.753663
TS 2	-689.261679	-688.945049	-688.434737	-688.115671	-689.069321	-688.747590
TS 3	-689.259685	-688.943503	-688.432936	-688.114464	-689.068089	-688.745497
TS 4	-689.257272	-688.940266	-688.429908	-688.110851	-689.066423	-688.743340
TS 5	-689.225446	-688.911482	-688.402062	-688.086385	-689.035387	-688.716673
TS 6	-689.188605	-688.875508	-688.359660	-688.044220	-688.995107	-688.677198
TS 7	-689.188363	-688.875115	-688.359236	-688.043765	-688.994726	-688.675307
Un-cat R	-337.828104	-337.658881	-337.352842	-337.186463	-337.672944	-337.506304
Un-cat TS	-337.752399	-337.587390	-337.328208	-337.162987	-337.649789	-337.482506
Un-cat P	-337.778823	-337.613656	-337.402145	-337.232217	-337.724845	-337.553431

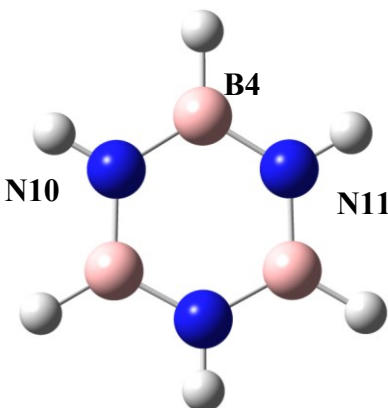
^a 6-31+G(2d,2p) basis set.

S 2: Tabulated BSSE correction energies (kcal·mol⁻¹) by counterpoise method.^a

	BSSE				
	1	10	12	CBS-BH₃	CBS-dBH₃
B3LYP/6-31+G(2d,2p)	1.2 (2.0)	0.3	0.4	0.9	1.1
B3LYP/6-311++G(2d,p)	0.9 (1.4)	0.3	0.4	0.6	0.7
PBE0/6-31+G(2d,2p)	1.2	0.3	0.3		
PBE0/6-311++G(2d,p)	1.1	0.4	0.4		
ωB97X-D/6-31+G(2d,2p)	1.2	0.5	0.5		
ωB97X-D /6-311++G(2d,p)	1.1	0.7	0.5		

^a Calculations were performed using counterpoise=2, with the catalyst-borane adduct and the ketone as fragments. Values in parentheses are from counterpoise=3 calculations, with all three components as fragments (CBS, borane, ketone).

S 3: Borazine B3LYP/6-31+G(2d,2p) NBO partial output.



```

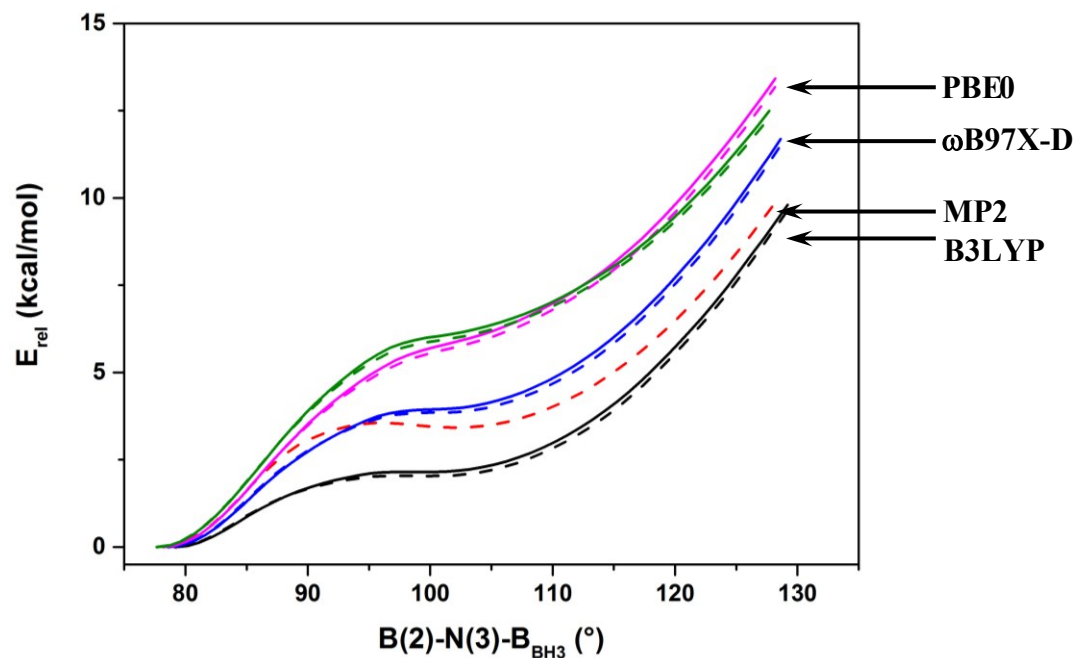
5. (1.98305) BD ( 1) B  4 - N 10
   ( 23.75%)  0.4873* B  4 s ( 31.40%)p 2.18( 68.32%)d 0.01(  0.28%)
               0.0002 -0.5600  0.0202  0.0040  0.0011
               -0.0002 -0.6182  0.0024  0.0122  0.5464
               -0.0485 -0.0096  0.0000  0.0000  0.0000
               0.0460  0.0015  0.0000  0.0000  0.0000
               0.0000 -0.0176 -0.0096  0.0116 -0.0125
   ( 76.25%)  0.8732* N 10 s ( 38.02%)p 1.63( 61.83%)d 0.00(  0.16%)
               0.0001 -0.6165 -0.0098 -0.0022  0.0001
               0.0000  0.6114 -0.0062 -0.0062 -0.4942
               -0.0123  0.0076  0.0000  0.0000  0.0000
               0.0319 -0.0006  0.0000  0.0000  0.0000
               0.0000  0.0019 -0.0024  0.0234  0.0009

6. (1.98306) BD ( 1) B  4 - N 11
   ( 23.75%)  0.4873* B  4 s ( 31.40%)p 2.18( 68.32%)d 0.01(  0.28%)
               0.0002 -0.5600  0.0202  0.0040  0.0010
               -0.0002 -0.2049 -0.0252  0.0047 -0.7991
               0.0416  0.0148  0.0000  0.0000  0.0000
               -0.0334 -0.0095  0.0000  0.0000  0.0000
               0.0000  0.0362 -0.0022  0.0116 -0.0125
   ( 76.25%)  0.8732* N 11 s ( 38.02%)p 1.63( 61.82%)d 0.00(  0.16%)
               0.0001 -0.6165 -0.0098 -0.0022  0.0001
               0.0000  0.2286 -0.0121 -0.0008  0.7521
               0.0067 -0.0098  0.0000  0.0000  0.0000
               -0.0100 -0.0020  0.0000  0.0000  0.0000
               0.0000  0.0304 -0.0014  0.0234  0.0009

7. (1.82581) BD ( 2) B  4 - N 11
   ( 11.27%)  0.3357* B  4 s (  0.00%)p 1.00( 99.73%)d 0.00(  0.27%)
               0.0000  0.0000  0.0000  0.0000  0.0000
               0.0000  0.0000  0.0000  0.0000  0.0000
               0.0000  0.0000  0.9983  0.0135  0.0250
               0.0000  0.0000  0.0149 -0.0012  0.0495
               0.0007  0.0000  0.0000  0.0000  0.0000
   ( 88.73%)  0.9420* N 11 s (  0.00%)p 1.00( 99.99%)d 0.00(  0.01%)
               0.0000  0.0000  0.0000  0.0000  0.0000
               0.0000  0.0000  0.0000  0.0000  0.0000
               0.0000  0.0000  0.9998  0.0115  0.0165
               0.0000  0.0000  0.0063 -0.0006 -0.0059
               -0.0002  0.0000  0.0000  0.0000  0.0000
    
```

S 4: CBS Catalyst B3LYP/6-31+G(2d,2p) NBO partial output.

17.	(1.98135)	BD (1)	N 13 - B 14							
	(77.63%)			0.8811*	N 13 s(42.53%)p 1.35(57.24%)d 0.01(0.22%)					
					-0.0001 0.6521 0.0048 -0.0038 0.0025					
					0.0000 0.6090 -0.0130 -0.0117 0.3987					
					0.0116 -0.0025 -0.2050 0.0019 0.0060					
					0.0118 0.0013 -0.0375 0.0029 -0.0144					
					-0.0002 0.0207 -0.0009 -0.0073 -0.0002					
	(22.37%)			0.4729*	B 14 s(31.20%)p 2.20(68.50%)d 0.01(0.30%)					
					0.0003 0.5583 -0.0014 -0.0169 -0.0006					
					0.0004 -0.6507 0.0388 0.0063 -0.2170					
					-0.0150 0.0079 0.4610 -0.0147 0.0022					
					0.0330 0.0080 -0.0311 0.0046 -0.0126					
					0.0019 0.0234 -0.0024 0.0054 0.0084					
18.	(1.92986)	BD (2)	N 13 - B 14							
	(87.82%)			0.9371*	N 13 s(0.24%)p99.99(99.70%)d 0.26(0.06%)					
					0.0001 0.0422 -0.0239 -0.0057 -0.0006					
					-0.0002 0.1035 -0.0005 0.0054 0.2652					
					-0.0108 0.0064 0.9566 -0.0154 0.0207					
					0.0022 -0.0001 0.0114 -0.0010 -0.0128					
					0.0018 0.0039 -0.0004 -0.0174 -0.0001					
	(12.18%)			0.3490*	B 14 s(0.62%)p99.99(99.03%)d 0.57(0.35%)					
					-0.0005 -0.0764 0.0168 0.0034 0.0043					
					-0.0013 0.4112 -0.0167 -0.0045 0.3408					
					0.0109 0.0070 0.8370 0.0578 0.0255					
					-0.0295 -0.0022 -0.0281 -0.0083 -0.0084					
					-0.0044 -0.0102 -0.0007 0.0394 0.0054					

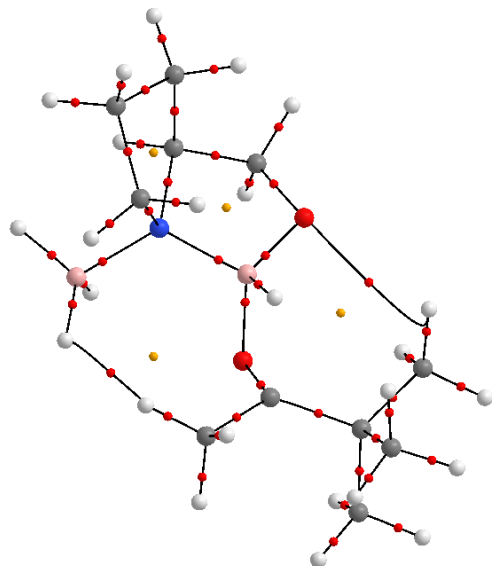


S 5: Energy ($\text{kcal}\cdot\text{mol}^{-1}$) profiles of relaxed scans of catalyst-borane adducts. Profiles obtained using a double zeta basis set (6-31+G(2d,2p)) are shown with a solid line, those obtained using a triple zeta basis set (6-311++G(2d,2p)) with a dashed line. B3LYP (black), MP2 (red), ω B97X-D (blue) and PBE0 (magenta and olive green). The olive green line stems from a scan in which a different catalyst conformation was used (pyrrolidine ring in the catalyst framework with a half-chair instead of an envelope conformation). The relative energies are referenced to the CBS-dBH₃ complexes of each functional, and the scans were performed by increasing the B(2)-N(3)-B_{BH₃} angle every degree for 50 degrees.

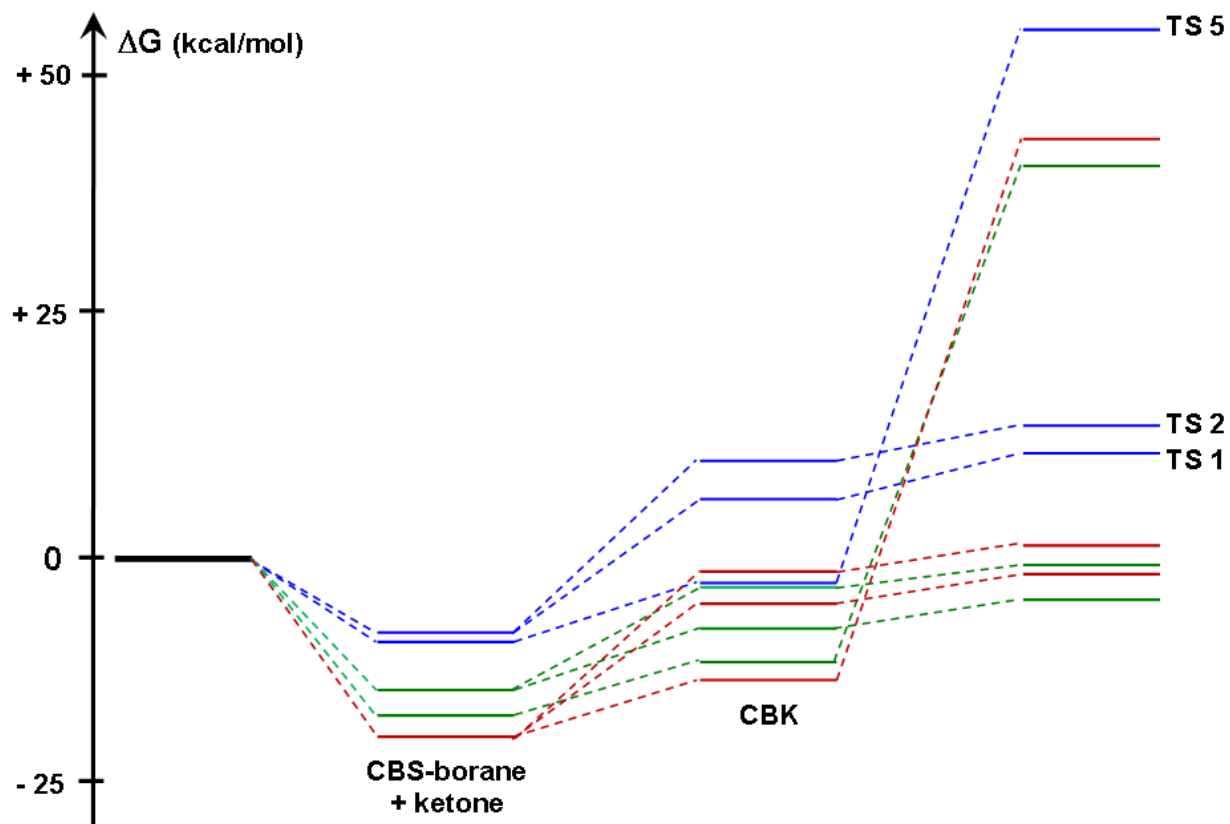
S 6: Tabulated NRT structures of highest probability and their assigned weights for CBS, CBS-BH₃ and CBS-dBH₃.

	Resonance Structure weights (%)			
	B3LYP ^a	PBE0 ^a	ω B97X-D ^a	MP2 ^b
	73.6	72.5	73.7	77.7
	8.9	9.1	8.7	6.6
	76.8	75.9 ^c	77.2	80.9
	2.6	2.2 ^c	2.1	1.4
	29.1	34.1	30.6	34.0
	22.3	18.2	19.8	24.9
	20.0	18.1	21.7	17.4
	2.5	2.1	2.5	1.6

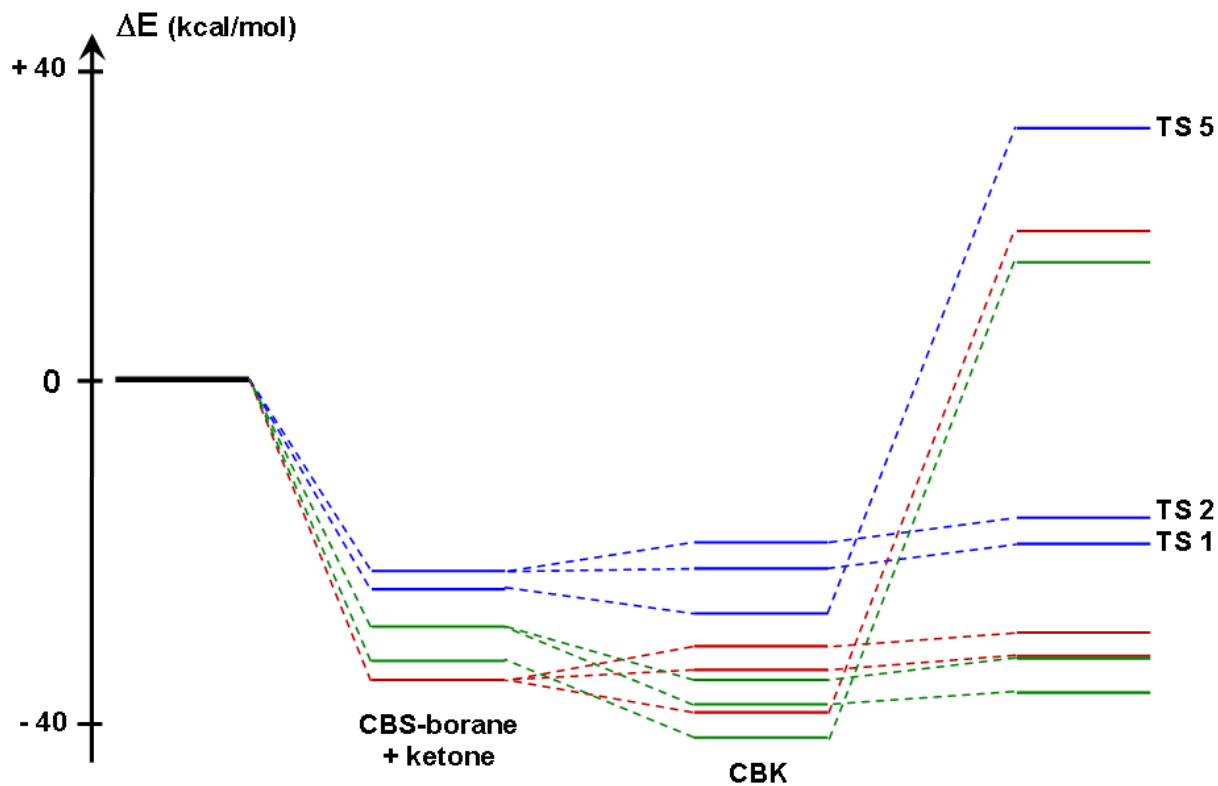
^a 6-31+G(2d,2p) basis set. ^b 6-311++G(2d,p) basis set. ^c Obtained from a geometry optimization in which the N-B-N angle was fixed at the average value obtained using B3LYP/6-31+G(2d,2p), ω B97X-D/6-31+G(2d,2p) and MP2/6-311++G(2d,p).



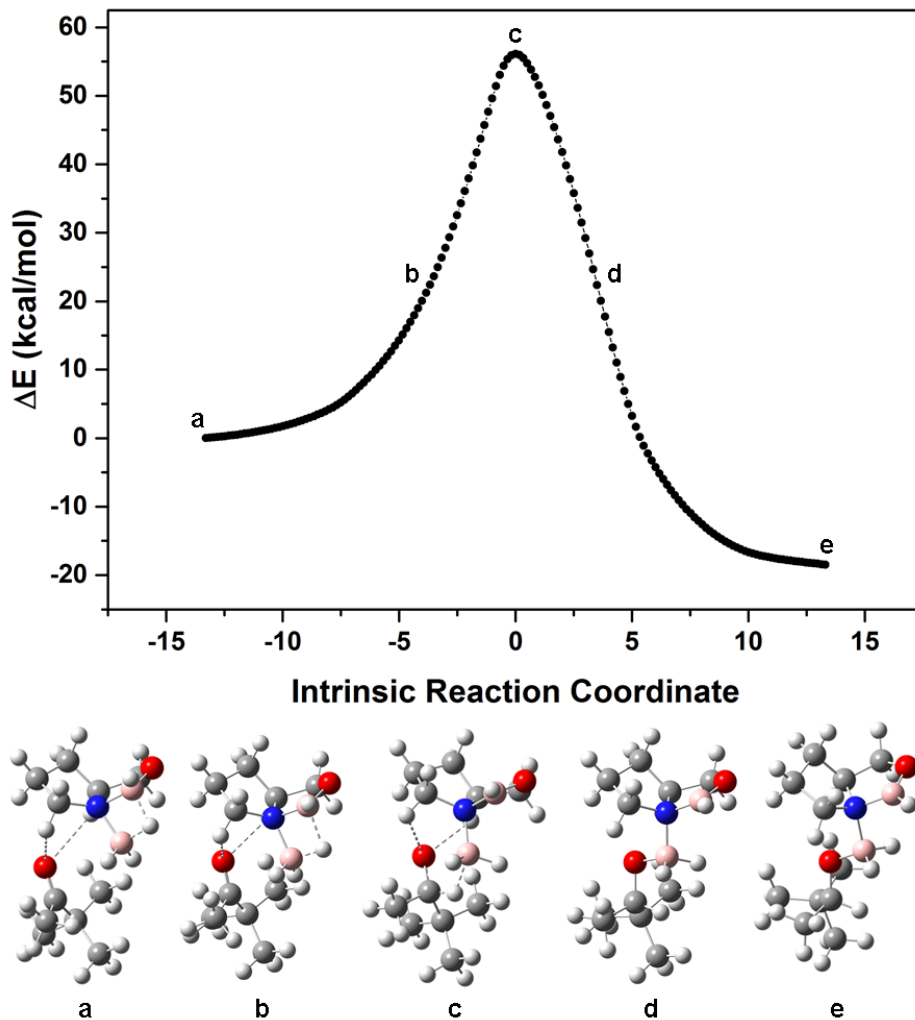
S 7: Molecular graph of **TS7** from B3LYP/6-31+G(2d,2p). Atoms are represented by large spheres: carbon (grey), hydrogen (white), oxygen (red), nitrogen (blue) and boron (pink). Bond critical points are indicated by small red spheres, ring critical points by small yellow spheres.



S 8: *t*-Butyl methyl ketone reduction reaction profile from reactants (ketone, CBS, BH₃) at relative zero to the rate limiting step: the hydride transfer transition state. Relative free energies (kcal·mol⁻¹) from B3LYP/6-31+G(2d,2p) in blue, ω B97X-D/6-31+G(2d,2p) in green and PBE0/6-31+G(2d,2p) in red.



S 9: *t*-Butyl methyl ketone reduction reaction profile from reactants (ketone, CBS, BH₃) at relative zero to the rate limiting step: the hydride transfer transition state. Relative electronic energies (kcal·mol⁻¹) from B3LYP/6-31+G(2d,2p) in blue, ω B97X-D/6-31+G(2d,2p) in green and PBE0/6-31+G(2d,2p) in red.



S 10: Intrinsic reaction coordinate for Pathway 3 **TS5**, B3LYP/6-31+G(2d,2p). The dashed lines (added using Gaussview software) indicate the carbonyl oxygen interaction with the catalyst framework as well as the bonds to the bridged hydrogen atom.